Inhibition of the influenza A virus-induced, tubulin-dependent apical mislocalization of the Na^+,K^+-ATPase in infected cells: Improving vectorial water transport and pulmonary edema clearance

Inaugural Dissertation

submitted to the Faculty of Medicine

in partial fulfillment of the requirements for the Doctor of Philosophy (PhD) Degree

by

Irina Kuznetsova

born in Leningrad, USSR

Gießen, 2019

From the Institute of Medical Virology
Director: Prof. Dr. John Ziebuhr
of the Medicine of the Justus Liebig University Giessen

First Supervisor and Committee Member: Prof. Dr. Stephan Pleschka
Second Supervisor and Committee Member: Jun. Prof. Dr. Gergely Tekes
Committee Members:

Date of Doctoral Defense: 05.05.2020

Table Of Contents

1. INTRODUCTION 7

1.1. Influenza A virus 7

1.1.1. Taxonomy and classification 7

1.1.2. Virion structure and morphology 7

1.1.3. Genome structure and protein characterization 8

1.1.4. Virus life cycle 13

1.2. Influenza A virus infection 17

1.2.1. Influenza A virus epidemiology and clinical symptoms 17

1.2.2. Influenza A virus induced lung injury 18

1.3. Na^+,K^+-ATPase 21

1.3.1. Structure of Na^+,K^+-ATPase 21

1.3.2. Functions of the Na^+,K^+-ATPase 22

1.3.3. Regulation of the Na^+,K^+-ATPase 23

2. METHODS 25

2.1. Cell cultures 25

2.1.1. Cell Culture cultivation 25

2.1.2. Polarization of Calu3 cells 26

2.1.3. Transepithelial electrical resistance (TEER) measurements 26

2.1.4. Cell viability assay 26

2.2. Viruses 28

2.2.1. Virus propagation 28

2.2.2. Foci forming assay 28

2.2.3. Preparation of lung homogenate for virus titration 29

2.3. Microsopy 29

2.3.1. Fixation of cells for immunofluorescence assay 29

2.3.2. Antibody staining and confocal laser-scanning microscopy 30

2.3.3. Preparation of polarized cells for Epon embedding and semi-thin section. 30

2.4. Analysis of protein expression 31
2.4.1. Cell lysis and detection of protein concentration 31
2.4.2. SDS-PAGE and Immunoblotting assay 32
2.4.3. On-Cell-Western blot assay 32
2.4.4. Surface Biotinylation 33
2.4.5. Subcellular fractionation by differential centrifugation 34
2.4.6. Caspase activity assay 35

2.5. *In vivo* experiments 35
2.5.1. Animal *in vivo* experiment 35
2.5.2. Wet-to-dry lung weight ratio 36
2.5.3. Preparation of lungs for histologic processing 36

2.6. Statistics 37

3. RESULTS 38

3.1. Establishment of a suitable cell line model to investigate the Na^+,K^+-ATPase mislocalization during influenza A virus infection 38

3.2. Calu3 cell line exhibits features of polarized primary alveolar cell 41

3.3. Detection of Na^+,K^+-ATPase mislocalization during influenza A virus infection of Calu3 cells 44

3.4. IAV-induced redistribution of Na^+, K^+-ATPase in Calu3 cells does not dependent on the viral replication efficiency or the virus subtype 47

3.5. IAV infection does not induce actin-dependent endocytosis of Na^+,K^+-ATPase from basolateral membrane and manipulation of the actin cytoskeleton and its regulatory molecules does not prevent Na^+, K^+-ATPase mislocalization 48

3.6. Maturation inhibition of newly produced Na^+,K^+-ATPase does not prevent its mistargeting to the apical membrane of IAV infected Calu3 cells 50

3.7. IAV infection modifies subcellular Na^+,K^+-ATPase compartmentalization 51

3.8. Microtubules are involved in mistargeting of Na^+,K^+-ATPase IAV-infected Calu3 cells 52

3.9. Inhibition of Na^+,K^+-ATPase mistargeting in Calu3 cells correlates with reduced IAV titer under ALI culture conditions 53

3.10. Inhibition of kinesin-1 prevents IAV-induced apical distribution of Na^+,K^+-ATPase 54

3.11. Rho-kinase inhibition decreases amount of acetylated α-tubulin during IAV infection 55

3.12. Influence of HDAC6 activity on IAV-induced Na^+,K^+-ATPase mistargeting 56

3.14 Effect of ROCK inhibition on IAV-induced caspase-3-dependent HDAC6-degradation 57

3.13. Influence of caspase-3 inhibition on IAV-induced apical distribution of Na^+,K^+-ATPase. 59

3.14. ROCK-inhibition improves vectorial water transport during IAV infection 60

3.15. Application of ROCK-inhibitor reduces virus titer and improves IAV-induced lung injury *in vivo* 61

4. DISCUSSION 65

5. SUMMARY 73

6. ZUSAMMENFASSUNG 74

7. REFERENCES 76

8. SUPPLIMENT 94

8.1. List of Figures 94

8.2. List of Tables 96

8.3. Materials **96**
8.3.1. Instruments 96
8.3.2. Reagents and chemicals 97
8.3.3. Inhibitors 99
8.3.4. Antibodies 100
8.3.5. Materials for cell culture and infection 102
8.3.6. Kits 104
8.3.7. Buffers and solutions 104
8.3.8. Viruses 112

8.4. List of Abbreviations **113**

8.5. Acknowledgements **116**

8.6. Affirmation **117**

1. Introduction

1.1. Influenza A virus

1.1.1. Taxonomy and classification

The influenza A virus (IAV) is a single species of the genus *Alphainfluenzavirus* that together with six other genera – *Betainfluenzavirus* (Influenza B virus, IBV), *Deltainfluenzavirus* (Influenza D virus, IDV), *Gammainfluenzavirus* (Influenza C virus, ICV), *Isavirus* (Salmon isavirus), *Quaranjavirus* (Johnston Atoll quaranjavirus, Quaranfil quaranjavirus) and *Thogotovirus* (Dhori thogotovirus, Thogoto thogotovirus) belongs to the family *Orthomixoviridae*[1]. The family includes enveloped viruses containing a segmented, negative-sense, single-stranded RNA genome that is replicated in the nucleus of infected cells. The classification of influenza viruses to IAV, IBV, ICV and IDV is based on the antigenic variations of the internal viral proteins – the nucleoprotein (NP) and the matrix protein 1 (M1)[2]. Furthermore, IAVs are subdivided into subtypes according to the serological (antigenic) properties of their two major surface glycoproteins – hemagglutinin (HA) and neuraminidase (NA). Until now 16 different antigenic subtypes of HA (H1-H16) and 9 serotypes of NA have been isolated from aquatic avian species that are considered as a main natural pool of IAVs. Additionally, two influenza A-like viruses (H17N10 and H18N11) were isolated from bats[3-5]. IAVs mainly circulate in wild birds, marine mammals, poultry and domestic mammals (swine, horses, dogs, cats)[6]. Only three IAV subtypes have been found to circulate in the human population – H1N1, H2N2 (1957 – 1968) and H3N2.

1.1.2. Virion structure and morphology

The IAV virion has a pleomorphic nature; therefore, different shapes of the virus particles can be described. Most of the clinically isolated viruses demonstrate a filamentous phenotype with an approximate diameter of 80-100 nm, and an average length of 250 nm that can sometimes have a maximum of 30 μm[7,8]. During adaptation to *in vitro* cultivation conditions, clinical isolates are losing their filamentous shape and become more spherical.[9] Spherical and elliptical virion shapes are described for the majority of laboratory-adapted IAV strains. The diameter of spherical particles is slightly bigger than the filamentous and reaches 80-120 nm. The lipid envelope of IAVs originates from the plasma membrane of the cells, in which the

virus was replicating and contains the incorporated viral transmembrane glycoproteins, HA and NA, and the ion channel protein – matrix protein 2 (M2) (Fig. 1-1). HA is evenly distributed within the virus particle, whereas NA forms clusters on the proximal end of the budding virion[9]. The HA/NA ratio in the IAV particle is usually 4-5 to 1[2]. Underneath of the membrane-derived envelope localizes the most abundant viral protein – the M1, which is arranged as a helical matrix composed by multiple copies of M1-monomers. M1 is associated with the viral envelope and/or cytoplasmic tails of HA, NA, M2 and the viral ribonucleoprotein complexes (vRNPs)[10-12]. vRNPs comprise the three subunits of the RNA-dependent-RNA-polymerase (RdRP) complex including polymerase basic 2 (PB2), polymerase basic 1 (PB1) and polymerase acidic (PA) subunits, and NP-coated viral RNA segments. IAV contains eight RNA genome segments, as well as IBV, whereas ICV and IDV genomes consist of seven gene segments. In IAV virions the vRNPs are organized in a specific "1+7" configuration and localize on the distal end of the virus particle opposite to the NA clusters. The non-structural protein 1 (NS1) and nuclear export protein (NEP)/ non-structural protein 2 (NS2) also have been detected in spherical virions of IAV[13]. The virion of IAV also includes host cell proteins in minor amount[13].

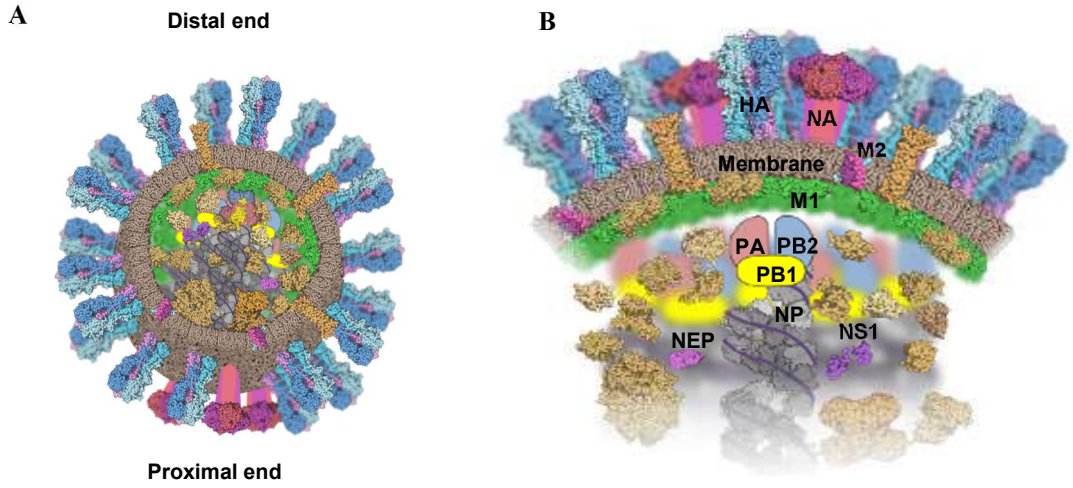

Figure 1-1 Schematic representation of an influenza virus particle, adapted from[13]**.** A cross-section of an influenza A virion indicating the NA accumulation at the proximal end **(A)** and an enlarged section **(B)**, showing the locations and relative abundance of viral proteins (colorful) and host membrane and proteins (brown) at the distal end.

1.1.3. Genome structure and protein characterization

The genome of IAV consists of eight segments of negative-sense, single-stranded RNA. Each single RNA molecule is coiled in a hairpin structure and via its phosphate groups binds

to a basic amino-acid groove of the double-helical-oligomerized NP protein with a ratio of one NP per 26 nucleotides of RNA[14-16]. NP (550 aa) is encoded by gene segment 5, containing 1565 nt. The terminal noncoding 5´- and the 3´ends of each vRNA segment contain 13 and 12 nucleotides, respectively, that are highly conserved and partially complementary. This leads to the formation of a double-stranded 'panhandle' structure[17-19]. The duplex region between the 5´- and the 3´ends associates with a heterotrimeric complex of the viral RdRP composed by PB2, PB1 and PA and functions as a viral promoter for RdRP-dependent replication and transcription[6]. The polymerase subunit proteins are the largest viral proteins (PB2 759 aa, PB1 757 aa and PA 716 aa), and are encoded by genome segments 1 (2341 nt), 2 (2341 nt) and 3 (2233 nt), respectively. PB2 recognizes and binds the 5' cap of host pre-mRNAs[20]. PA protein demonstrates cap binding, endonuclease and promoter binding activities, resulting in the cleavage of the host pre-mRNA shortly behind the cap structure. This "primer" is transferred onto the vRNA and leads to initiation of genome transcription[21-23] exerted by the PB1, which is the catalytic subunit of RdRP[24,25] (also see 1.1.4).

Apart from the RdRP subunits, segment 1, 2 and 3 of certain IAV strains encode additional proteins that are translated from the same mRNA[26-28]. Among these, the PB2-S1 protein (508 aa), which is encoded by a spliced version of the PB2 mRNA that comprises a deletion from nucleotide (nt) 1513 to 1894[29]. PB2-S1 protein interferes with polymerase activity and inhibits RIG-I-dependent signaling[29,30]. The PB1 gene can encode an alternate open reading frame (ORF) resulting in the PB1-F2 protein that is 87 to 101 amino acid (aa) long (strain dependent)[31]. PB1-F2 is a multifunction protein that is involved in regulation of polymerase activity, activation of innate immune response and induction of apoptosis[26,32-34]. PB1-N40 is the third protein encoded by the PB1 gene. It is translated from the 5th AUG initiation codon within the ORF1 of the full-size PB1 gene[28]. PB1-N40 is 718 aa long and involved in the regulation of viral transcription and replication by interaction with the polymerase complex and host factors[28,35]. Gene segment 3 as well has an alternative +1 ORF, the "X-ORF" of PA that results in a translation of a conserved PA-X protein among IAVs via ribosomal frame shift[36,37]. PA-X protein consists of 191 N-terminal aa identical to those of the PA protein and 61 C-terminal aa translated from the X-ORF[36]. PA-X possesses an endonuclease activity and plays a role in host protein synthesis shutoff leading to the inhibition of immune response, resulting in viral virulence[36,38,39]. The PA-N155 (562 aa) and the PA-N182 (535 aa) proteins are universal among most of IAVs, representing truncated forms of PA protein, transcribed from 11th and 13th initiating AUG codon within the PA mRNA, respectively[40,41]. Both proteins are involved in the control of virus replication by interaction with host proteins[42].

Segment 4 of IAV encodes only one described protein – the HA. HA (550 aa) is translated as an inactive precursor molecule HA0, folded as a trimer on the virion surface. It possess two structural regions - a membrane-proximal stalk domain, presented by triple-stranded coiled-coil α-helices and a globular receptor-binding domain, formed by antiparallel β-sheets[43-45]. HA is the main surface glycoprotein of the IAV virion. It binds to sialic-acid moieties (receptor determinant) on surface glycoproteins of the target cells (in contrast, the HA of bat IAVs can use the major histocompatibility complex (MHC) class II from different species dissimilar from sialic-acid receptor)[46,47]. Furthermore, it is responsible for the membrane fusion between the viral envelope and vesicular membranes of the cell during endosome-dependent virus entry. To perform its fusion activity HA0 requires proteolytic activation into the HA1 and the HA2 subunits, linked by disulfide bonding[48]. This cleavage generates a new amino terminus with fusion activity. Most of the HA molecules of human and zoonotic IAV possess a monobasic cleavage site. In such a case the HA0 is cleaved at a single arginine (R) or a lysine (K) residue in a Q(E)-T/X-R motif by extracellular (trypsin-like or other) proteases[48-50]. Highly pathogenic IAV (HPAI) possess polybasic cleavage site motifs (R-X-K/R-R or K-X-K/R-R), which are cleaved by ubiquitously present intracellular processing trans Golgi network (TGN) proteases, like furin or pro-protein convertases (PCs)5/6[44,49,51,52]. After the HA0 cleavage, IAV is capable of infecting a new host cell. The main receptor for IAVs is a sialic (N-acetylneuraminic) acid (SA) in the oligosaccharide chain of host N-glycans, O-glycans or glycosphingolipids[53,54]. SAs are usually bound to galactose residues within the oligosaccharide over a α-2,3 or α-2,6 bondage[10,53]. The type of SA linkage determines in great part the IAV host tropism. Thus, avian IAV strains preferentially bind to α-2,3 SA, since this type of IAV receptor is mainly distributed in avian enteric tract where these strains replicate[55,56]. Human IAVs predominantly utilize α-2,6 SA due to its high concentration in the upper respiratory tract of humans[55,57,58].

NA (454 aa) is another surface protein representing 20% of the surface glycoproteins that is encoded by segment 6 of the IAV genome[59]. NA is an integral membrane glycoprotein consisting of a cytoplasmic segment, a transmembrane domain, a stalk and a head domain, and forms a homotetrameric mushroom-shaped 60-100 Å long structure[60,61]. NA possesses an exo-sialidase activity and its active site is localized in the globular head domain[62]. Like HA, the NA recognizes α-2,3 and α-2,6 SA, but cleaves the α-2,3 linkage between SA and galactose more efficiently[56,59-61]. NA plays a major role in the process of targeting the virus to epithelial cells by promoting degradation of sialylated O-glycans of mucin molecules in mucus layer that lines the target cells[63,64]. Furthermore, NA is involved in amplification of the fusogenic activity of

the HA, promotes budding of new virions and prevents the aggregation of progeny virions with each other and to the host cells by cleavage of SA on cellular and viral glycoproteins[65,66].

Genome segment 7 encodes also more than one protein. The M1 protein (252 aa) is the primary transcript of the unspliced mRNA. The M2 protein (97 aa), the potentially encoded (undiscovered) M3 peptide (9 aa) and the occasionally expressed M4 (99 aa) proteins are the result of alternative splicing[67-69]. M1 has an essential structural role by forming a rigid matrix layer underneath the membrane-derived viral envelope[12,70-72]. M1 is also involved in the viral uncoating process, the nuclear export of newly synthesized vRNP and it inhibits vRNA synthesis at the late stage of virus genome replication[6,10,73,74]. M2, is a product of alternative splicing of the M1 mRNA and consist of three domains – an N-terminal ectodomain domain, a transmembrane segment and a C-terminal domain. Four identical M2 monomers form a single-pass, pH-regulated, proton-selective ion channel, which is activated by low exterior pH in the range pH 4.5-5.0[67,69,75,76]. M2 function is necessary during virus entry, leading to a proton influx lowering the virion-internal pH needed for the M1 dissociation from the vRNP complexes, allowing these to enter into the cytoplasm[75-77]. Functional activity of M2 is also required during virus replication, since the M2 is integrated into cellular membranes resulting in an proton efflux and increasing of the lumenal pH in the TGN to prevent conformational changes of (intra-cellular-cleaved) pH-sensitive HA proteins[76,78]. M2 also facilitates virus budding and scission[11,79-81]. Until now the function of the M3 mRNA transcript during the IAV life cycle is not described, but it was shown that M3 mRNA is not required for efficient virus replication in cell culture[82]. The M4 mRNA is translated into the M42 protein and it can be a functional alternative for M2 in M2-deficient virus[83,84]

The shortest IAV genome segment 8 encodes the non-structural protein 1 (NS1, 230 aa), the nuclear export protein (NEP, 121 aa) and the non-structural protein 3 (NS3, 187 aa). NS1 is transcribed from the full length mRNA and has two functional domains - an N-terminal RNA-binding domain and a C-terminal effector domain[85-87]. NS1 is one of the early-expressed virus proteins during IAV-infection; it exists as a homodimer and has multiple functions, including antagonizing the host innate immune response and regulating the viral replication[85,87-90]. NEP is expressed from the spliced NS mRNA and is involved in the export of vRNP from the host cell nucleus, in the regulation of virus replication and the budding processes[89,91-93]. The last described protein encoded by alternative splicing of NS1 mRNA is the NS3 protein. NS3 is similar to the NS1 protein, but contains an internal deletion and is associated with the adaptation of avian IAV to a mammalian host, such as mouse, human, swine or dogs[94].

Table 1. IAV RNA segments and encoded proteins

RNA segment number	vRNA (nt)	Gene product	Number of amino acids	Main functions
1	2341	PB2	759	RdRP subunit, recognition and binding to cellular mRNA cap
		PB2-S1	508	Inhibition of RIG-I dependent interferon (IFN) signaling
2	2341	PB1	757	Catalytic subunit of RdRP (elongation) with endonuclease activity
		PB1-F2	87-101	Apoptosis induction activity, regulation of host IFN response
		PB1-N40	718	Regulation of PB1/PB1-F2 expression ratio
3	2233	PA	716	RdRP subunit with endonuclease activity, Cleaves capped RNA fragments off of the host's pre-RNA
		PA-X	61	*In vitro* – involved in regulation of veirus replication and inhibition of host innate immune response
		PA-N115	561	Possible role in virus replication, but function is not determined
		PA-N182	534	Function is not determined
4	1778	HA	566	Attachment to the receptor, membrane fusion
5	1565	NP	498	Binds to ssRNA, protection function within vRNP complex, nuclear import/export of vRNA
6	1413	NA	454	Degradation of mucus layer, receptor disruption, involved in virion release
7	1027	M1	252	Contribution in virion morphology and structure, nuclear import/export of vRNA , budding
		M2	97	Contribution in uncoating process and stability of HA conformation during protein-syntesis
		M3	9	Function is not determined
		M42	99	Function is not fully established, can serve as M2 complements
8	890	NS1	230	Suppressing of host mRNAs production, post-transcription regulation, innate immune response antagonist
		NEP	121	Regulation transcription/regulation timing, vRNP nuclear export
		NS3	187	May be important for adaptation to a new host

1.1.4. Virus life cycle

The first step in the IAV replication cycle is represented by virus binding to the host cell receptor determinant mediated by the HA (Fig. 1-2). The HA receptor binding domain is localized on the distal end of the globular head of the HA1 subdomain and is highly conserved among IAV subtypes[92, 93]. HA binds with low affinity to the SA on the host cell glycoproteins or glycolipids, but due to the attachment by other HAs to several SAs, the binding efficiency is increased[95]. Upon attachment, the IAV particle enters the cell by receptor-mediated endocytosis via clathrin-coated or uncoated vesicles or macropinocytosis[96-99]. After uptake, IAV undergoes endosomal trafficking from the early endosome (EE) to the late endosome (LE), involving the activity of many host factors, including small GTPases, Rab5, Rab7, focal adhesion kinase, actin filaments and microtubules (MT)[100-105]. In the late endosome at low pH, HA undergoes an irreversible conformational change that leads to the exposure of 'fusion peptide' of the HA2 subunit and later to its insertion into the endosomal membrane resulting in the fusion of the endosomal and the viral membrane[106-109]. M2 mediated proton influx into the virion in the late endosome acidifies the inside of the virus particle to induce a conformational change in the M1, resulting in its dissociation from the NP associated with the vRNPs[110-113]. In the next step, vRNPs are released into the cytoplasm to be imported into the nucleus where the genome replication and transcription takes place. Nuclear vRNP import is dependent on the host karyopherin (importin) α1, α5, β import system and nuclear localization signals (NLS) in the NP, whereas NLSs of PB2, PB1 and PA are used later in the life cycle for the single protein nuclear import[91,114-118].

Viral transcription of a negative-sense vRNA starts by a primer-dependent mechanism (Fig. 1-3). For this, IAV retrieves host cell pre-mRNA cap structures by a process also known as 'cap-snatching'[119]. The PB2 subunit of the RdRP recognizes the 5'-m^{7}GpppXm cap structure of a nascent host transcript and the endonuclease activity of the PA subunit cleaves the host pre-mRNA 10-13 nucleotides downstream of the PB2-bound 5'-end[20,120,121]. Next, this capped primer engages the catalytic center of the PB1 subunit by rotation of the PB2 cap-binding domain and viral mRNA elongation takes place based on vRNA template-defined addition of nucleotides[122]. Generation of the viral mRNA is finalized by auto-polyadenylation through RdRP stuttering at a specific oligo-U stretch 17-22 nt upstream from 5'-end of the vRNA[123-126]. Synthesis of PB2, PB1, PA, NP and NS1 mRNAs takes place at the early stage of virus replication, whereas HA, NA and M1 mRNAs are more dominant at the late stage.

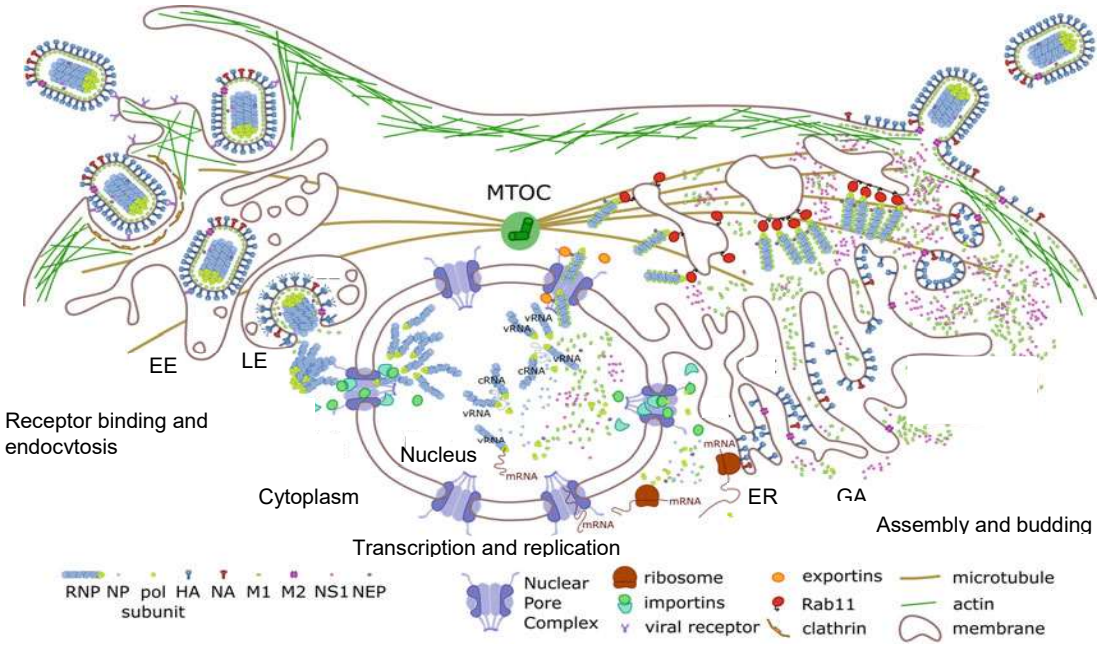

Figure 1-2 Schematic representation of the IAV life cycle, modified from[127]. The virion attaches to the apical plasma membrane receptors and enters the cells via receptor-mediated endocytosis. After fusion and uncoating in late endosomes, vRNPs are released into the cytosol and are then transported into the nucleus via importins. vRNA replication and transcription takes place in the nucleus. Nuclear export of mRNA and newly synthesized vRNAs is mediated by exportins. Viral proteins are translated in the cytoplasm by cytosolic and ER-associated ribosomes. PB2, PB1, PA, NP, M1, NS1 and NEP are reimported into the nucleus where assembly of new vRNPs takes place. By recruitment of the exportin Crm1 via NEP and M1, vRNP are exported from nucleus followed by Rab11-associated microtubule-dependent transport to the apical membrane where budding process takes place. HA, NA and M2 proteins take the ER-GA- associated transport pathway. (EE: early endosome, LE: late endosome, ER: endoplasmic reticulum, GA: Golgi apparatus, MTOC: microtubule-organizing center).

Before nuclear export, mRNAs encoded by M and NS segment undergo splicing by recruiting the cellular spliceosome[67,87,128]. For viral protein production, IAV then utilizes the translation machinery of the host cell. Membrane-associated proteins (HA, NA and M2) are translated by endoplasmic reticulum (ER)-associated ribosomes, translation of other viral proteins is situated at cytosolic ribosomes. In order to generate new vRNPs, subunits of the RdRP and NP protein are imported back into the nucleus by utilizing host α-importin for the PB2 import, importin-5 and karyopherin-β for import of the PB1:PA heterodimer and importin α1, α3 and α5 for NP import[14]. M1, NS1 and NEP as well are transported back to the nucleus[129]. In the nucleus, NP, PB2, PB1 and PA are associating with newly synthesized cRNA (see below) and are involved in the generation of new vRNA molecules. Replication of vRNA is carried out by the RdRP and includes two processes - first, an unprimed generation of a positive-sense complementary RNA (cRNA), followed by the second step – synthesis of a new negative-sense

vRNA based on the cRNAs template. In comparison with mRNA, cRNA is a full-length copy of the vRNA, and is not polyadenylated and does not have a cap-structure[130-133].

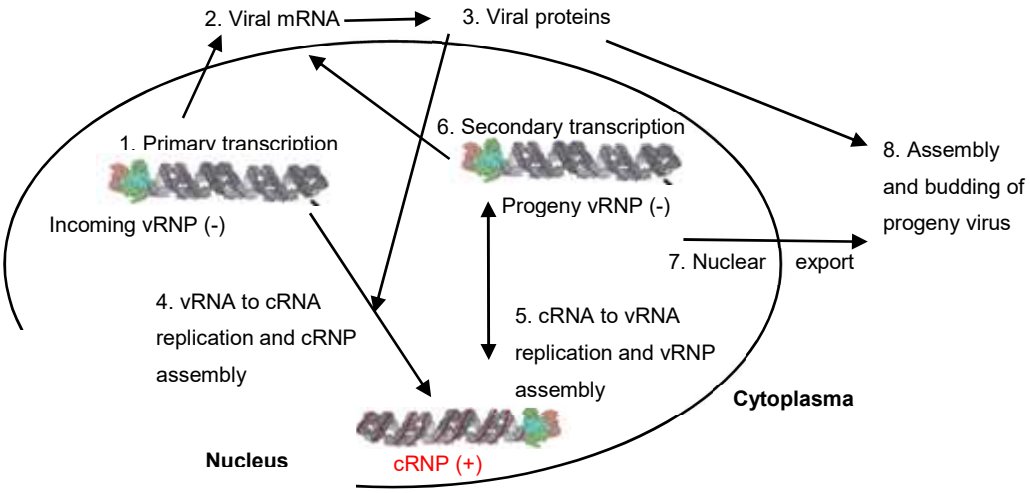

Figure 1-3 Influenza A virus RNA replication/transcription, adapted from[134]**.** Simplified scheme of transcription and replication of vRNAs during the life cycle of influenza A virus. (vRNA: viral (negative-sense) RNA, cRNA: (positive-sense viral) complementary RNA).

Newly generated vRNAs associate with NP and RdRP subunits to form the vRNP complex. vRNPs of different genome segments are aggregating in multi-structures (2-3-4 vRNPs) and are then actively transported from the nucleus through nuclear pores at the early stage of virus replication via the cellular β-exportin / chromosome region maintenance 1 (CRM1)-dependent pathway with the help of NEP and M1 proteins[74,92,135-141]. M1 protein associates with NP within vRNP and with NEP, which contains two nuclear export signals (NES) recognizable by the exportin CRM1 and its cofactor Ran-GTP[91,142,143]. At the late stage of virus replication vRNPs are exported passively from the nucleus due to the caspase3/7-dependent enlargement of nuclear pores[144]. The cellular Y box binding protein 1 (YB-1) also binds to vRNPs in the nucleus and is exported together with M1-NEP-vRNPs complex into the cytoplasm, where it facilitates vRNP association with microtubules around the microtubule-organizing center (MTOC)[145]. From the MTOC to the cell surface vRNPs are transported via the endocytic recycling compartment by the Rab11-dependent pathway[146-149]. Ras-related protein Rab11 is a marker of recycling endosomes (RE). It belongs to the family of small GTPase and mediates several processes of intracellular vesicle trafficking, including delivery of plasma membrane proteins to the apical or perinuclear endosomes, exocytic processes of the TGN and motility of RE towards the cell surface[150,151]. Rab11 can form complexes with different molecular motors, which enables the vesicular transport along microtubules in direction of their (-) and (+) end,

as well as actin-dependent transport[151]. In respect to molecular motors, Rab11 can associate with KIF5A, KIF3, KIF13 of the kinesin-1, kinesin-2 and kinesin-3 families providing (+) end microtubule (MT)-directed transport. The association with dynein light chains 1 and 2 enables (-) end MT-directed transport and an association with the myosin motor protein - myosin Vb, provides actin-dependent transport[152-158]. The transport efficiency is facilitated by the Rab11-family interacting proteins (FIPs), that are used either as an adaptor molecules between Rab11 and different molecular motors or as an effector of motor protein affinity to the Rab11-positive vesicle membranes[151,159]. KIF13 is the only until now described molecular motor that is facilitating Rab11-dependent vRNP transport and presence of FIPs was described to be dispensable for IAV infection[148,160,161]. Transport of vRNA to the cell surface was described as dependent on both - the actin- and the MT cytoskeleton, since a pharmacological disruption of actin or MT networks led to impaired shuttling of vRNP to the cell surface and reduced virus titer [100,146,161-164]. Post-translational acetylation of microtubules also influences vRNP transport to the apical cell membrane, since activation of histone deacetylase 6 (HDAC6) that possesses a tubulin deacetylase activity, decreases vRNP trafficking and virus titer[165]. GTP-bound (activated) Rab11 associates with vRNPs by interaction with PB2[146,162]. Binding of vRNPs to Rab11 induces its redistribution and impairs recycling endosome sorting efficiency by an undescribed mechanism[149]. Clusters of Rab11-vRNP vesicles form hotspots containing eight distinct vRNPs under the plasma membrane in the region of virus budding. Approximately 500 nm from the cell surface vRNPs are then dissociating from Rab11[166]. The mechanism of vRNPs transport into the budding zone stays unclear. During the vRNP transport to the cell surface, M1 and NEP are also co-transported together by Rab11-vesicles.

HA, NA and M2 are synthesized at the rough ER (rER) and transported to the cell surface via the secretory pathway[167]. HA and NA contain apical sorting signals and their transport from the rER to the Golgi apparatus (GA) where they obtain required post-translational sugar modifications, is associated with the coat protein I (COPI) complex[168]. An apical localization signal in the M2 protein is not yet identified, but COPI is also involved in M2 transport from the rER to the GA[168]. Already in the TGN, NA and HA are associated with lipid raft microdomains that contribute to the apical shuttling of the glycoproteins and organization of the viral budding zone[169,170]. Acetylated microtubules are also involved in the trafficking of the HA to the plasma membrane[165]. M2 protein is excluded from lipid rafts, but is targeted to the apical membrane in an actin-dependent manner, where it associates with HA clusters[171,172]. Transport of M2 to the apical plasma membrane requires the host factors ubuiquitin protein ligase E3 component N-recognin 4 (UBR4), transport protein particle complex 6A

(TRAPPC6AΔ) and Rab11, since the knockdown of these proteins reduces M2 surface expression, but does not have a negative effect of HA and NA distribution[75]. Accumulation of HA and NA in lipid drafts in plasma membrane induces formation of the budding zones[11,173] and triggers nuclear vRNP export via Raf/MEK/ERK signaling[174]. M2 associates with lipid rafts at the edges of the budding zones, due to the cholesterol recognition/interaction amino acid consensus (CRAC) motif, allowing cholesterol binding and membrane integration. Palmitoylation of the Cys50 residue allows lipid raft association[175-177]. Each vRNP contains identified packaging signal sequences, but the mechanism of the formation a "1+7" pattern in a budding zone and its uptake into the virus particle remains elusive[178]. M1 protein oligomerizes below the plasma membrane providing the structure of the progeny virion and is believed to interact with HA, NA, M2, NEP and vRNPs[179-181]. When the virion is completely formed, M2 protein becomes localized at the neck of the growing bud where it generates a negative Gaussian curvature resulting in membrane constriction and pinching off of the virus particle[34]. Finally, NA cleaves off sialic acids from cellular and virus glycoproteins promoting virion release[129]

1.2. Influenza A virus infection

1.2.1. Influenza A virus epidemiology and clinical symptoms

Influenza viruses cause an acute infectious respiratory disease in humans. Outbreaks occur in form of seasonal influenza epidemics, caused by IAV and IBV, and sporadic pandemics caused by IAV. Antigenic drift and antigenic shift are two distinct mechanisms of virus surface glycoproteins modification that lead to formation of epidemiological influenza virus variants. Antigenic drift is a gradual accumulation of mutations in the HA and NA, induced by the error prone genome replication as the RdRP does not possess a proof-reading function and by antibody-mediated selective pressure in the hosts[182,183]. It occurs in both IAV and IBV and results in seasonal epidemics[182,183]. Antigenic shift is described only for IAV and refers to the exchange of vRNPs upon co-infection with different IAVs (reassortment). This can result in an introduction of IAVs with novel characteristics and possibly HAs with new antigenic properties into the human population[183,184]. Such viruses can rapidly spread, as there is no pre-existing human immunity that could counteract, and can therefore lead to worldwide pandemics. Five pandemic outbreaks have been documented in the last 100 years – the Spanish influenza in 1918/1919 (H1N1), the Asian influenza in 1957 (H2N2), the Hong Kong influenza in 1968 (H3N2), the re-emergence of H1N1 in 1977 (Russian influenza) and swine origin influenza in 2009 (H1N1, Mexico influenza). Spread of new IAVs variants in an immunologically naïve

human population causes increased morbidity and mortality due to severe acute pulmonary hemorrhage and edema[183,185]. HA of seasonal IAVs preferentially binds to α-2,6 SAs, which are mainly distributed on the surface of epithelial cells in the upper respiratory tract of humans[186]. Seasonal viruses can spread easy and fast via aerosol and droplets of nasal discharges, but the infection is normally limited to the upper respiratory tract (URT) – nasal cavity, pharynx and larynx[187,188]. Seasonal viruses often cause disease characterized by fever, headache, myalgia, malaise accompanied by non-productive cough, nasal discharge, and sore throat[183,189].

Human infections with pandemic viruses was often associated with a severe infection of lower respiratory tract (LRT), including infection of bronchioles and type II pneumocytes expressing α-2,3 SA receptors preferable used by avian IAV[186,187]. Sequence analysis of HA genes in the IAVs of 1918/1919 H1N1, 1957 (H2N2), 1968 (H3N2), and 2009 (H1N1) revealed changes in the HA receptor binding site, allowing α-2,6, α-2,3, or α-2,3/α-2,6 sialic acid specificity[190-196]. Due to the fact, that the primary target of α-2,3 SA-dependent IAVs is located in LRT, the spread of these viruses in the human population is limited, but LRT infections are more sever and associated with acute pneumonia, necrotizing bronchitis, intestinal inflammation and alveolar lumen flooding with edema fluid, leading to development of acute respiratory distress syndrome (ARDS)[187,197-199].

1.2.2. Influenza A virus induced lung injury

IAV directly induces lung injury by infecting lung epithelial cells, disrupting the tight junctions among them and by activation of the intrinsic apoptosis/necrosis pathway in infected cells[187,200-202]. Additionally, IAV infection of alveolar epithelial cells leads to the insufficiently controlled production of pro-inflammatory cytokines and chemokines, including IP-10, IFNβ, IL-1β, IL-6, RANTES, CCR2, TNFα. This results in recruitment of inflammatory cells followed by abundant immune cell infiltration and tissue damage, that cannot be resolved in severe cases[187,197,200-203]. Disruption of the epithelial-endothelial barrier leads to protein-rich fluid leakage into the alveolar lumen resulting in respiratory insufficiency. Under the normal conditions, clearance of the lung edema strongly depends on the limited protein transport across the epithelium out of the alveolar lumen, and on the presence of an osmotic gradient allowing water transport via aquaporins and intracellular pathways in alveolar epithelial cells towards the interstitial lumen [202]. Alveolar epithelium is composed by squamous, flat type I pneumocytes (alveolar epithelial cells (AEC) type I, AT I), that comprise 90% of the alveolar

surface and which are actively involved in gas exchange and ions and water transport[204]. The second type of alveolar epithelial cells – cuboidal type II pneumocytes (alveolar epithelial cells type II, AT II) also play an important role in fluid homeostasis and ions transport, and are involved in pathogens recognition and activation of the immune response[205]. ATs II possess a progenitor cell function during lung repair and IAVs are almost exclusively replicating in AT II[197,206].

Barrier function of the alveolar epithelium is based on the tight interconnection of the cells and their high polarization (Fig. 1-4). Within the epithelium, cells are attached to each other via the adherent junctions, which are intracellular linked to the actin cytoskeleton and formed by the transmembrane protein E-cadherin and intracellular components of the catenin protein family[207]. Tight junctions (TJ) are composed by the transmembrane proteins occludin, claudin and by scaffolding proteins zona-occludens (ZO-1,-2,-3), localized in cytoplasm[207]. TJs regulate paracellular transport of ions and solutes, providing a low epithelial permeability and cellular polarity, described as an intrinsic asymmetry in distribution of structures within the cell. Asymmetric expression of membrane ion-channels and pumps results in the establishment of an osmotic gradient. Amiloride-sensitive epithelial sodium channel (ENaC) is expressed on the apical cell membrane of AT I and AT II and is responsible for sodium ions uptake (Na^+), that is accompanied by the chloride ion (Cl^-) transport via the cystic fibrosis transmembrane conductance regulator (CFTR)[202,204]. Sodium-potassium adenosine triphosphatase (Na^+,K^+-ATPase, NKA) is located on the basolateral cell membrane and actively transports three Na^+ ions to the interstitial space against the concentration gradient creating an osmotic force for passive water transport from alveolar airspace to the lung lymphatic and microvascular vessels[202,204,208]. Both AT I and AT II express aquaporins – membrane water channels, involved in water transfer across the membrane[209].

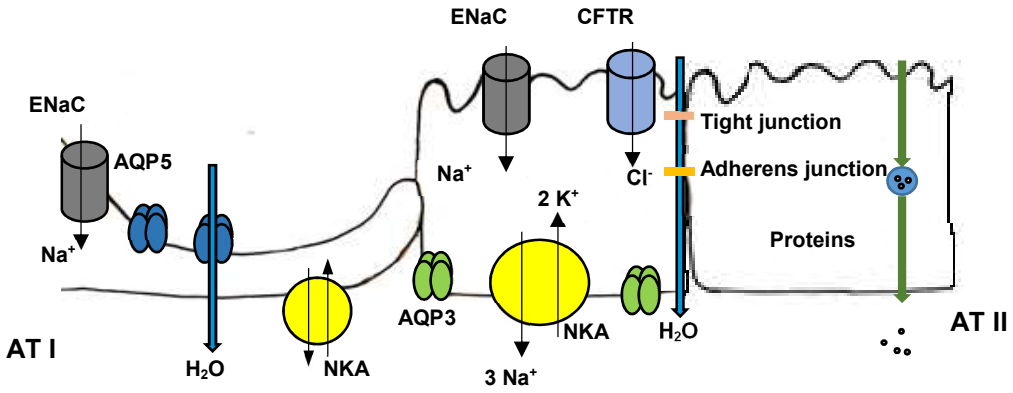

Figure 1-4 Schematic representation of alveolar epithelium. Alveolar epithelia consist of alveolar epithelial cells type I (AT I) and alveolar epithelial cells type II (AT II), connected with each other via adherent

and tight junctions. Epithelial cells possess an asymmetric expression of ion channels and pumps. (ENaC: epithelial sodium channel, CFTR: cystic fibrosis transmembrane conductance regulator, AQP: aquaporin, NKA: sodium-potassium adenosine triphosphatase, H_2O: water)

IAV infection affects the alveolar epithelium integrity by inducing the loss of the TJ protein claudin-4, resulting in increased epithelial permeability (Fig. 1-5)[201]. IAVs also negatively regulate expression and function of ENaC and CFTR and thus further impair alveolar fluid clearance[210-213]. Additionally, IAV-induced paracrine cross-talk between infected epithelial cells and macrophages leads to the reduction of the NKA basolateral amount in non-infected alveolar epithelial cells negatively affecting edema resolution[214].

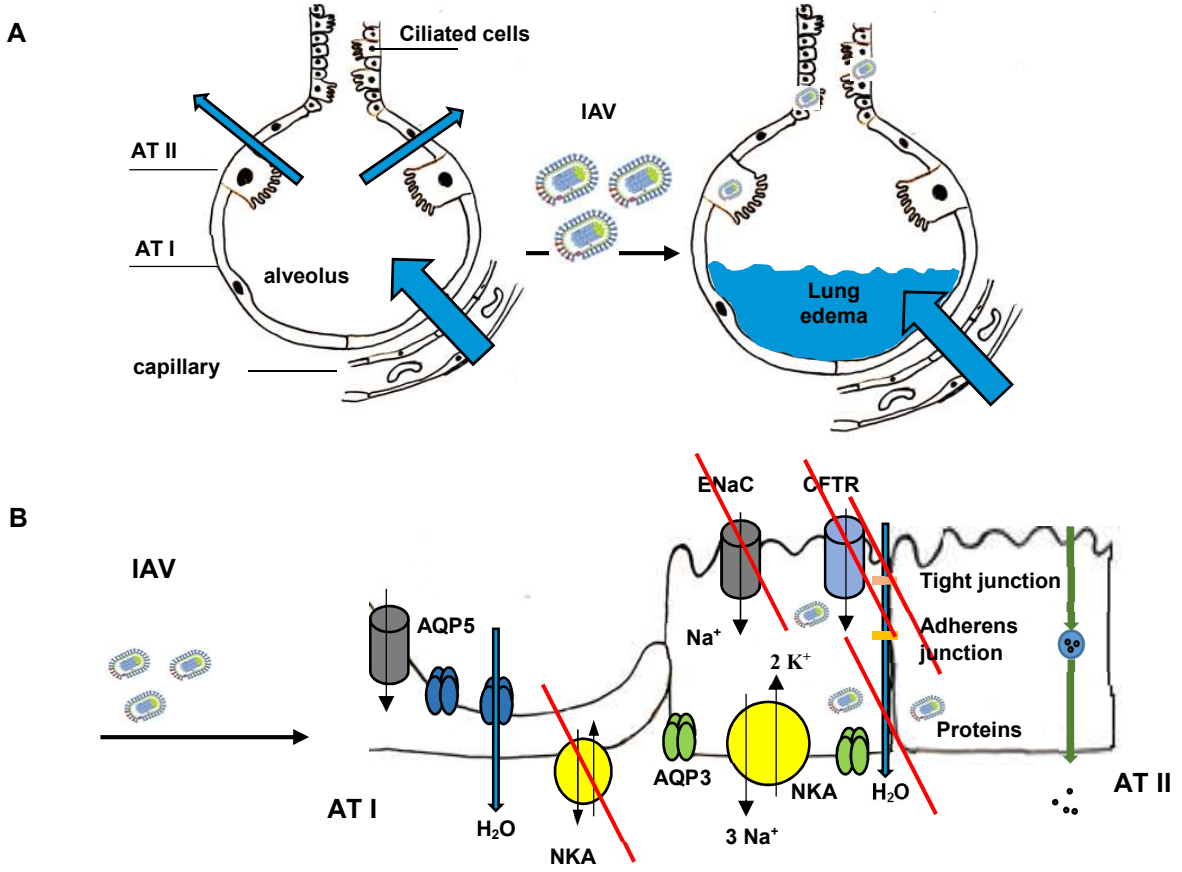

Figure 1-5 Pathological effect of IAV on lung edema resolution. (A). Schematic representation of alveolar edema formation induced by influenza virus. **(B).** IAV-induced decrease of ion channel and transporter plasma membrane expression resulting in disruption of vectoral water transport. Alveolar epithelia consist of AT I and AT II, connected with each other via adherent and tight junctions. AECs possess asymmetric expression of ion channel and pumps.

1.3. Na^+,K^+-ATPase

1.3.1. Structure of Na^+,K^+-ATPase

The NKA is a heterodimeric integral membrane protein that belongs to the largest and most diverse family of the ATP-dependent ion transporters, the P-type ATPases. NKA consists of the catalytic α-subunit, the β-subunit and a FXYD protein (Fig.1-6).

The catalytic α-subunit has a molecular weight of 100-110 kDa, composed by ten transmembrane helices, five extracellular loops, three cytosolic domains, the N-(nucleotide binding)-, the P-(phosphorylation) and the A-(actuator) domain. The N- and C-terminus have an intracellular localization[215]. Four distinct isoforms of the α-subunit have been identified and they have only minor differences in aa sequence, despite of being encoded by different genes[216]. The α-subunit displays binding domains for Na^+,K^+, ATP, phosphate and for the cardioactive glycoside ouabain – the inhibitor of the NKA.

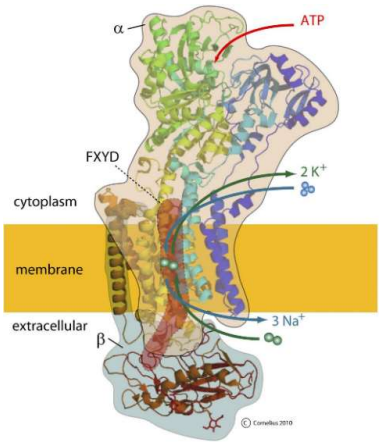

Figure 1-6 The molecular structure of Na^+,K^+-ATPase, modified from[217]**.** The catalytic α subunit (pink) is composed of ten transmembrane helices and five exposed extracellular loops. The β subunit (light blue) contains a short intracellular N-terminal domain (30 amino acid residues), a single transmembrane domain and an extracellular domain, which is interacting with the extracellular loop of the α subunit between the M7 and M8 transmembrane helices. The FXYD protein is a tissue specific protein associated with M9 α-helix and may interact with the β subunit.

The β-subunit is a type II glycoprotein (app. 55 kDa) with a short intracellular domain, a single transmembrane span and a large extracellular, highly glycosylated C-terminus domain. Three different isoforms of the β-subunit have been described[218]. The β-subunit is involved in maturation of the NKA by acting as a molecular chaperone, has an influence on the functional activity of NKA by changing Na/K affinity of the α-subunit and has an important role in establishment of cell polarity[217-221].

The tissue-specific FXYD protein consists of a single transmembrane helix and an N-terminal extracellular domain with a PFXYD motif. It associates with the extracellular and the transmembrane domains of the β subunit[218]. Seven isoforms of the FXYD protein are described in mammals and they regulate substrate affinities of NKA as well as a maximal ion conductance[222].

Functional expression of NKA in the plasma membrane requires assembly of α- and β-subunits in the ER and only the α/β-assembled complex may exit the ER to the Golgi complex, where enzyme maturation takes place[223-225]. In absence of the β-subunit, the α-subunit associates with β-COP protein, a component of the coat protein II (COPII) complex, that leads to ER-retention followed by degradation[226]. Basolateral localization of NKA in most of the epithelia is strongly dependent on the adhesive properties of the β1-subunit[224,227,228.] Association of α1-and β2-subunits leads to apical NKA mislocalization under the pathological condition of autosomal dominant polycystic kidney disease (ADPKD) or under normal conditions in the retinal pigment epithelium (RPE)[229,230]. The stoichiometry of α- and β-subunits in the active membrane integrated enzyme is 1:1, but α- and β-subunits are as well independently involved in different cellular functions[225,231,232].

1.3.2. Functions of the Na^+,K^+-ATPase

The NKA is an omnipresent ion pump that is actively involved in the establishment and the maintenance of the Na^+ and K^+ gradient across plasma membrane. Most of mammalian cells have a low intracellular concentration of Na^+ (5-15 mM), and a high concentration of K^+ (140 mM), whereas extracellular concentrations of these ions is reversed (Na^+ -145 -150 mM and K^+ - 5 mM)[233]. NKA transfers 3 Na^+ out of the cell and 2 K^+ into the cell against the concentration gradient using energy by ATP hydrolysis. More than 40% of total produced energy in mammals is spend for NKA activity[234]. By the regulation of ion concentration, the NKA maintains a stable osmolarity of the cells preventing swelling and it creates a driving force for the secondary transport of glucose, amino acids or phosphates and generates an electrical transmembrane potential[218,221]. The osmotic Na^+ gradient by NKA is crucial for the reabsorption processes of the kidney and the gut tissue, as well as in the vectorial paracellular water transport in the alveolar airspace to enable normal gas exchange[216,235,236.]. Thus, ARDS and acute lung injury (ALI) are associated with impaired edema clearance due to the decreased function of epithelial NKA[236]. Functional activity of the enzyme is also required for the formation of tight junctions and desmosomes leading to development of polarized epithelial cells[237-239]. NKA is further

involved in regulation of actin dynamics and stress fibers formation[235,238-240]. Although, NKA does not have kinase or phosphatase activities, it plays an important role as a signal transducer in cell signaling[241]. NKA directly interacts with regulatory proteins, such as membrane-associated non-receptor tyrosine kinase Scr, B-cell lymphoma 2 (BCL-2), phosphoinositide 3-kinase (PI3K), protein phosphatase 2 and EGFR. Therefore, NKA is involved in cell proliferation, differentiation, apoptosis and homeostasis via participation in control of Raf/MEK/ERK, PI3K/Akt, PLC/PKC, Ca^{2+}-signaling and generation of reactive oxygen species (ROS)[241-244].

1.3.3. Regulation of the Na^+,K^+-ATPase

Regulation of NKA abundance and function occurs at the transcriptional, post-transcriptional, translational and post-translational level. As it was mentioned above, expression of the NKA subunits is tissue specific and the level of subunit expression changes during development, cellular activity and ion homeostasis[245]. A long-term regulation of NKA expression in a response to extracellular stimuli includes several DNA-binding transcription factors, including histone deacetylase 2 (HDAC2), Snail, specificity protein (Sp) and hormone receptors, that activate or repress the enzyme production[245-248]. A short-term regulation that leads to a quick response to extracellular stimuli, involves changes of the enzyme kinetic, of its ion affinity and of NKA trafficking between the plasma membrane and the intracellular pool, which contains 30-70% of all cellular NKA[249]. During ALI induced by mechanical lung ventilation, hypoxia, hypercapnia, alcohol, endotoxin or oleic acid, the abundance of the membrane located NKA is reduced due to endocytosis of the enzyme[249,250]. This process is reversible upon the abrogation of the extracellular stimulation, while a sustained stimulation leads to the lysosomal degradation of NKA, as a part of the phosphorylation-ubiquitination-recognition-endocytosis-degradation (PURED) regulatory mechanism[249]. Phosphorylation of the residue Ser18 in the α1-subunit of NKA by the AMP-activated protein kinase (AMPK)-activated protein kinase C (PKC-ζ) is a pre-requisite for its clathrin-dependent endocytosis. Subsequent NKA dephosphorylation takes place in late endosomes[251,252]. Phosphorylation of Ser18 is also necessary for NKA ubiquitination at the positions Lys16, 17, 19 and 20 of the α1-subunit N-terminus[253]. NKA translocation from the plasma membrane is further regulated by the Rho-associated coiled-coil containing serin/threonine kinase (ROCK), as well as by protein kinase A (PKA) that are both controlling rapid reorganization of the actin cytoskeleton,

allowing NKA endocytosis[254-256]. Phosphorylated and ubiquitinated NKA undergoes lysosomal degradation, leading to the reduction of its intracellular and plasma membrane abundance.

IAV-infection of primary human and murine alveolar epithelial cells decreases the NKA amount on the basolateral membrane of neighboring, non-infected cells[214]. IAV-infection also induces host type I IFN production of infected alveolar macrophages that leads to release of TNF-related apoptosis–inducing ligand (TRAIL) expression and subsequent activation of PKC-ζ signaling in non-infected cells, resulting in NKA degradation and impaired lung edema resolution[214]. Interestingly, in IAV-infected cells, the amount of the plasma membrane-associated NKA was unchanged[214], but it was found to be mistargeted to the apical cell membrane (Peteranderl et al., under submission).

In contrast, other extracellular stimuli, such as β-Adrenergic agonists, dopamine or insulin can improve alveolar fluid reabsorption by increasing the plasma abundance of NKA via its recruitment from the intracellular pool to the plasma membrane[257-260]. Dopamine or insulin treatment of alveolar cells leads to the dephosphorylation of the α1-subunit residue Ser18 by protein phosphatase 2A (PP2A) and to microtubule-dependent transport of NKA containing vesicles to the plasma membrane, facilitated by microtubule-associated molecular motor kinesin I[257,261-263]. Activation of atypical protein kinases C (aPKCs: aPKC-ϵ and aPKC-δ, protein kinase B (PKB) also known as Akt) and activity of the Ras-related protein Rab10, a regulator of the apical and the basolateral recycling pathways, is also required for NKA recruitment to the plasma membrane[259,261].

2. Methods

2.1. Cell cultures

2.1.1. Cell Culture cultivation

All cell lines were cultivated in 75 cm^2 or 165 cm^2 tissue culture flask at 37 °C in a 95% humidified atmosphere of 5% CO_2. When cell monolayers reached 90% confluence cells (except Calu3 cells which do not reach 100% confluence, maximum 50%) were washed once with PBS -/- and detached with Trypsin-EDTA. Cells were resuspended in a suitable media (see table below) and seeded in 6-well, 12-well, 24-well tissue plates, in 15 cm tissue dishes or on sterile glass-cover slips placed within a culture well 24 hours prior of each experiment.

Cell culture	Origin	Source	Media composition
A549	human lung adenocarcinoma epithelial cells	American Type Culture Collection, Manassas, VA, USA	DMEM, 10% heat inactivated (hi, 56 ºC for 1 h) FCS, 25mM Glucose, 4mM L-Glutamine
BEAS 2B	human bronchial epithelial cells	Cell culture collection, Institute of Medical Virology, Justus-Liebig University Giessen, Germany	BEGM, 10% hi FCS, BEGM BulletKit
CaCo2	human colon adenocarcinoma epithelial cells	Cell culture collection, Institute of Medical Virology, Justus-Liebig University Giessen, Germany	DMEM-F12, 10% hi FCS, 2mM GlutaMax
Calu3	human adenocarcinoma bronchial epithelial cells	American Type Culture Collection, Manassas, VA, USA	MEM, 15% hi FCS, 4mM GlutaMax, 1mM Sodium Pyruvate, 1% Non-Essential Amino Acids Solution
MLE 15	Murine lung epithelial cells	Cell culture collection, Institute of Medical Virology, Justus-Liebig University Giessen, Germany	DMEM, 10% hi FCS, 25mM Glucose, 4mM L-Glutamine
MDCK II	canine kidney epithelial cells, subclone II.	Cell culture collection, Institute of Medical Virology, Justus-Liebig University Giessen, Germany	DMEM, 10% hi FCS, 25mM Glucose, 4mM L-Glutamine

2.1.2. Polarization of Calu3 cells

In order to obtain highly polarized Calu3 cells, the cell monolayer in a 175 cm^2 tissue culture flask grown to 50 % confluence was washed once with PBS -/- and treated with Trypsin-EDTA. Cells were resuspended in 10 ml culture medium and centrifuged for 15 min at 300 x *g*, 24 °C. Supernatant was discarded and cells were resuspended in 5 ml of culture medium. 30 µl of cell suspension were mixed with 30 µl of 0.4% trypan blue dye and cell concentration was calculated in Neubauer chamber according manufacturer's instruction. Cells were dilute to a concentration of 2×10^6 viable cells/ml in Calu3 culture medium and 250 µl/125 µl of the cell suspension containing 0.5×10^6 / 0.25×10^6 viable cells were placed to the apical compartment of each Transwells® insert in a 12/24 well plate. 1/0.3 ml of Calu-3 culture medium was added into the basolateral compartments, avoiding the introduction of air bubbles and cells were cultivated at 37 °C, 5% CO_2. For the cells grown under the Liquid-Liquid Interface (LLI) condition, medium was replaced in both compartments each second day. For Air-Liquid Interface (ALI), culture medium was aspirated from the apical compartment on the day two, whereas medium was replaced every 2 days in the basolateral compartments.

2.1.3. Transepithelial electrical resistance (TEER) measurements

In order to measure trans-epithelial electrical resistance Millicell®ERS-2 epithelial Volt-Ohm meter was used. First, cells were allowed to come to the room temperature (RT). For ALI culture – 300 µl of culture medium was added to the apical compartment prior measurement. The electrode of the Volt-Ohm meter was washed once with 70% ethanol, then with sterile ddH_2O and once with culture medium at RT. Then, the electrode was placed in Transwells® so that the shorter tip did not contact the cell layer on the membrane in the upper compartment and the longer tip touched just a bottom of the outer well. TEER was calculated as a difference between the resistances obtained for the Transwells® with cells and blank -Transwells® without cells per one square centimeter. The unit of TEER is Ωcm^2.

2.1.4. Cell viability assay

In order to check a cytotoxicity of applied inhibitors a commercial available reagent - PrestoBlue™ has been used. The reagent – resazurin (7-hydroxy-10-oxidophenoxazin-10-ium-

3-one)-based compound is converted into the reduced form by the mitochondrial enzymes of viable cells with a change of color and can be quantified using either spectrophotometric or fluorometric approach. The viability assay was performed according to the manufacturer's protocol. Calu3 cells were seeded on a 96-well plate in a concentration 1×10^4/well in 90 µl of culture medium 24 h later were treated with media containing the inhibitors at different concentrations and 24 h later 10 µl of 10-fold ready-to-use PrestoBlue™ reagent were added to each well. The plate was then incubated 30 min at 37°C in darkness and subsequently the absorbance was measured at 570 nm wavelength by Tecan Spark® 10M multimode microplate reader to determine the amount of resazurin conversion.

2.1.5. Vectorial water transport

Vectorial water transport (VWT) as a characteristic of the physiological status of the Calu3 cell monolayer was measured by changes of FITC-dextran concentrations in apical and basal cell culture medium of polarized Calu3 cells grown on Transwells® inserts for 14 days under Liquid-Liquid Interface conditions. For this, the cells were either mock infected or infected with *PR8* at a multiplicity of infection (MOI): 2 for 1 hour at 37 °C. Inoculum was removed and cells were supplied with the Infection medium #2 containing 1 mg/ml of 70 kDa FITC-dextran and 5 µM Rho-kinase inhibitor RKI-1447 (XIII) in DMSO or just the equal amount of DMSO (solvent). Cells were incubated at 37 °C for 8 and 24 h. 30 µl of cell culture medium from apical and basal side were collected, diluted 1:1 with PBS -/- and placed on 96 well flat bottom black plates. The fluorescence intensity of the samples was measured at excitation wavelength 480 nm and emission wavelength 535 nm by Tecan Spark® 10M multimode microplate reader. VWT was calculated using the formula:

$$C0 = [1 – (C0/Ca)] – [1-(C0/Cb)]$$

, where

C0- fluorescence value of culture medium at starting point;

Ca - fluorescence value of culture medium in apical side of Transwells® inserts;

Cb - fluorescence value of culture medium in basal side of Transwells® inserts

2.2. Viruses

2.2.1. Virus propagation

All viruses were propagated in MDCK II cells in 165 cm^2 culture flask. For this a 24-hr-old 85% confluent monolayer of cells was washed once with PBS -/- and 5 ml of PBS +/+/BA/PS containing virus dilution corresponding to MOI equal to 0.01 were added, followed by 45 min of incubation at a room temperature. Subsequently, inoculum was removed, cells were washed with PBS -/- and were incubated in Infection medium #1 containing 1 mg TPCK-treated trypsin ml^{-1} at 37 °C for 2 days. Supernatant was collected and virus titer was determined by a foci-forming assay.

2.2.2. Foci forming assay

For the foci forming assay, MDCK II cells were seeded in 96-well plates at a concentration of 3×10^6 cells/plate. The next day, 10-fold dilutions in duplicates (from 10^{-1} to 10^{-8}) in PBS +/+/BA/PS was prepared from each virus sample in U-shaped 96-well. Importantly, during the preparation of the dilutions the pipet tips were changed after each dilution step. The MDCK II cells in the 96-well plate(s) were washed once with PBS+/+. Then 50 µl of the according dilutions for each sample in the U-shaped plate were transferred onto the MDCK II cells in an according well of the 96-well plate, which were then incubated for 45 min. After incubation, inoculum was removed starting with the 10^{-8} dilution row without changing the pipet tips and 100 µl of Avicel medium containing 1 mg TPCK-treated trypsin ml^{-1} were added to each well. Cells were incubated at 37 °C, 5% CO_2 for 30 hours followed by the immunocytochemical analysis to detect virus-infected cells. For this, cells were washed twice with 200 µl of PBS +/+, were fixed and permeabilized in 4% (w/v) paraformaldehyde (PFA) containing 1% (v/v) Triton-X-100 for 30 minutes at room temperature. Next, cells were trice washed with 400 µl of washing buffer (PBS +/+ with 0.05% (v/v) Tween® 20) and overlaid with 50 µl of primary anti-NP antibody solution (3% (w/v) BSA in PBS +/+) for 2 hours at room temperature. Then, cells were washed tree times with washing buffer followed by incubation with 50 µl of secondary Horse-Radish Peroxidase (HRP) labeled anti-mouse antibody. 1 hour later, cells again were washed with 400 µl of washing buffer and 40 µl AEC-staining buffer were added to each well. Following incubation for 30 min at 37 °C until foci could be detected, the staining buffer was removed and cells were washed twice with dH_2O. Air-dried plates were scanned by using the

Epson Perfection V500 Photo scan (Epson) at 1200 dpi and total number of foci was determined per well. Since Avicel-medium has a high viscosity that prevents diffusion of virus particles in surrounding media, virus can spread only from one cell to other forming foci. The viral titer per 1 ml was determined by formula:

$$Number\ of\ foci\ per\ well \times \frac{1000\ \mu l}{50\ \mu l} \times dilution\ factor^{-1} = ffu/ml$$

, where *ffu* is foci forming unit.

2.2.3. Preparation of lung homogenate for virus titration

For analysis of the virus titer in infected lung epithelial cells by foci assay, mice were sacrificed by exsanguinations. The pulmonary circulation was flushed with sterile PBS -/-via the right ventricle. Flushed blanched lungs were removed and washed with cold PBS -/-. Lobes were sheared with scissors and remaining tissue was dissociated by pipeting in 1 ml PBS -/- to single cell suspensions. Cells were pelleted by centrifugation at 400 x *g* for 10 min at 4 °C and supernatant was subjected to foci assay as described earlier.

2.3. Microsopy

2.3.1. Fixation of cells for immunofluorescence assay

For immunofluorescence assay cells were washed ones with PBS +/+ and fixed with or without extra permeabilization at the indicated time points. Depending on the primary antibodies used cells were either fixed and permeabilzed with organic solvents or fixed with the cross-linking reagent paraformaldehyde. As organic solvents either pre-cooled (-20 °C) 1:1 (v/v) aceton:methanol solution (for NKA α1 staining) or pre-cooled (-20 °C) 100% methanol (for tubulin staining) was used for 3 min at -20 °C followed by three times washing with washing buffer and blocked with blocking buffer for one hour at RT or overnight at 4 °C. As a cross-linking reagent 4% (w/v) PFA solution was used to fix the cells for 10 min at RT, followed by washing thrice with PBS +/+ containing 30 mM glycine (G-PBS) and subsequently permeabilized with 0.25% (v/w) Triton X-100 for 7 min. Then cells were washed three times with G-PBS and were overlaid with blocking solution (3% (w/v) BSA in G-PBS, G-PBS/BSA) for 30 min at RT. Fixed cells were then treated with 0.25% (v/w) Triton X-100 in G-PBS for 15 minutes, washed with G-PBS three times followed by blocking in G-PBS/BSA for 30 min.

2.3.2. Antibody staining and confocal laser-scanning microscopy

For antibody staining cells were then incubated with specific primary antibody (dilution given in 2.1.4) in antibody diluting solution. The antibody dilution was added to the fixed cells (+/- permebilization) for 2 h at RT, followed by washing twice with PBS +/+. The cells were then incubated for 1 h with secondary antibody conjugated to Alexa Fluor 488, Alexa Fluor 568, Alexa Fluor 594 or Alexa Fluor 647 diluted in antibody diluting solution. Then cells were washed thrice with PBS -/-, once with ddH_2O and cover slips or polyester membrane from Transwells® were mounted on a glass slide with ProLong™ Gold antifade mountant with DAPI (conc. not given by the manufacture) overnight. Signals were visualized by using a Leica TCS-SP5 confocal laser-scanning microscope with HCX PL Apo 63x/1.30 GLYC objective and a pinhole – 1 airy unit (AU). Z-Stack was acquired using 0.25 µm step size and results were analyzed by Imaris software (Bitplane).

2.3.3. Preparation of polarized cells for Epon embedding and semi-thin section.

Calu3 cells cultured on Transwells® inserts were fixed with 1.5% (v/v) glutaraldehyde in 0.1 M cacodylate buffer (pH 7.4) for 5 h at RT and were washed in 0.5 M phosphate buffer (pH 7.4) overnight at 4°C. Then the cells were treated with 1% (v/v) osmium tetroxide in 0.1 M cacodylate buffer for 1 h at RT, three times washed with 0.1 M cacodylate buffer for 5 min at RT followed by two times washing with ddH_2O. The cells were then dehydrated on ice in a graded ethanol series:

Ethanol concentration	Time	°C
30%	15 min	RT
50%	15 min	RT
70%	15 min	RT
80%	10 min	RT
90%	10 min	RT
96%	10 min	RT
100%	10 min	RT
100% with molecular sieve 0.3 nm	overnight	4°C

The cells on the Transwells® membranes were then treated with Epon in following procedure:

100% ethanol: Epon ratio	Time	°C
2:1	3 h	RT
1:1	overnight	+ 4
1:2	4 h	RT
Pure Epon	2 h	RT

The cells were then embedded in Epon in plastic flat embedding molds and dried at 60 °C for 24 h. Semi-thin cross-sections (300 nm) of the cells were cut on Reichter Ultracut R ultratome and stained during 2 min by 0.5 % Toluidine blue in ddH_2O.

2.4. Analysis of protein expression

2.4.1. Cell lysis and detection of protein concentration

To analyze quantitative changes in protein expression levels under different conditions, cells were washed ones with ice-colds PBS +/+ and then treated with cold NP40-lysis buffer (50 µl per one well of 12 well plate, 100 µl per one well of 6 well plate) containing proteases/phosphatases inhibitors for 2 min. Next, cells in NP40-lysis buffer were detached from plastic with a cell scraper and incubated in a reaction tube (Eppendorf) on ice for 20 min with pulse-vortex each 5 min. Cell debris was precipitated by centrifugation at 16,200 x *g* for 15 min at 4 °C. Quantification of protein concentration in the supernatants was performed by colorimetric Bradford assay according to the manufacturer's instruction. The Bradford assay is based on an absorbance shift after complex formation between the Brilliant Blue G-250 dye and proteins in solution. Briefly, 2 µl of cell lysate were diluted 1:10 in PBS -/-. Next, 5 µl of this dilution was mixed with 250 µl of the Bradford reagent in 96-well plates with flat bottom and incubated for 15 min at RT. The absorbance of the samples was measured at wavelength of 595 nm using Tecan Spark® 10M multimode microplate reader. As a standard dilutions of BSA (0-0.3 mg/ml) in PBS -/- were used. Each sample and the standard were measured in triplicates. Protein concentrations were determined by comparison to the standard curve and recalculated according to the used dilution. 20 µg of protein per sample were used for SDS-PAGE.

2.4.2. SDS-PAGE and Immunoblotting assay

The gel percentage required was dependent on the molecular weight of protein of interest.

Protein molecular weight	Gel percentage
10 – 45 kDa	15%
10–70 kDa	12.5%
15-100 kDa	10%
25-250 kDa	8%

A sample volume containing 20 µg of protein was mixed with SLAB-loading buffer, incubated for 5 min at 95 °C and cooled on ice for 1 min, then shortly centrifuged at 16,000x*g* for 10 sec. To detect the Na^+,K^+-ATPase, samples containing 30 µg of protein after mixing with SLAB-loading buffer were incubated for 30 min at 37 °C with shacking at 650 rpm in order to prevent agglutination of the highly hydrophobic Na^+,K^+-ATPase α1 subunit. Then, samples were shortly centrifuged at 16,000 x *g* for 10 sec, were loaded into the pockets of the SDS-gel and electrophoresis was performed under denaturing reducing condition for 2 h at 35 mA and 100V. Next, washed for 30 sec in 100% methanol 0.45 µm PVDF-membrane was laid on the layer of two blotting papers soaked with Anode buffer on Semi Dry Blotter Unit. SDS-PAGE gel was placed on the membrane and covered with two blotting papers soaked in Cathode buffer. Proteins were transferred onto a PVDF membrane for 1.5 h at 0.8 mA/cm^2 under semi-dry conditions. Subsequently, unspecific epitopes were blocked by incubation of the membranes in TBS containing 0.05% (v/v) Tween®20 (TBS-T) and 5% (w/v) nonfat dry milk for 1 h. The membranes were then washed once for 5 min in TBS-T buffer at RT and then were incubated with primary antibody (see 6.2.4) in TBS-T containing 2% (w/v) nonfat dry milk overnight at 4 °C. After washing thrice for 5 min with TBS-T, membranes were incubated for 1 h at RT with the corresponding fluorescent-dye- or HRP-conjugated secondary antibodies (see 2.1.4). Then membrane were washed thrice for 5 min with TBS-T. The immunoblots with fluorescent-dye conjugated secondary antibodies were scanned on the Odyssey Classic Infrared Imaging System. The membranes blotted with HRP-conjugated secondary antibodies were incubate with SuperSignal West Femto Substrate for 5 min and the signal was visualized and quantified with ChemoCam Imager.

2.4.3. On-Cell-Western blot assay

For the On-Cell Western blot assay, Calu3 cells were seeded in 96-well with optically clear flat bottom plates at a concentration of 6×10^4 cells/well. 24 hours later when the cell monolayer was 95% confluent, cells were infected with specified strain of influenza A virus at an MOI of

2. After 45 min of incubation at 37 °C the inoculum was replaced by the Infection medium #2 containing inhibitor at indicated concentration (see 6.2.5.1) or solvent of the inhibitor as a control. 24 hours later medium containing either inhibitor or solvent was removed and primary antibody that recognize an extracellular epitope of HA, M2 or the Na^+,K^+-ATPase β1 subunit diluted in PBS +/+ (see 6.2.4) were added and plates were further incubated for 1.5 h at 37 °C at 5% CO_2. Cells were then washed three times with PBS+/+, fixed with 4% PFA for 20 min at RT followed by washing thrice with PBS +/+ for 5 min each. Then, cells were treated with blocking buffer containing 3% BSA (w/v) for 45 min at RT and then incubated in dark with the secondary IRDye 800-conjugated anti-mouse, rabbit or goat antibody (accordingly to the host of primary antibody) diluted in blocking buffer containing 5 µM DRAQ5™ (a far-red DNA stain) for 1 h at RT. Cells were then washed three times with TBS-T and scanned on the LI-Cor Odyssay Infrared Imager (100 µm resolution, 0.5 mm focus offset). Data were analyzed using Image Studio, Excel and GraphPad Prism 5 software.

2.4.4. Surface Biotinylation

To analyze plasma membrane localized proteins, cells were incubated with membrane-impermeant EZ-link Sulfo-NHS-SS-Biotin, which binds to primary amino groups (-NH_2) on surface proteins, forming covalent bonds. In order to prevent endocytosis and degradation of the labeled proteins all steps were performed with pre-cooled reagents on ice. Cells were washed thrice with ice-cold PBS +/+ and then incubated with Biotinylation buffer containing 1 mg/ml of biotin for 20 min at 4°C with regular shaking. Next, cells were washed three times with10 mM glycine in PBS +/+ for 10 min each time, followed by one washing step with ice-cold PBS +/+. After complete aspiration of remaining PBS +/+ cells were lysed with NP-40 lysis buffer. Cell lysates were incubated on ice for 30 min with pulse-vortexing each 5 min and then centrifuged at 95,600 x *g* for 10 min at 4°C in order to pellet cellular debris. The supernatant was collected and the protein concentration of the samples was measured by Bradford assay as described in above. 300 µg of protein in 300 µl of lysis buffer were mixed with 60 µl streptavidin-coupled beads and incubated on a rotating mixer at a rotation speed of 40 rpm at 4°C overnight, allowing biotinylated proteins to bind. 16 hours later, beads were washed once with washing solution A, twice with washing solution B and three times with washing solution C, each time using a volume of 300 µl of ice-cold solutions after centrifuging the sample at 95,600 x *g* for 3 min at 4 °C. In order to release bound proteins, beads were resuspended in 35 µl of SLAB-loading buffer, containing 100 µM 1,4-dithiothreitol-reducing

agent that breaks the disulfide bridges in the spacer arm of EZ-linked Sulfo-NHS-SS-Biotin allowing protein elution from the beads, and heated up to 37 °C for 30 min. Beads were then precipitated by centrifugation and the supernatant was loaded onto an 10% SDS-PAGE.

2.4.5. Subcellular fractionation by differential centrifugation

A discontinuous sucrose gradient was prepared 24 h prior the experiment. For this, 70% (w/w) sucrose solution in ddH2O was prepared and it has been used for preparation of the next sucrose fractions in following procedure:

% of sucrose	70% sucrose stock, ml	ddH2O, ml
30	4.29	5.71
35	5	5
40	5.71	4.29
45	6.43	3.57
50	7.14	2.86
60	8.57	1.43
65	9.29	0.71
70	10	0

0.5 ml of each sucrose fraction was loaded in ultra-clean 14 x 89 mm tubes starting with the 70% fraction from the tube's bottom and tubes were incubated overnight at 4 °C. Calu3 cells grown in 152 cm^2 tissue culture dishes were infected mock or with *PR8* at an MOI: 2 and incubated for 24 h at 37 °C. Cells were scraped from the dish bottom, resuspendent in 2 ml of hypotonic buffer and incubated for 30 min on ice followed by homogenization by using a pre-chilled Dounce homogenizer. Nuclei and unbroken cells were precipitated by centrifugation at 800 x *g* for 10 min at 4 °C. The PNS was added to the top of a discontinuous (30% to 70%) sucrose gradient. The tubes were placed in SW41 Ti Swinging-Bucket rotor for Beckmann LE-80 Ultracentrifuge and centrifuged at 130000 x *g* for 4 h at 4 °C with the break switched off. Twelve fractions (each 500 µl) were collected from the top to the bottom and analyzed by immunoblotting using antibodies against membrane proteins (E-Cadherine, α1 NKA, luminal endoplasmic reticulum (ER) protein - ERp72, Golgi protein – RCAS1, early endosomal marker – EEA1 and Rab5, late endosomal marker – Rab7, recycling endosomal marker – Rab11) and against the viral NP.

2.4.6. Caspase activity assay

To determine the proteolytic caspase activity in lysates of Calu3 cells, a commercially available colorimetric protease assay kit was used. The caspase activity assay is based on the proteolytic cleavage of the colorimetric substrate, which is composed of the chromophore, p-nitroanilide (*p*NA), and a synthetic tetrapeptide substrate: DEVD (Asp-Glu-Val-Asp-(cut)-*p*NA) for caspase 3, LEHD (Leu-Gly-His-Asp-(cut)-*p*NA) for caspase 9 or IETD (Ile-Glu-Thr-Asp-(cut)-*p*NA) for caspase 8, which is upstream of caspase cleavage site. A spectrophotometer or a microplate reader at 400/405 nm can detect light absorbance of free pNA. Calu3 cells grown on 6-well plates were infected with *PR8* at an MOI of 2 and overlaid with the Infection medium #2 containing either 5 µM Rho-kinase inhibitor XIII, DMSO or 1µM staurosporine (strong inducer of caspase activity) as positive control. 0, 6, 16 and 24 h post infection/treatment cells were washed ones with ice-cold PBS +/+, scraped, vortexed and centrifuged at 200x*g* for 5 min at 4 °C. The cell pellet was resuspended in 50 µl of chilled cell lyses buffer (provided in the kit) and incubated 10 min on ice followed centrifugation at 10000 x *g* for 1 min. Protein concentration of samples was determined by Bradford assay. 200 µg of protein per sample were incubated with 5 µl of 5 mM *p*NA substrate at 37 °C for 2 h in darkness. The absorbance of the samples was measured at a wavelength of 400 nm using Tecan Spark® 10M multimode microplate reader. *p*NA light absorbance in the sample of mock infected, untreated cells was used as baseline activity.

2.5. *In vivo* experiments

2.5.1. Animal *in vivo* experiment

All animal experiments were performed by Balachandar Selvakumar, PhD, according to the latest guidelines of the ‘‘Federation of European Laboratory Animal Science Associations (FELASA)” and approved by the local committee of the Max-Planck Laboratory for Heart & Lung Research Instituto de Investigación en Biomedicina de Buenos Aires (IBioBA). Six-week-old BALB/c mice (n=5 per group) were infected by intra-tracheal inoculation of 500 plaque-forming units (pfu) /mouse of *PR8* in a volume of 30 µl. Fasudil HCl was diluted in sterile PBS -/- and was daily applied intraperitoneally (IP) at a concentration of 10 mg/kg 24 h p.i. during the next 7 days. As a control IP injection of sterile PBS -/- were applied. Body weight

was monitored every day until day 8 p.i.. On the day 7 after treatment start (= day 8 p.i.) mice were sacrificed by an overdose of isoflurane.

2.5.2. Wet-to-dry lung weight ratio

The lung wet-to-dry (W/D) weight ratio was used to analyze lung water accumulation after IAV infection. The animals were sacrificed, dissected, and the lung 'wet' weight was measured immediately after its excision. The lungs were then dried in an oven at 60 °C for 5 days and re-weighed as dry weight. The W/D weight ratio was calculated by dividing the wet by the dry weight.

2.5.3. Preparation of lungs for histologic processing

The animals were sacrificed, lungs were perfused via the right ventricle with PBS -/-, removed from chest cavity, fixed in 4% PFA for 24 h and were then embedded in Paraffin (Leica ASP200S). Paraffin embedded lungs were cut into thin sections (3.5 µm) using a Microtome RM2125 (Leica). Slices were mounted on to charged slides and dried overnight at 37 °C. Next day, lung sections were stained by Hematoxilin/Eosin by following procedure:

Step	Time
Xylene	5 min
Xylene	5 min
100% ethanol	30 s
100% ethanol	30 s
100% ethanol	30 s
96% ethanol	30 s
96% ethanol	30 s
70% ethanol	30 s
70% ethanol	30 s
Hematoxylin	3-5 min
0,1 % HCL	2 s
Flowing tap water	5 min
0,5% Eosin G solution	3 min
Tap water	30s
70% ethanol	30 s
96% ethanol	30 s

100% ethanol	30 s
100% ethanol	30 s
100% ethanol	30 s
Xylene	5 min
Xylene	5 min

Microscopic analysis was performed by EVOS FL Auto Cell Imaging System. A total amount of cells in histological cuts was quantified by Aperio CS2 Scanner (Leica Biosystems Imaging Inc., CA, USA) using „Aperio v9 nuclear count algorithm“ software (Leica Biosystems Imaging Inc., CA, USA) in collaboration group of Univ.-Prof. Dr. Achim Gruber (Freie Universität Berlin).

2.6. Statistics

Statistical analysis was performed by GraphPad Prism 5 software. The data are given as a mean + either standard error of mean (SEM) or standard deviation of the mean (SD) (indicated in figure legend). The statistical significance of two groups was tested by a two-tailed unpaired Student’s t test. The statistical significance of three or more groups was analyzed by one-way ANOVA followed by Tukey's post hoc test. A p value was considered as a significant, if it was less than 0.05, *$p<0.05$; **$p<0.01$; ***$p<0.005$

3. Results

3.1. Establishment of a suitable cell line model to investigate the Na^+,K^+-ATPase mislocalization during influenza A virus infection

Recently, the important observation was made that in IAV-infected murine primary alveolar epithelial cells the Na^+,K^+-ATPase (NKA) is not only found at the "normal" basolateral site, but is also mistargeted to the apical membrane (Peteranderl et al., under submission). As this might well have a great impact on IAV-induced edema formation, this work presented here aimed to investigate the underlying molecular mechanisms and cellular/viral factors involved.

In a first step a suitable cell system, representing all, important characteristics of lung alveolar epithelia cells had to be established. Due to the limited lifespan, a finite expansion capacity and a high sensitivity to growth conditions of primary cells, which strongly impairs an intensive investigation of the observed phenomenon using such cells, human (A549, BEAS, Calu3, CaCo2, and H441), canine (MDCK II) and murine (MLE15) permanent cell cultures were tested to identify a cell line model capable to reproduce the results that have been observed with primary cells.

First, the selected cells were analyzed for they ability to support influenza virus A/Puerto Rico/8/34 (H1N1, PR8) replication. All cell lines except H441 (data not shown) supported virus replication and demonstrated the maximum of virus titer 48 h p.i.. The highest virus titer (7.8 log10 FFU/ml) was observed by infection of MLE-15 cells, whereas human bronchial epithelium cells (BEAS) demonstrated the lowest virus titer (3.5 log10 FFU/ml). (Fig. 4-1).

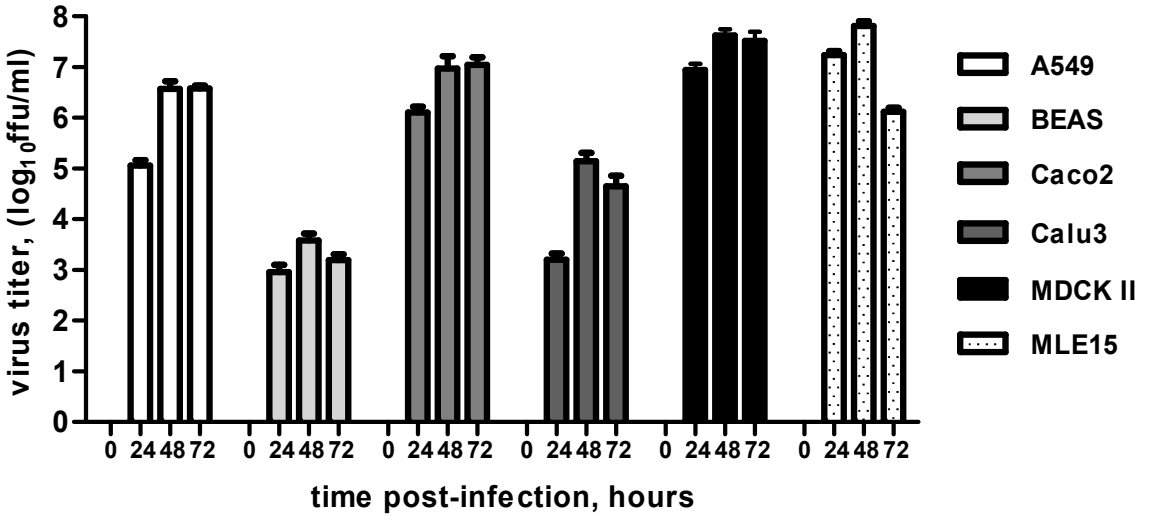

Figure 4-1 Growth kinetic of PR8 on different permanent cell lines. A 24-hours-old monolayers of A549, BEAS, CaCo2,Calu3, MDCK II and MLE-15 cells were infected with IAV *PR8* (MOI: 0.01). Virus titer was determined by foci assay in MDCK II cells at the indicated time points post infection (p.i.). Data represents means + standard deviation (SD), n = 6.

Next, the permissive cell lines were screened for their NKA α1-subunit expression level after IAV infection. As it was previously shown on primary murine and human alveolar epithelial cells, that IAV infection leads to the reduction of the total NKAα1 amount in non-infected cells[214] the selected cells were infected with *PR8* at an multiplicity of infection (MOI) =: 0.1. Only Calu3 and MDCK II cells demonstrated a significant reduction of the total NKAα1 amount in the course of viral infection (Fig. 4-2, A, B, C). The maximal decrease of total NKAα1 expression of 3.2- and 2.1-fold at 24 h p.i. and 16 h p.i. was observed in Calu3 and in MDCK II cells, respectively.

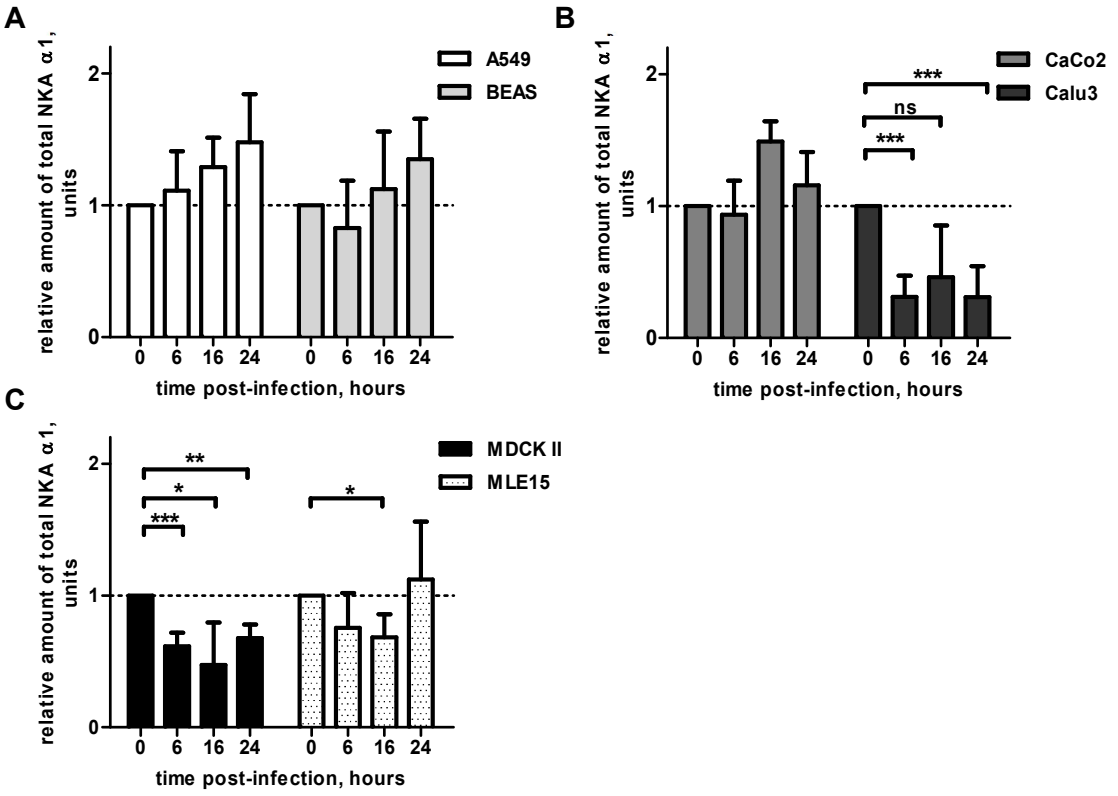

Figure 4-2 Total Na^+,K^+-ATPase α1-subunit expression in different IAV-infected cell lines. A549 and BEAS **(A)**, CaCo2 and Calu3 **(B)**, MDCK II and MLE15 **(C)** cells were infected with *PR8* (MOI: 0.1) and 0, 6, 16 and 24 h p.i. whole-cell extracts were separated by SDS-PAGE and analyzed by immunoblotting using a monoclonal anti-NKAα1 antibody. The values represent relative density of the bands normalized to β-actin + standard error of mean (SEM), n=4.

To determine whether IAV infection induces apical mislocalization of NKA in the selected cell lines, Calu3 and MDCK II cells were subjected to immunofluorescence analysis followed by confocal microscopy. At the early stage of the viral life cycle, a change in the localization

pattern of NKA could not be observed and the majority of the protein was localized in the basolateral membrane (BLM) of infected cells (Fig. 4-3, A, B). Viral NP protein was detectable in the nuclei of the cells already 6 h p.i., where replication and transcription of viral genome takes place indicating formation of progeny viral ribonucleoprotein complexes (vRNPs) (Fig. 4-3, A, B). At later times (24 h p.i.), the NP protein was mainly distributed in the apical cell compartment where the budding process of IAV takes place. Interestingly, apical NP localization correlated with apical NKA appearance in infected cells. Mislocalization of NKAα1 was detected in Calu3 cells and in MDCK II cells (Fig. 4-3, A, B).

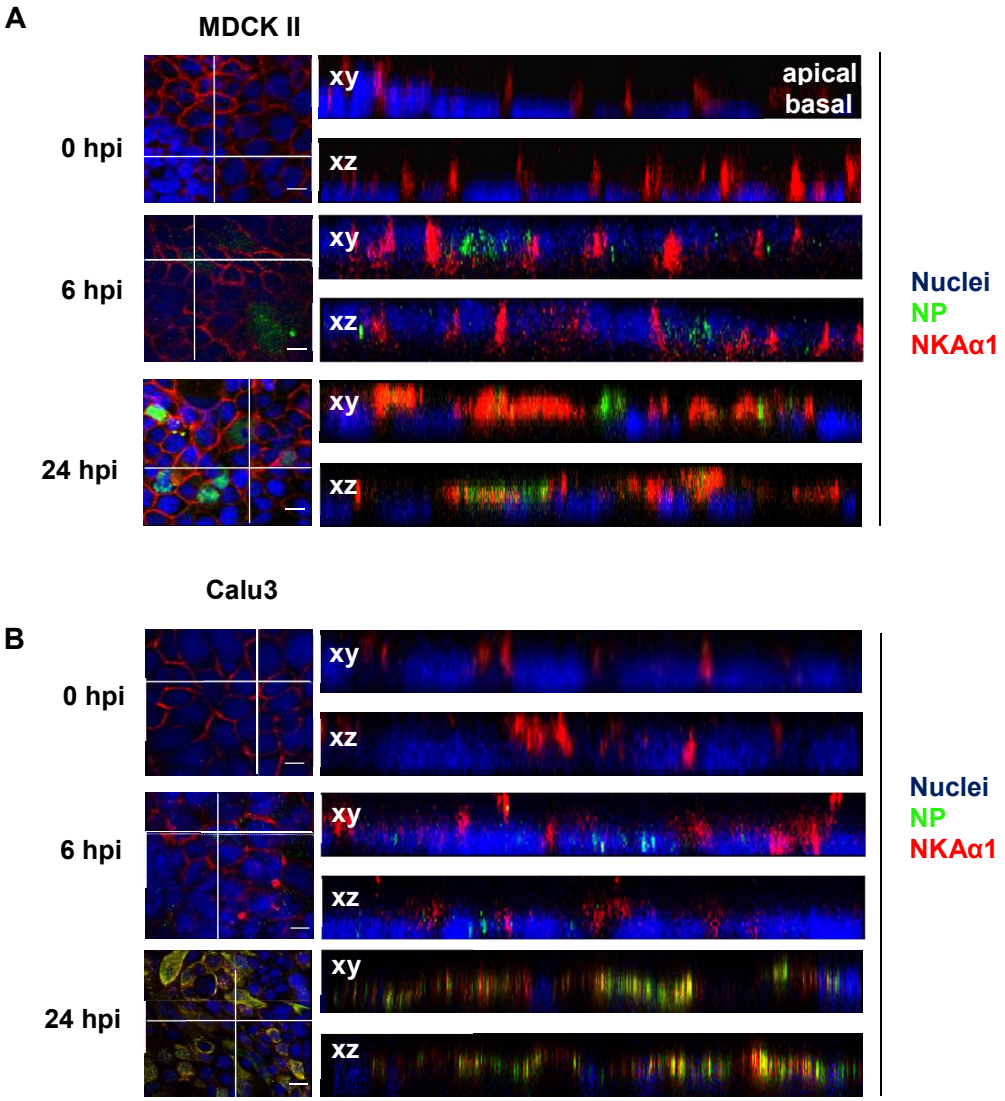

Figure 4-3 Redistribution of NKAα1 within the plasma membrane of infected cells. MDCK II **(A)** and Calu3 **(B)** cells were infected with *PR8* IAV at an MOI 1. At 0, 6 and 24 h p.i. cells were fixed in aceton:methanol (1:1 v/v) and subjected to the immunofluorescence assay with NKAα1- (red) and nucleoprotein (NP) (green)-specific antibodies. Merge – yellow. xy: top view and xz: intersection.

Based on the obtained results of viral growth kinetics, IAV induced reduction of the NKAα1 total amount and detection of IAV-induced apical distribution of NKA in the plasma

membrane of infected cells, the human Calu3 cell line was chosen as the model cell line for the further investigation of the underlying molecular mechanisms of NKA apical mistargeting.

3.2. Calu3 cell line exhibits features of polarized primary alveolar cell

To study the membrane protein redistribution full cell differentiation is required. This is characterized by polarization, e.g. intrinsic asymmetry of the cellular structure and organization, including formation of apical and basolateral cell surfaces separated by tight junctions (TJ). Such apical-basolateral polarization of epithelial cells can be obtained by cultivation of cells on a permeable support[264]. In order to evaluate these characteristics of Calu3 cells as a model of a polarized cell line, cells were cultivated on permeable Transwell® cell culture inserts, either as a liquid-covered culture (Liquid-Liquid Interface – LLI) or as an air-exposed culture (Air-Liquid Interface – ALI). Trans-epithelial electrical resistance (TEER) was measured as a functional parameter of cell monolayer integrity and permeability of tight junctions. 14 days post seeding, cells cultivated at LLI condition showed higher TEER in comparison with those cultivated at ALI conditions, 608 $\Omega \times cm^2$ and 515 $\Omega \times cm^2$, (Fig. 4-4). Maximal TEER of ALI Calu3 culture (577 $\Omega \times cm^2$) was observed on day 21 of cultivation (Fig.4-4).

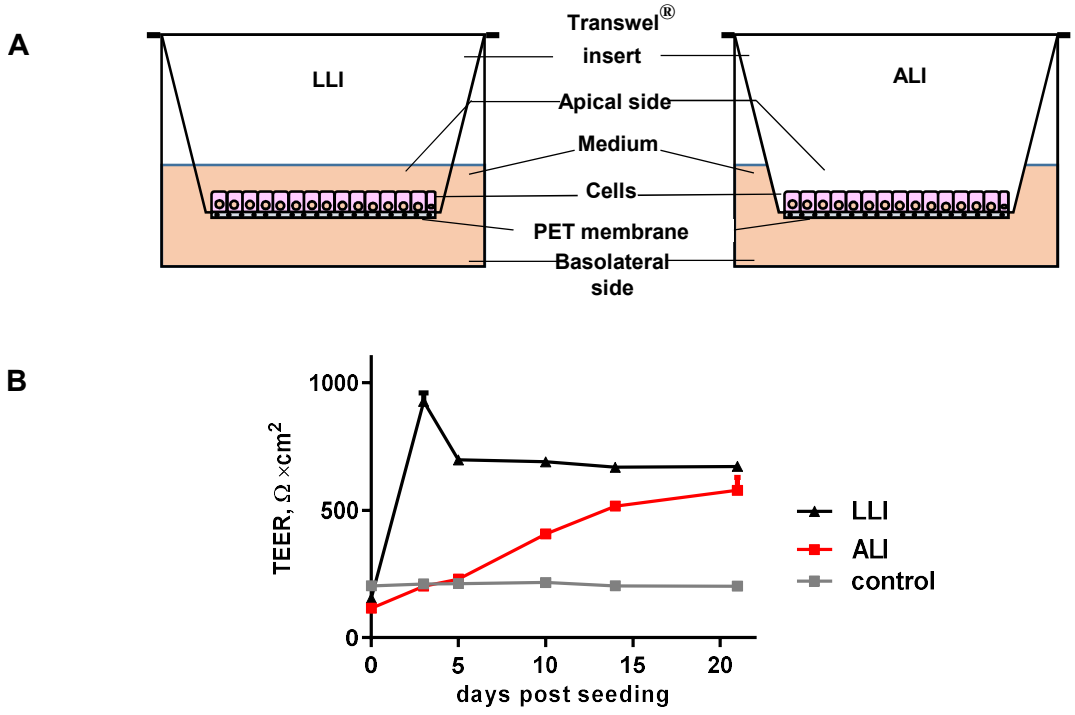

Figure 4-4 Development of TEER in Calu3 cells cultivated at LLI or ALI conditions. (A) Schematic representation of Transwells® inserts cultivation setup of Calu3 cells at LLI and ALI condition. **(B)** Calu3 cells

were cultured on Transwells® inserts at LLI or ALI for 14 days. TEER was measured at the indicated time point. Control - Transwells® inserts without cells. Results represent mean of two independent experiments + SEM, (n=11). PET – polyester.

Morphologically, Calu3 cell cultured at LLI formed a simple columnar epithelium after 14 days of incubation, and pseudostratified columnar epithelial after 21 days at ALI condition (Fig.4-5, A). Interestingly, independent of the cultivation methods, both LLI and ALI cells secreted mucus, which was detected during medium changes and by immunofluorescence analysis with an antibody against mucin 5AC, a glycoprotein that is commonly expressed on apical surface of mucosal (goblet) cell in the respiratory tract (Fig. 4-5, B). ALI culture conditions led to a greater amount of mucus production in comparison to LLI cultivated cells. Localization of β-Tubulin IV – a cytoskeletal protein that is used as a marker of ciliated cell differentiation was investigated in LLI and ALI Calu3 culture. Cells grown at LLI and ALI demonstrated both a diffuse staining pattern of β-Tubulin IV without presence of cilia-like structures on the apical surface (Fig. 4-5, C) indicating that cilia is not formed by Calu3 cells independently of cultivation condition.

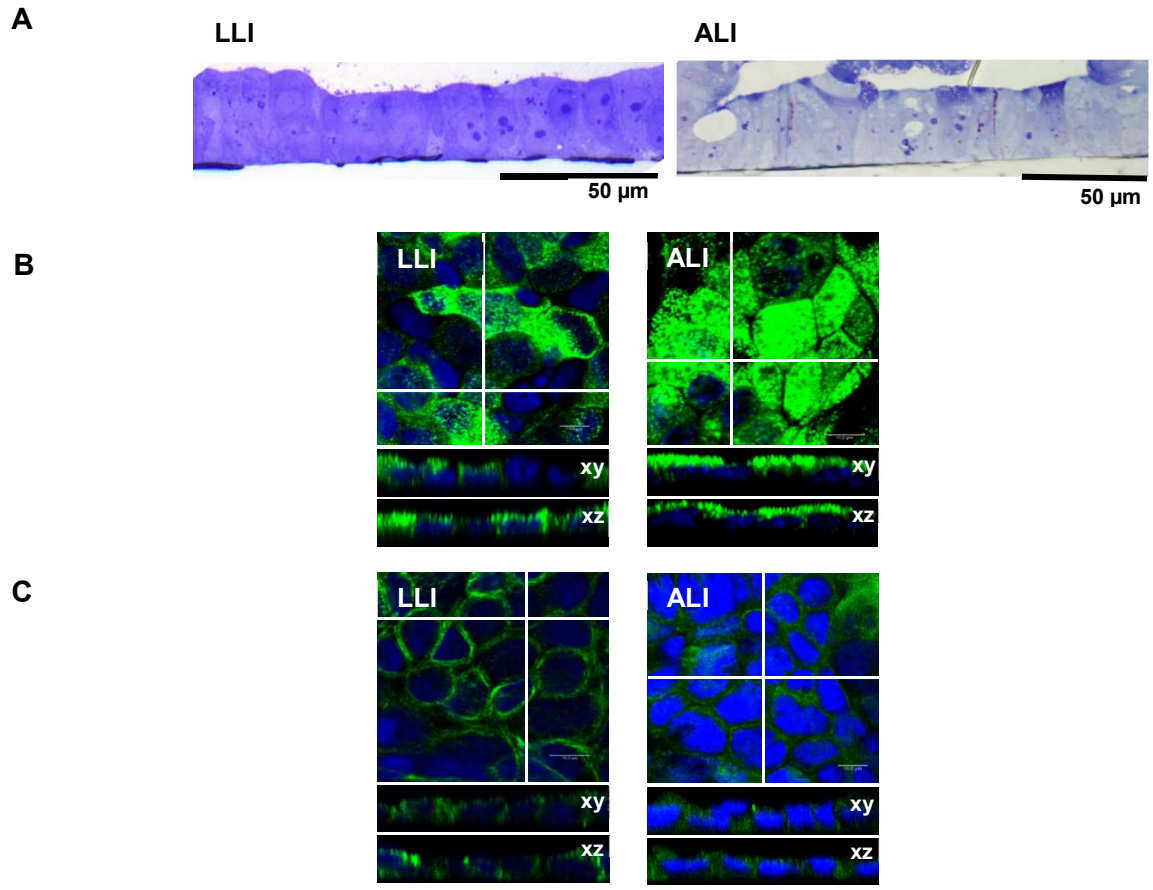

Figure 4-5 Calu3 cells cultivated at LLI or ALI conditions. (A) Thin layer section of 0.5 % Toluidine Blue stained Calu3 cells grown 14 days on permeable membrane at LLI or 21 days at ALI. Section size: 300 nm,

scale bar: 50 µm. The picture of ALI cells was kindly provided by Ms. Jessica Schulze, Division of Influenza and other Respiratory Viruses, Robert Koch-Institute. **(B)** Expression of MUC 5AC protein and **(C)** β-Tubulin IV by Calu3 cells cultivated at LLI (14 days) or ALI (21 days). Cells were fixed with 4% PFA, Optical section thickness: 0.25 µm, scale bar: 10 µm.

As markers of epithelial integrity and tight junction formation, the distribution patterns of TJ proteins occluding and ZO-1 (zonula occludens-1 / tight junction protein-1) were analyzed in LLI- and ALI cultured Calu3 cells, as well as in Calu3 cell monolayer grown on glass cover slips. Z-stack scanning confocal microscopy of polarized LLI and ALI cells revealed a strong fluorescent signal of occludin and ZO-1 only in the first optical sections, when cells were scanned from the top to the bottom (Fig. 4-6, A, B). The signal was distributed as a ring on the perimeter of cells in close proximity to the apical cell membrane (Fig. 4-6, A, B). In the confluent Calu3 cell monolayer cultured on cover slips for 24 hours, ZO1 was detected in the apical cell compartment, whereas occludin was localized to the lateral membrane of the cells (Fig. 4-6, A, B). Taking together, independent of the cultivation conditions (LLI, ALI) Calu3 cells exhibited many characteristics of polarized primary cells, e.g. high TEER, localized expression of tight junction markers and differentiation molecules. Notably, non-differentiated Calu3 cells also demonstrated a polarized distribution pattern of NKA and tight junction markers (data not shown).

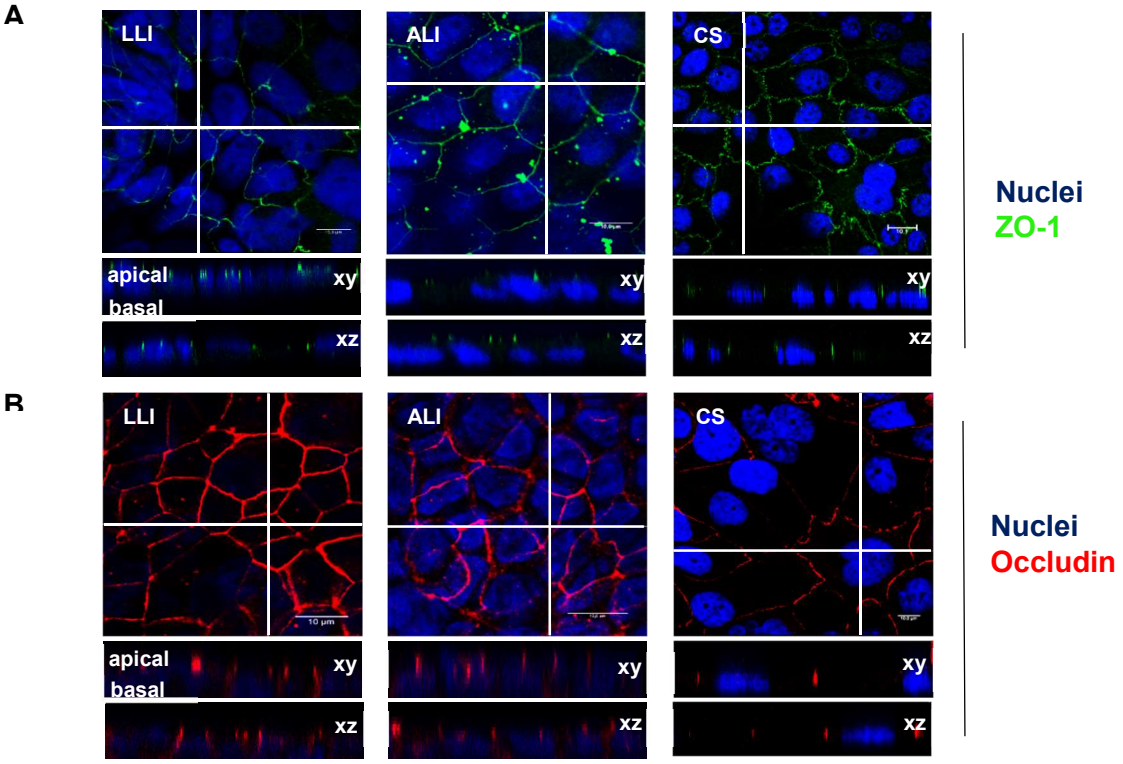

Figure 4-6 Distribution of tight junction proteins in membrane of Calu3 cells cultivated under different conditions. (A) ZO-1 and **(B)** occludin localization in membrane of Calu3 cells grown 14 days at LLI, 21 days at

ALI conditions or 24 h on cover slips (CS). Cells were fixed in 4% PFA; protein localization was addressed by immunostaining and confocal microscopy. Single optical section represents maximum of observed signal. Section thickness: 0.25 µm , scale bar: 10 µm

3.3. Detection of Na^+,K^+-ATPase mislocalization during influenza A virus infection of Calu3 cells

To determine whether cultivation conditions of Calu3 cells affect IAV replication properties, the growth kinetics of *PR8* virus were analyzed. Calu3 cells grown on 12-well plate or on Transwell® inserts at LLI /ALI conditions were infected with *PR8* at an MOI: 2 or 5, respectively. An increased MOI: 5 was used to overcome the reduced infection efficiency in highly polarized Calu3 cells due to the mucus production, which traps the virus particles[265]. Interestingly, neither the growth conditions of Calu3 cells, nor the MOI had a negative effect on the virus titer observed at 20 h p.i.. The virus grew to a titer of 6.2 $\log_{10}$ FFU/ml in Calu3 cells that had been cultivated on culture plate and was not significant different form the virus titer observed in Calu3 cell at LLI or ALI conditions, which was found to be 6.65 $\log_{10}$ FFU/ml and 6.57 $\log_{10}$ FFU/ml, respectively (Fig. 4-7). The increased virus titer at early stage of virus infection of LLI or ALI cells could be explained by a release of not internalized, but mucus/cell-attached virus particles of the inoculum into the culture medium.

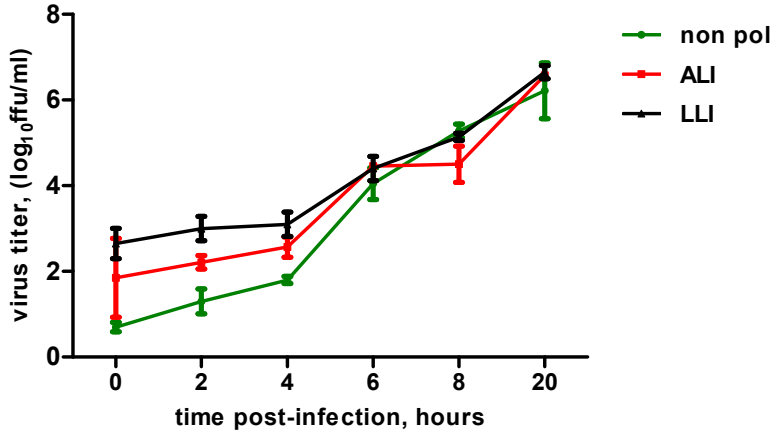

Figure 4-7 Replication of PR8 virus in Calu3 cells cultivated in Transwell ® inserts at liquid-liquid interface (LLI), air-liquid interface (ALI) or in a culture plate. 14-days-old LLI Calu3 cells, 21-days-old ALI Calu3 cells or 24-hours-old monolayer of Calu3 cells were infected with *PR8* virus at an MOI: 5 (cells on the Transwell® inserts) or MOI: 2 (cells on tissue plate) and virus titers were detected at the indicated time points by foci assay. Data represent means ± SD, (n = 4).

To test whether NKA mistargeting indeed takes place also in IAV infected, highly polarized Calu3 cells, ALI cultivated cells were subjected to immunofluorescence analysis with anti- NKAα1 antibody 20 h p.i. followed by 3D modeling. Due to the increased height of polarized columnar epithelial cells in comparison to non-differentiated round polygonal cells (app. 10.25 µm vs 4.5 – 5 µm), the apical NKA expression in infected Calu3 cells at ALI was more prominent. 3D-reconstruction of whole Z-stack image revealed a strong change in the α1 NKA localization pattern – a strong, diffused signal was now also found localized on apical side of infected cells. (Fig. 4-8).

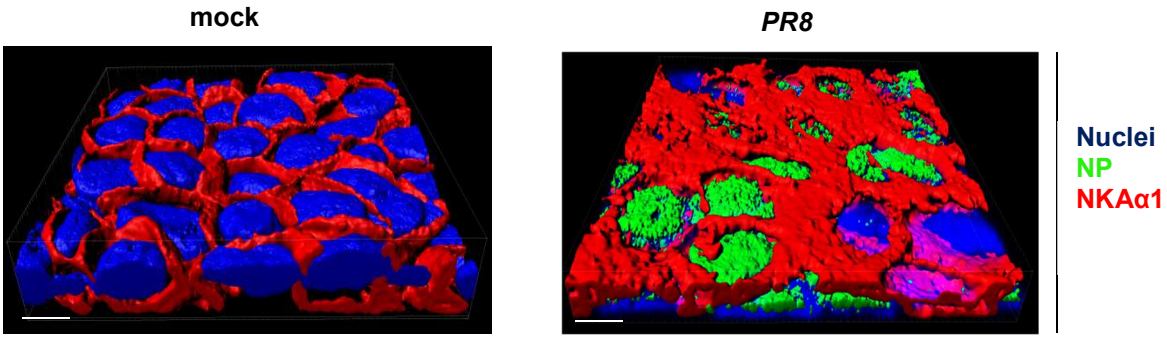

Figure 4-8 Redistribution of NKAα1 within the plasma membrane of infected cells. Highly polarized monolayers of Calu3 cells grown on Transwell® inserts at ALI were infected with influenza virus *PR8* at an MOI 5. 20 h p.i. NKAα1 localization was assessed by an indirect immunofluorescence analysis and subsequent 3D-modeling using Imaris® software (NKAα- (red), viral nucleoprotein (NP) (green), nucleus (blue)). Section thickness –0.25 µm, scale bar – 10 µm.

To quantify the NKA amount in the apical membrane of Calu3 cells at the late stage of IAV infection, biotinylation of apical cell membrane proteins followed by subsequent precipitation and Western-blot analysis was performed. As depicted in Figure 4-9, IAV infection did not affect the amount of apical plasma membrane acid-sensitive ion channel 3 (ASIC3), but induced a significant apical membrane presentation of NKA (Fig. 4-9, A, B).

Previously, it has been described that a polarized distribution of NKA takes place already at an early stage of cell monolayer development and after formation of a cell-cell junction leading to the accumulation of the majority of NKA on the lateral membrane of connected cells[224,228,266]. Therefore, another method to quantify NKA apical localization - "On Cell Western Blotting" (OCWB) - was utilized. Therefore, anti-NKA antibody recognizing only the extracellular domain of the auxiliary β_1-subunit was applied to non-permeabilized Calu3 cells cultivated for only 24 h on 96-well tissue plate. In agreement with the immunofluorescence

analysis (Fig. 4-8) and apical cell membrane protein biotinylation (Fig. 4-9), mislocalization of NKAβ_1 to the apical site was detected also by OCWB assay (Fig. 4-9, C). Despite of being less sensitive when compared to membrane protein biotinylation, OCWB assay generated data were more reproducible.

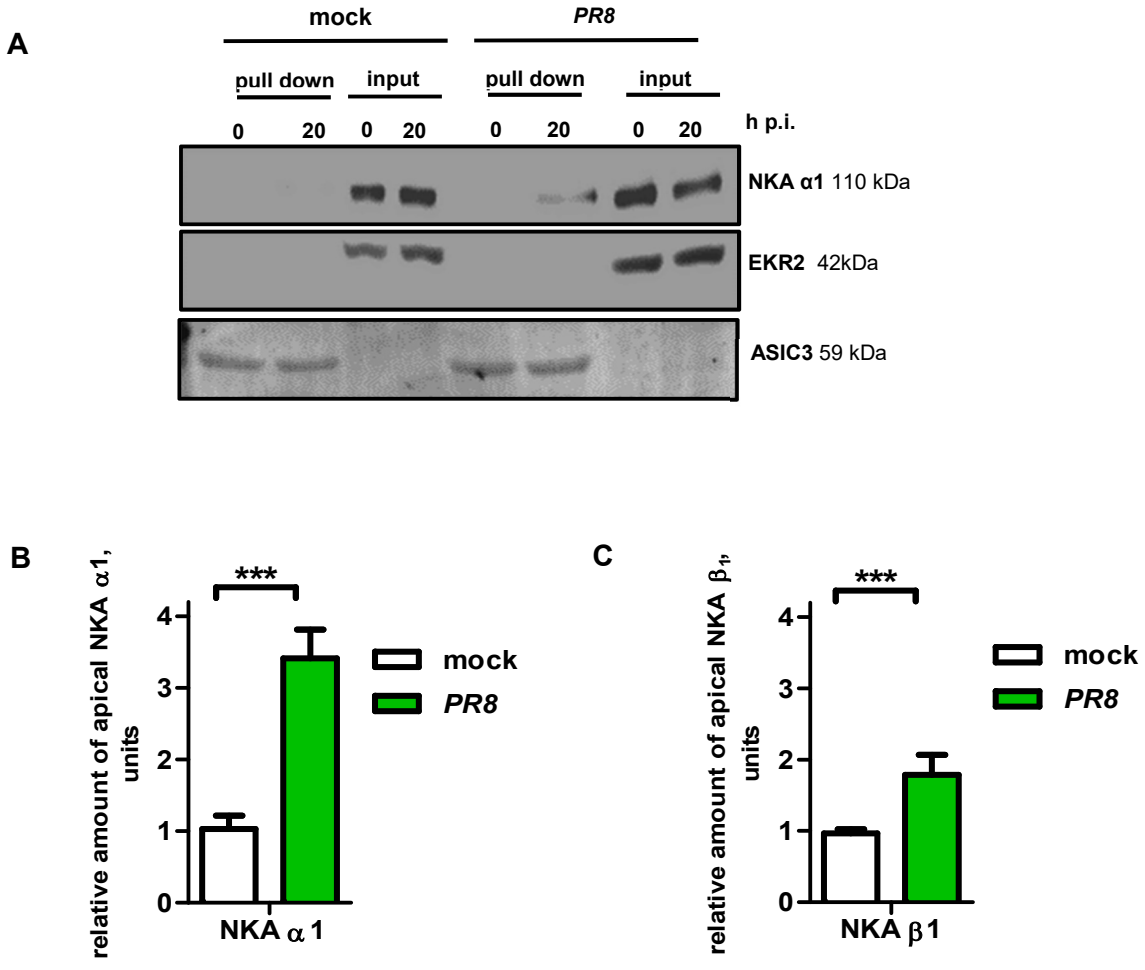

Figure 4-9 NKA quantification on the apical plasma membrane of IAV infected Calu3 cells. Highly polarized monolayer of Calu3 cells grown on Transwell® inserts at ALI condition was infected with influenza A virus *PR8* at an MOI 5 and were subjected to **(A)** to surface labeling of apical proteins via biotinylation, cell lysis and Western-blot analysis using antibodies against NKAα1, ERK2 (cytoplasmic protein control), ASIC3 (apical cellular membrane control). **(B)** Graphical representation of the relative amount of apical presented NKAα1 analyzed by surface biotinylation. Data represent the mean +SD, n=3. **(C)** Graphical representation of the relative amount of apical presented NKAβ_1 analyzed by "On-cell Western blotting" (OCWB). 24 h old H1N1-infected (MOI: 2) Calu3 cells in 96 well plates were analyzed 20 h p.i. by OCWB assay using anti-NKAβ_1 (extracellular domain) antibody to quantified apical amount of NKA. Bar graph represents mean + SD, n=32.

Taken together, IAV-induced mistargeting of NKA, which was previously shown only in primary cells, could also be successfully detected and quantified in the human Calu3 cell line by three different methods, independent from the cultivation conditions.

3.4. IAV-induced redistribution of Na^+, K^+-ATPase in Calu3 cells does not dependent on the viral replication efficiency or the virus subtype

To determine whether the NKA misdistribution during IAV infection is a general characteristic of IAV pathogenicity or is only specific for the tested *PR8* virus, different IAV subtypes were screened for their ability to induce an apical NKA presentation. Firstly, the growth kinetics of influenza virus A/Victoria/3/75 (H3N2), A/Thailand/1 (KAN-1)/2004 (H5N1) or A/Anhui/1/2013 (H7N9) in Calu3 cells were compared. No significant differences in the replication efficiency of the analyzed IAV subtypes and the previously tested *PR8* virus were detected. Highly pathogenic viruses of the H5N1- and H7N9 subtype demonstrated maximal virus titer equal to 6.1 $\log_{10}$ FFU/ml and 7.5 $\log_{10}$ FFU/ml, respectively, 48 h p.i., whereas the less pathogenic H3N2 strain reached a maximal titer of 6.9 $\log_{10}$ FFU/ml 24 h p.i. (Fig. 4-10, A)

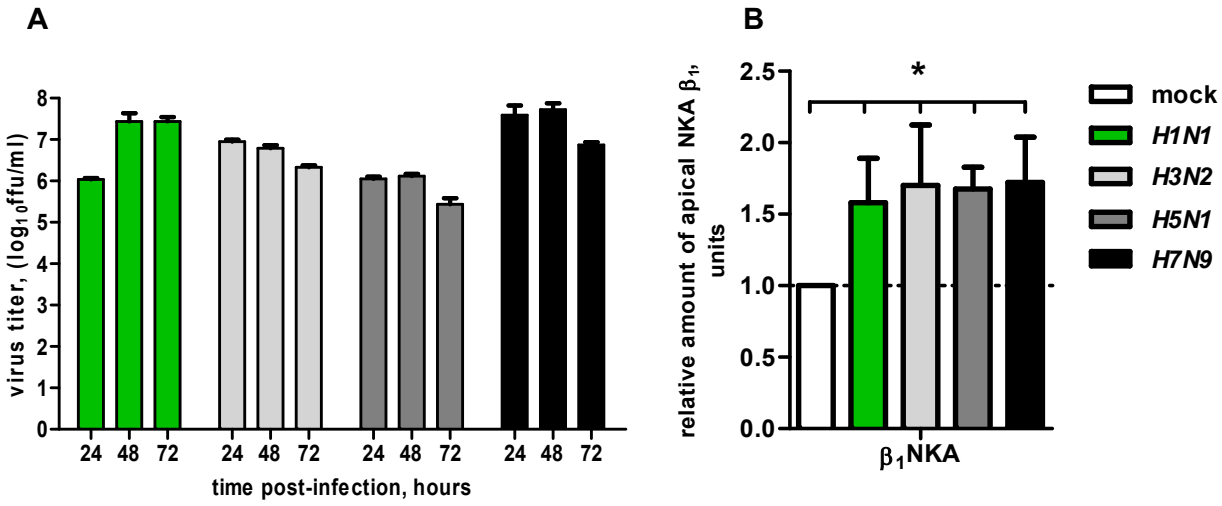

Figure 4-10 Redistribution of NKAβ1 within the plasma membrane of Calu3 cells infected with different IAV subtypes. (A) Growth of different IAV subtypes in Calu3 cells. Cells were infected with the indicated viruses at MOI 0.01 and virus titers were determined by foci assay at the indicated time points. Bar graph represents mean + SD, n=3. **(B)** Quantification of NKAβ1 on the apical membrane of Calu3 cells infected with different strains of IAV. Monolayer of Calu3 cells on 96-well plate were infected with the indicated viruses (MOI: 2) and 20 h p.i. OCWB analysis was performed. Data represent the mean +SD, n=16

All tested viruses were able to induce apical NKA mislocalization at the late stage of viral infection as demonstrated by OCWB analysis (Fig. 4-10, B). There was no significant difference in the capacity to cause apical NKA appearance between the different IAV strains, indicating that this is general effect caused by IAV infection of polarized epithelia cells.

3.5. IAV infection does not induce actin-dependent endocytosis of Na^+,K^+-ATPase from basolateral membrane and manipulation of the actin cytoskeleton and its regulatory molecules does not prevent Na^+, K^+-ATPase mislocalization

Previously, it has been shown that 50% of cellular NKA is distributed within the plasma membrane[267]. The membrane-located NKA undergoes rapid ROCK and ERK coordinated actin-dependent endocytosis from plasma membrane into an intracellular pool during hypoxia-induced generation of ROS or acute hypercapnia, respectively[254,255,268]. IAV infection induces production of ROS in host cells, activates the Ras/Raf/MEK/ERK pathway, ROCK and myosin light chain kinase (MLCK), which is a regulator of contraction and relaxation of the actin cytoskeleton[174,269-277]. Activation of the mentioned pathways was indeed detected in Calu3 cells after infection with *PR8* virus (Fig. 4-11, A). A gradual increase of phosphorylated ERK level, the substrate of mitogen-activated protein kinase kinase (MEK), was observed during viral replication (Fig. 4-11, A). Phosphorylated myosin light chain (pMLC), a substrate for a direct phosphorylation by MLCK and ROCK, was also detected in infected Calu3 cells with a maximum at 6 h p.i. (Fig. 4-11, A). Activity of ROCK was further confirmed by detection of the phosphorylated form of the ROCK target myosin phosphatase target subunit 1 (pMYPT1) 16 and 24 h p.i.. Next, in order to determine whether IAV-induced apical NKA is derived from the BLM-located NKA by actin-dependent endocytosis, the NKA amount on the BLM was analyzed by surface protein biotinylation of the BLM after IAV infection. Interestingly, no reduction of the NKA membrane abundance was observed at late stage of IAV replication (Fig. 4-11, B, C). By contrast, rather a tendency of an increase in the NKAα1 amount was detected (Fig. 4-11, B, C). To test, whether manipulation of the actin organization or inhibition of MEK/ERK, ROCK or MLCK activity can prevent IAV-induced NKA mispolarization, Calu3 cells were treated with either U0126 (,4-diamino-2,3-dicyano-1,4-bis (2-aminophenylthio) butadiene, MEK inhibitor)[278], fasudil HCl (HA-1077, ROCK inhibitor)[279,280] or ML7 (MLCK inhibitor)[281] at non-toxic concentrations after infection with *PR8* virus. The actin-filament disrupting drug cytochalasin D and actin polymerization enhancer jasplakinolide were also used[282,283]. As shown in Figure 4-11 D, inhibition of MEK/ERK, MLCK as well as manipulation of the actin cytoskeleton did not prevent apical mislocalization of NKAβ1 (Fig. 4-12, D). By contrast, activity of Rho kinase was essential for IAV-induced NKA mistargeting. Collectively, these data indicate that BLM localized NKA cannot be a source for apically misguided NKA and the process of NKA mispolarization does not depend on actin cytoskeleton integrity, but is controlled by ROCK activity.

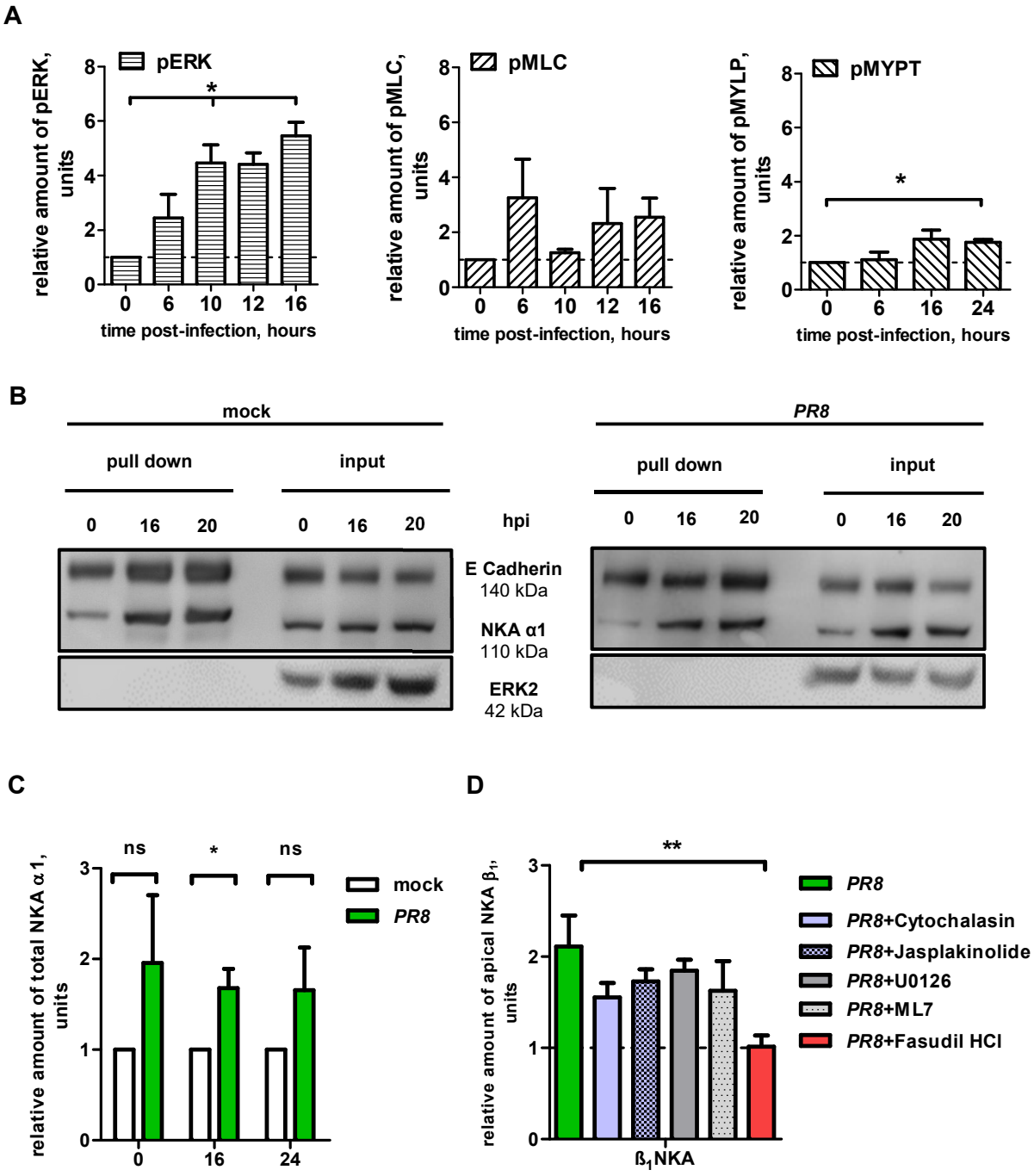

Figure 4-11 Effect of actin targeting reagents and MEK-, MLCK- and ROCK inhibitors on IAV-induced NKA mistargeting. (A) Influenza A virus infection induces phosphorylation of ERK1/2, MYPT-1, and MLC. 24-hours-old monolayers of Calu3 cells were infected with *PR8* at an MOI: 2 and were lysed at the indicated times points. Immunoblotting was performed with antibodies against phosphorylated ERK (pERK), MLC (pMLC) and MYPT (pMYPT1). Bars represent mean +SD, n=3**. (B, C)** Effect of IAV-infection on BLM-abundance of NKA. Highly polarized monolayer of Calu3 (ALI) cells were infected with *PR8* virus at a MOI: 5 and analyzed for NKAα_1 subunit amount in the surface-biotinylated BLM protein fraction by immunobloting. A representative Western-blot for each time point is shown. Bars represent mean +SEM, n=4. **(D)** Detection of NKAβ_1 subunit on the apical surface of IAV-infected Calu3 cells treated with different inhibitors. 24-hours-old Calu3 cell monolayers were infected with *PR8* at an MOI: 2 and treated either with DMSO (control), MEK inhibitor - U0126 (50µM),

MLCK-inhibitor – ML7 (10 µM), cytochalasin D (20µM), jasplakinolide (1µM) or Rho-kinase inhibitor –fasudil HCl (5 µM). "On cell Western-blotting analysis" was performed with anti-NKAβ_1 antibody. Data represent mean +SD, n=16.

3.6. Maturation inhibition of newly produced Na^+,K^+-ATPase does not prevent its mistargeting to the apical membrane of IAV infected Calu3 cells

Another potential source for the apical cell-surface expressed NKA in IAV-infected cells might be the newly synthesized protein subunits of the ion pump. The catalytic α- and the auxiliary β-subunits assemble into the αβ-complex in the endoplasmic reticulum (ER) followed by transport to the Golgi apparatus where they undergo further sugar modification[225]. An inhibition of ER/Golgi transport prevents maturation of newly generated NKA complexes. Therefore, after infection with IAV Calu3 cells were treated with Brefeldin A (BFA), an inhibitor of ER/Golgi vesicular transport[284], and the amount of apically localized NKA was determined. As a control, the amounts of the viral HA and M2 proteins were analyzed, as they are both synthesized in the ER and transported through the trans-Golgi network (TGN) to the apical cell membrane. As presented in Figure 4-12, application of BFA resulted in 2- and 3,7-fold decrease of apical localized M2 and HA, respectively, whereas the amount of detected NKA was not changed in comparison with untreated infected cells. This indicates that the apical presented NKA in IAV-infected cells is not derived from newly produced subunits.

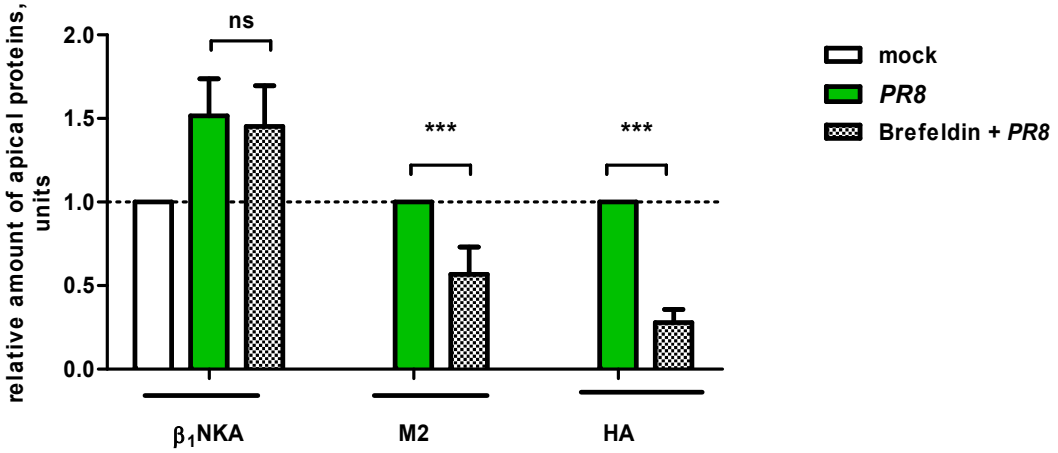

Figure 4-12 Influence of ER/Golgi transport inhibition on NKAβ1 mistargeting to the apical plasma membrane of IAV-infected cells. Calu3 cells were infected with *PR8* virus and BFA (1 µl/ml of provided stock, according to the manufactures' protocol) was added 6 h p.i. Amount of NKAβ1, M2 and HA protein was determined with "On cell Western-blotting assay" 20 h p.i.. Bar graphs represent means +SD, n=32.

3.7. IAV infection modifies subcellular Na^+,K^+-ATPase compartmentalization

A further potential source of mistargeted NKA might be the cellular endosome-enriched fraction, since app. 30% of NKA is localized there[251,267,285]. To test this assumption, cellular NKA compartmentalization in post-nuclear supernatant (PNS) of *PR8*-infected Calu3 cells was analyzed. Western-blot analysis of all fractions was performed with compartment specific antibodies (E Cadherin: a marker of plasma membrane; ERp72: a marker of the luminal endoplasmic reticulum; RCAS1: a Golgi associated protein; Rab11: a recycling endosomal marker and Rab7: a late endosome marker). The intracellular NKA distribution pattern detected was comparable with the distribution pattern for the cytosolic heavy (plasma membrane, ER,) and light (Golgi apparatus) membranes (Fig. 4-13). Interestingly, there was almost no difference in PNS fraction content between infected and non-infected cells, except of recycling endosomal marker distribution - IAV-infection increased the amount number of Rab11-positive fractions (Fig. 4-13). Moreover, NKA and the viral protein NP were presented in the same fractions as Rab11 protein of IAV-infected cells (Fig. 4-13). These results indicate a potential co-localization of NKA, NP and Rab11-positive recycling endosomes that might be involved in the apical membrane transport of NKA during IAV infection.

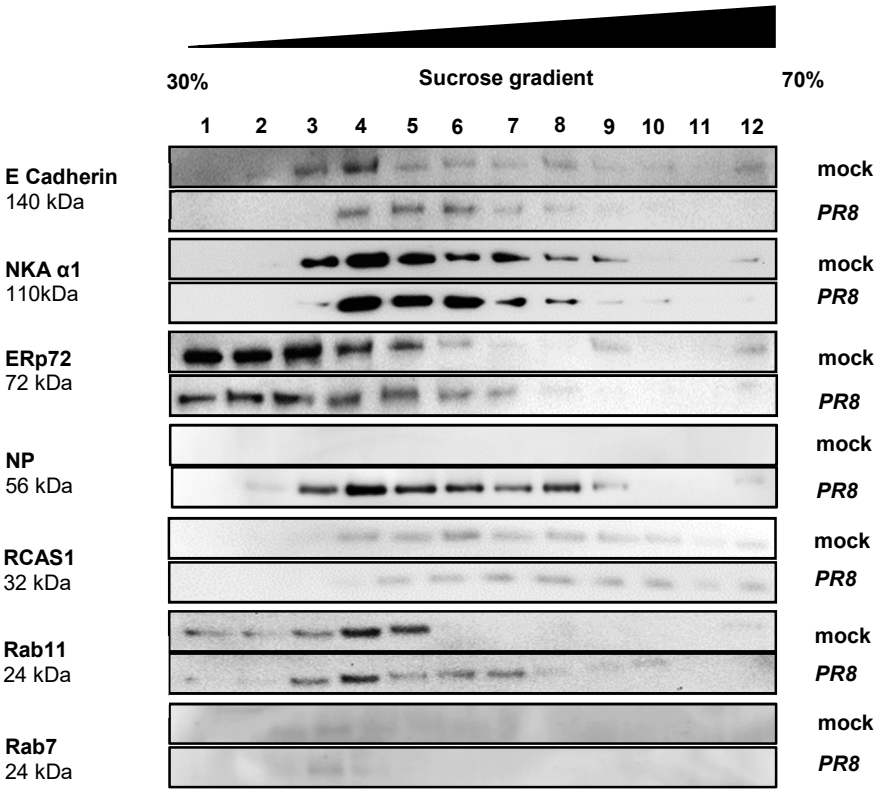

Figure 4-13 Subcellular NKA distribution in IAV-infected Calu3 cells. Cytosolic and plasma membrane proteins were isolated from Calu3 cells infected with *PR8* virus (MOI: 2) 24 h p.i. and subjected to density-gradient

centrifugation. 500 µl volume samples were collected and analyzed by SDS-PAGE following by immunoblotting for indicated marker proteins.

3.8. Microtubules are involved in mistargeting of Na^+,K^+-ATPase IAV-infected Calu3 cells

Several reports demonstrated that during IAV infection vRNPs are transported to the cell surface attached to Rab11-containing vesicles along a microtubule network[146-148,152,161,286]. Since the density-gradient centrifugation analysis revealed that NKA and the recycling endosomal marker Rab11 had a similar distribution pattern in the PNS fractions of infected Calu3 cells (Fig. 4-13), involvement of the tubulin cytoskeleton in mistargeting of NKA was investigated. For this, *PR8*-infected Calu3 cells were treated either with an inhibitor of microtubule polymerization (nocodazole: methyl [5-(2-thienylcarbonyl)-1H-benzimidazol-2-yl)[287] or with a stabilizer of microtubule polymers (paclitaxel: taxol)[288]. A disruption of microtubules by nocodazole as well as the protection from disassembly by paclitaxel prevented apical mistargeting of NKA induced by IAV infection (Figure 4-14). Stabilization of the basolateral NKA distribution at the late stage of virus replication was confirmed by "On cell Western-blotting analysis" and indirect immunofluorescence analysis followed by 3D modeling (Fig. 4-14).

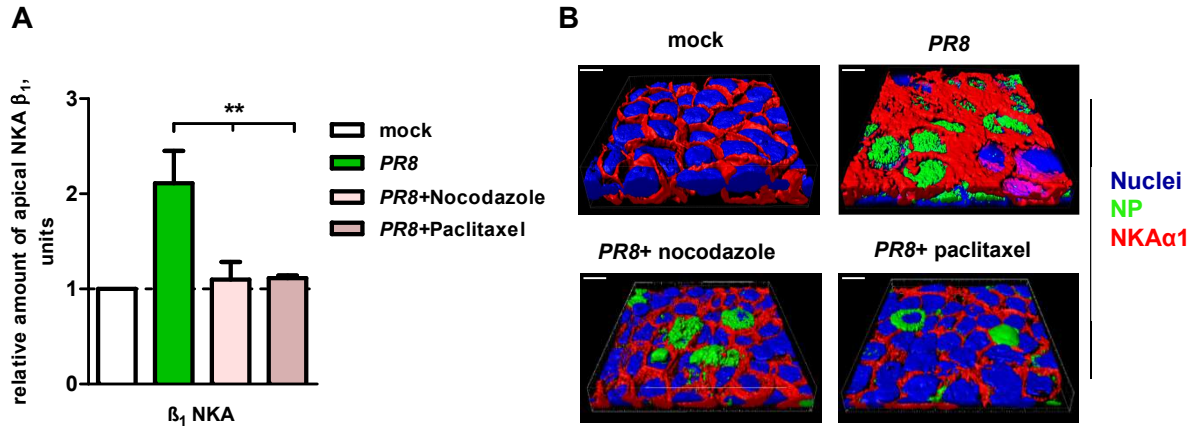

Figure 4-14 Effect of microtubule targeting reagents application on IAV-induced Na^+, K^+-ATPase mistargeting. (A) 24-hours-old monolayers of Calu3 cells were either mock-infected or with *PR8*-infected (MOI: 2) and treated with either DMSO, nocodazole (1µM) or paclitaxel (2 µM) at non-toxic concentrations for 24 hours. "On cell Western-blotting analysis" was performed using anti-NKAβ_1 antibody. Data represent mean +SD, n=16. **(B)** Highly polarized Calu3 ALI cells were either mock-infected or *PR8*–infected (MOI: 5) and treated with either DMSO (control), nocodazole (1µM) or paclitaxel (2µM) for 20 h. NKAα1 localization was assessed by an indirect

immunofluorescence analysis and subsequent 3D-modeling using Imaris® software (NKAα1- (red), viral nucleoprotein (NP) (green), nucleus (blue)). Section thickness: 0.25 µm, scale bar: 10µm.

These data demonstrate a crucial role of the tubulin cytoskeleton integrity and plasticity in mistargeting of NKA.

3.9. Inhibition of Na^+,K^+-ATPase mistargeting in Calu3 cells correlates with reduced IAV titer under ALI culture conditions

To determine whether virus-induced apical cell surface localization of NKA is affecting virus titer, *PR8* infected Calu3 cells were treated with nocodazole, paclitaxel or with ROCK inhibitor (fasudil HCl), since all of three substances were able to prevent NKA mispolarization as shown above. Surprisingly, stabilization of NKA at the BLM by affecting microtubules stability or by ROCK inhibition reduced virus titer only at early times of multicycle replication in Calu3 cells cultivated in 12-well tissue plates (Fig. 4-15, A). At late time points (24 and 48 h p.i.) the decrease of virus production caused by the agents tested was negligible. In contrast, application of nocodazole, paclitaxel and fasudil HCl to the infected ALI-cultured Calu3 cells resulted in a significant reduction of virus titer at each indicated time point, with a maximal virus titer difference observed 24 h p.i. for the nocodozole-treated group (5.3 $\log_{10}$ FFU/ml) compared to the control (6.7 $\log_{10}$ FFU/ml) (Fig. 4-15, B). This indicates that inhibition of NKA mistargeting has a strong effect on virus titer only when Calu3 cells are cultivated under ALI conditions presumably via a decreased water accumulation on apical cell surface leading to an increased viscosity of cell-produced mucus that impedes virus spread.

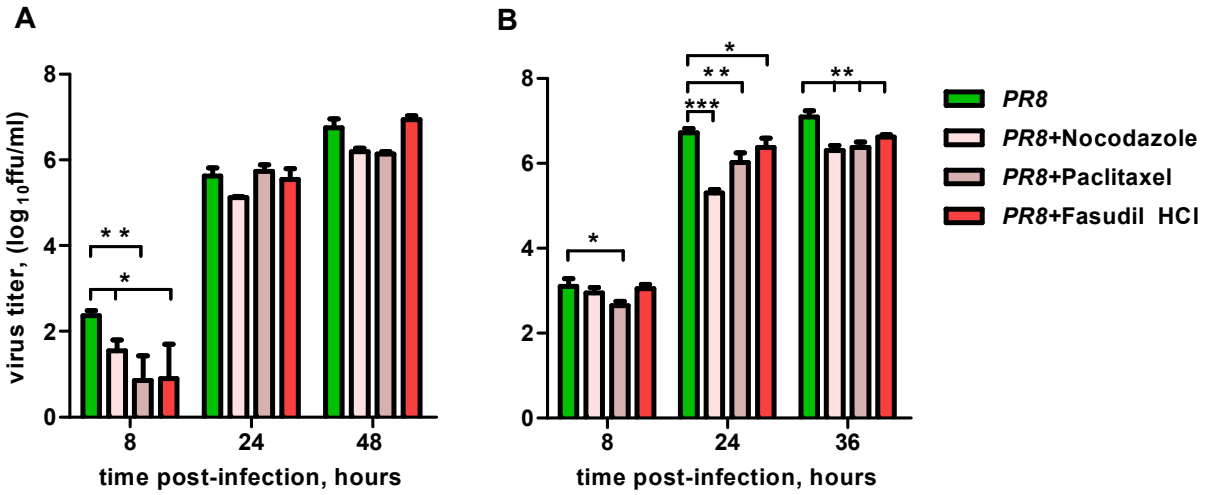

Figure 4-15 Effect of microtubule targeting agents and Rho-kinase inhibitor on the IAV titer. (A) Calu3 cells grown in 12-well plate were infected with *PR8* at an MOI 0.1 and virus titers were determined by foci assay at indicated time points. Data represent means +SD, n=3. **(B)** Highly polarized Calu3 cells cultivated on Transwell® inserts at ALI condition were infected with *PR8* at an MOI 5. At the indicated time points 200 µl of the infection medium was added to the apical chamber and cells were incubated for 15 min at 37 ºC. Supernatants were collected, virus yield was analyzed by foci assay and is presented as means +SD, n=4

3.10. Inhibition of kinesin-1 prevents IAV-induced apical distribution of Na^+,K^+-ATPase

Previously, it has been reported that plasma membrane recruitment of NKA dependents on the kinasin-1-implicated transport of NKA-containing vesicles[257,263]. To examine the involvement of microtubule-associated molecular motor kinesin-1 in the virus-induced NKA mislocalization, Calu3 cells were infected with *PR8* and treated with the competitive kinesin-1 inhibitor adenosine 5′-(β,γ-imido)triphosphate (AMP-PNP), a non-hydrolyzable ATP analogue that stabilizes the molecular motor tightly bound to the microtubule[289-292]. As depicted in Figure 4-16, A, inhibition of kinesin-1 did not have a negative effect on virus titer since no significant difference in virus yield between untreated and AMP-PNP-treated group was detected. Nevertheless, application of AMP-PNP significantly reduced amount of apically mislocalized NKA without affecting an apical distribution of viral HA and M2 protein (Fig. 4-16, B).

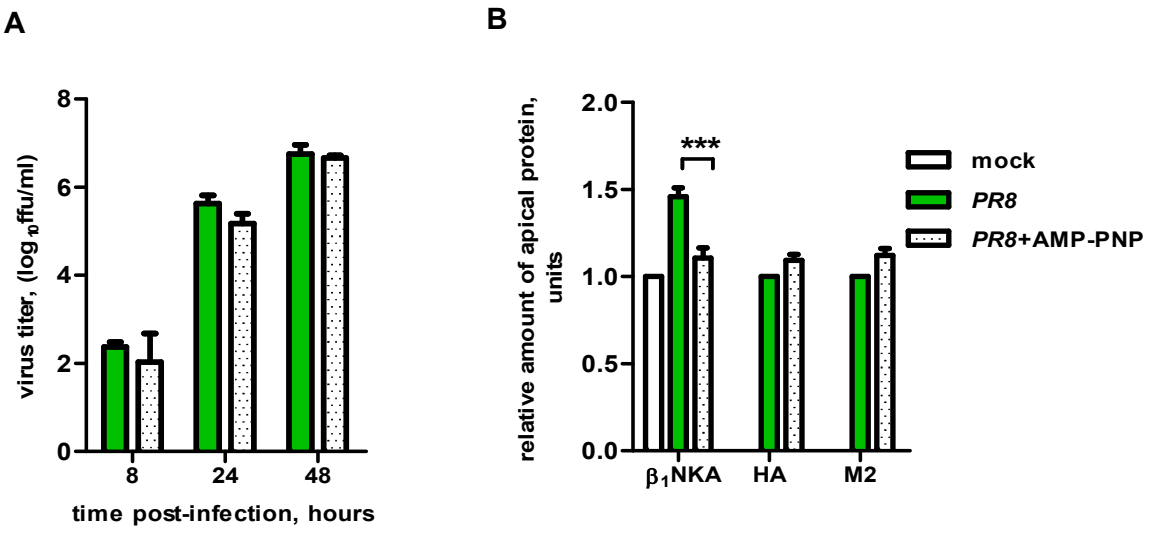

Figure 4-16 Effect of kinesine-1 inhibition on IAV titer and NKA mistargeting in Calu3 cells. (A) Calu3 cells grown on 12-well plate were infected with *PR8* at an MOI 0.1, treated with AMP-PNP (500nM) and virus titers were determined by foci assay at 8, 24 and 48 h p.i.. Data represent means +SD, n=3. **(B)** 24-hours-old monolayers of Calu3 cells were either mock-infected or *PR8*-infected at an MOI 2 and treated with either DMSO

(solvent) or AMP-PNP (500 nM) at non-toxic concentration for 24 hours. OCWB analysis was performed with anti-NKAβ_1-, anti-influenza HA- and anti-influenza M2 antibodies. Data represent mean +SEM, n=24.

These results indicate that the microtubule-associated molecular motor kinesine-1 is actively involved in NKA mistargeting during IAV infection, but is not implicated in the transport of viral proteins or RNPs to the apical membrane of infected cell.

3.11. Rho-kinase inhibition decreases amount of acetylated α-tubulin during IAV infection

Previous *in vivo* motility analysis of fluorescently labeled kinesin indicated that kinesin-1 preferably moves along acetylated microtubules[293-295]. Acetylation of the residue K40 of α-tubulin is one of the several post-translation modifications that regulate dynamic organization of tubulin cytoskeleton and affects intracellular transport events[296-298]. Previously, it has been reported that IAV infection increases α-tubulin acetylation in epithelial cells[165,299]. Therefore, the amount of acetylated α-tubulin (AcTub), as a potential factor that might increase a kinesin-1-dependent transport of NKA-containing vesicles, was evaluated in infected Calu3 cells. In line with published data that indicated an elevated level of AcTub in IAV-infected MDCK and normal human bronchial epithelial (NHBE) cells[299], it could also be demonstrate for Calu3 cells that IAV infection increased amount of AcTub (Fig. 4-17). The peak of AcTub increase (2.8-fold) was observed at 24 h p.i. (Fig. 4-17, B).

As the acetylation status of tubulin is partially regulated by ROCK (Fig. 4-18, A)[300,301] the Rho-kinase inhibitor RKI-1447 (XIII)[302] was applied either to mock-infected or IAV-infected Calu3 cells. In non-treated infected cells the amount of AcTub was increased (Fig. 4-17, A, B), indicating a reduced HDAC6 activity. Nevertheless, XIII inhibitor treatment of IAV-infected cells led to a significant reduction of AcTub amount at the late stage of viral replication (Fig. 4-17, A, B). This indicates that in IAV-infected Calu3 cells ROCK activity is needed for tubulin acetylation, which is pivotal for the kinesin 1-dependent NKA transport/mistargeting in IAV-infected polarized cells (see 3.10).

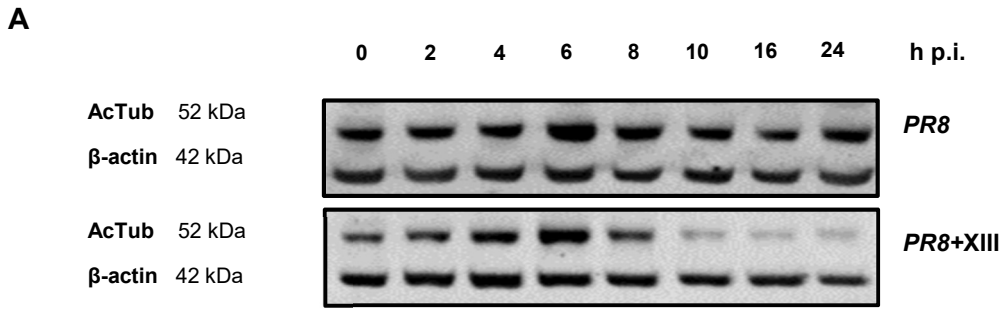

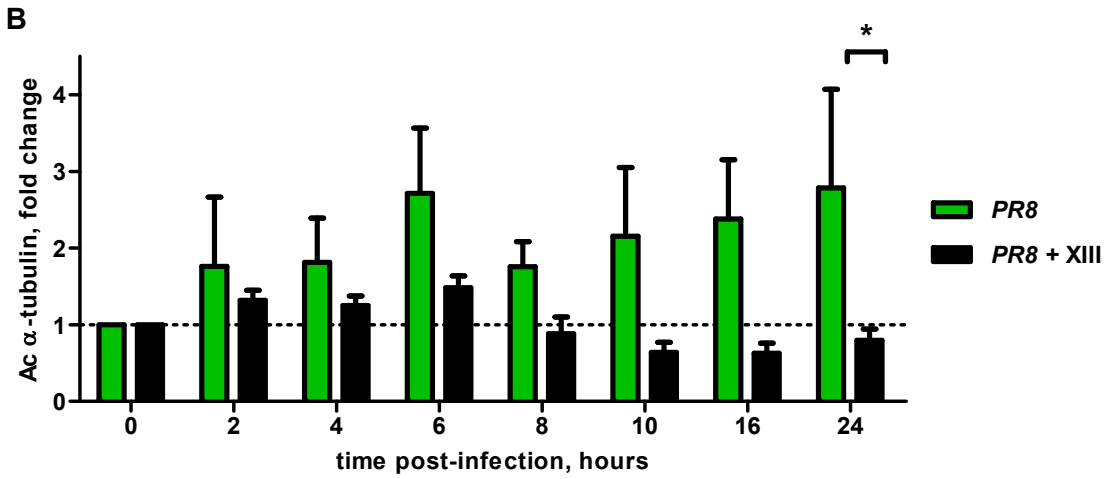

Figure 4-17 Rho-kinase inhibition reduces the amount of acetylated α-tubulin during IAV replication in Calu3 cells. Calu3 cells were infected with *PR8* at an MOI 2 and treated either with DMSO (control) or with Rho-kinase inhibitor RKI-1447 (XIII, 5 µM). Cells were lysed at the indicated time points and lysates were analyzed by immunoblotting with anti-acetylated α-tubulin- and anti-β-actin antibodies. **(A)** A representative western blot for each time point is shown. **(B)** Bars represent mean of signal intensity + SEM, n=5.

3.12. Influence of HDAC6 activity on IAV-induced Na^+,K^+-ATPase mistargeting

Earlier it has been demonstrated, that IAV infection induces caspase-3-mediated degradation of histone deacetylase 6 (HDAC6)[303], one of the enzymes that catalyzes tubulin deacetylation and which is partially regulated by ROCK[303-306] (Fig. 4-18, A). Interestingly, HDAC6 inhibition also improved vRNP-and HA transport to the cell surface, increasing the release of IAV particles from infected cells[165]. As caspase-3-mediated HDAC6-degradation results in increased acetylation of microtubules[303], the role of HDAC6 in the virus-induced NKA mistargeting was analyzed. OCWB assay was performed with *PR8*-infected Calu3 cells (+/-) treatment with the selective HDAC6 inhibitor tubacin[304]. Inhibition of HDAC6 slightly raised the apical membrane NKA amount of infected Calu3 cells (1.45 to 1.53 relative units) while the amount of viral HA and M2 protein was significantly elevated (Fig. 4-18, C).

The fact that HA and M2 transport is not negatively affected by HDAC6 inhibition was also reflected in the virus titer of tubacin-treated cells, which was not reduced by HDAC6 inhibition 24 and 48 h p.i.. A maximal virus titer difference between infected non-treated and infected and tubacin-treated cells of 6.7 $\log_{10}$ FFU/ml vs 7.3 $\log_{10}$ FFU/ml, respectively, was observed at 48 h p.i. (Fig. 4-18, B). In contrast, 8 h p.i. tubacin application resulted in reduced virus titers, which could be related to the fact that HDAC6 also participates in the fusion and uncoating process early in infection[305].

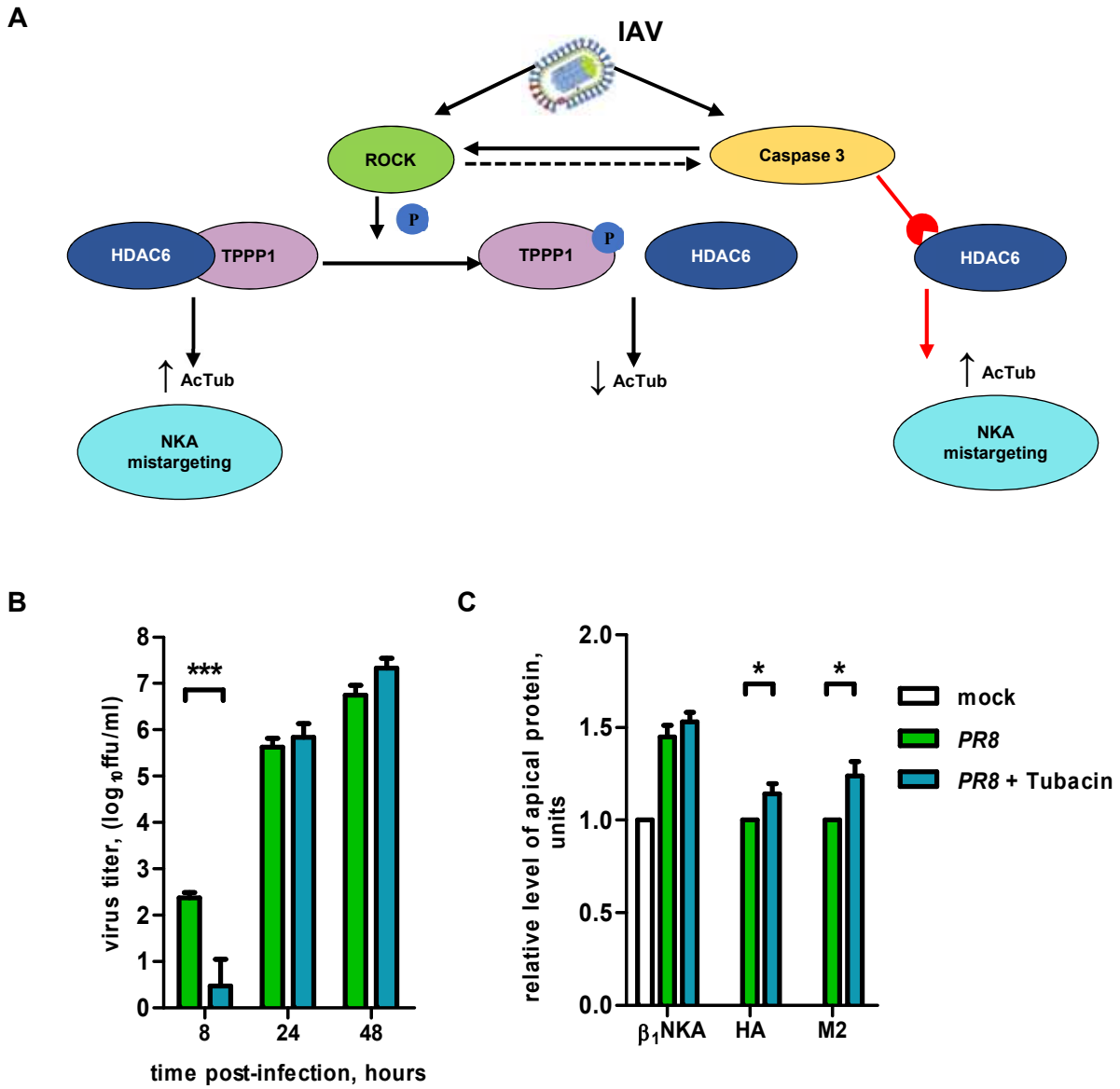

Figure 4-18 Influence of HDAC6 activity on IAV replication and mistargeting of NKAβ1 within the plasma membrane of infected cells. (A) Schematic representation of HDAC6 regulation by ROCK and caspase-3 **(B)** Calu3 cells grown on 12-well plate were infected with *PR8* at an MOI 0.1, treated with tubacin (10 µM) and virus titers were determined by foci assay at the indicated time points. Data represent means +SD, n=3. **(C)** Calu3 cells were infected at an MOI 2 with *PR8*, treated with HDAC6-inhibitor – tubacin (10 µM) and the apical membrane NKA amount was analyzed by OCWB assay with anti-NKAβ_1-, anti-HA- and anti- M2 antibodies 24 h p.i.. Data represent mean +SEM, n=24. Solid line – a direct interaction, dashed line – indirect interaction.

3.14 Effect of ROCK inhibition on IAV-induced caspase-3-dependent HDAC6-degradation

As in IAV-infected cells HDAC6 is degraded by virus-induced caspase-3[299,303], the total amount of cellular HDAC6 and of activated caspase-3 during the time course of IAV infection

of Calu3 cells was analyzed. As indicated (Fig. 4-19, A), IAV-infection induces proteolytic cleavage of HDAC6 late in the replication cycle, at 16 and 24 h p.i.. This is consistent with the above observation of increased α-tubulin acetylation in IAV-infected Calu3 cells (Fig. 4-17). Concurrently, the large (17/19-kDa), active subunit of caspase-3 was detected in lysates of the infected cells at 16 and 24 h p.i., (Fig. 4-19, B). Comparing the results regarding the reduced amount of HDAC6 with the increased activation status of caspase-3 over time, demonstrates that the presence of cleaved/active caspase-3 correlated with the degradation of HDAC6. These results support the assumption that also in IAV-infected Calu3 cells the amount of active HDAC6 is (in part) regulated by virus-induced caspase-3.

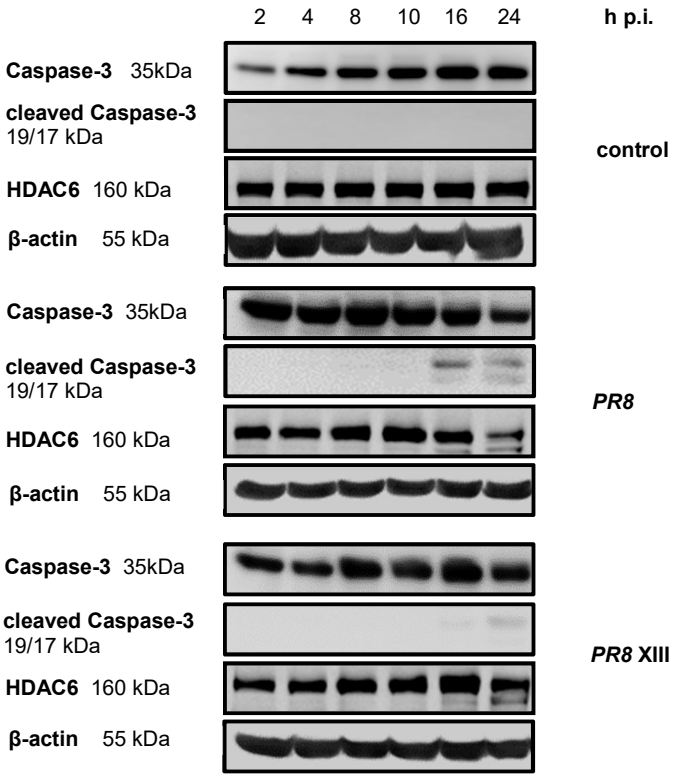

Figure 4-19 Effect of ROCK inhibition on cellular HDAC6 amount and caspase-3 activation during IAV infection. Calu3 cells were infected with *PR8* at an MOI 2 and treated either with DMSO (control) or with Rho-kinase inhibitor XIII (5 μM). Cells were lysed at the indicated time points and lysates were analyzed by immunoblotting with anti-caspase3, anti-HDAC6 and anti-β-actin antibody.

As ROCK can indirectly activate caspase-3 by various pathways,[306] the effect of ROCK inhibition on IAV-induced caspase-3 activation was investigated. When infected cells were treated with the ROCK-inhibitor XIII, proteolytic caspase-3 activation was weak and delayed to 24 h p.i. compared to the infected non-treated cells (Fig. 4-19). Likewise, cleavage of HDAC6 was also delayed, as a prominent truncated form of HDAC6 could only be detected at

24 h p.i. (Fig. 4-19). This indicates that also in IAV-infected Calu-3 cells HDAC6 activity is partially affected via ROCK-regulated caspase-3 activity.

Interestingly, the addition of the specific, irreversible caspase-3 inhibitor Z-DEVD-FMK[307,308] as well as the ROCK inhibitor XIII, to IAV-infected Calu3 cells had the same effect on caspase-3 activity, measured 24 h p.i. by an activity assay. The 1.35-fold increased caspase-3 activity in *PR8*-infected non-treated Calu3 cells was reduced to 1.07- and 1.08- fold after treatment with Z-DEVD-FMK or XIII, respectively (Fig. 4-20). Taken together the results indicate that the ROCK inhibitor impaired IAV-induced activity of caspase-3. This further points out that in IAV-infected cells caspase-3 activity is involved in promoting α-tubulin acetylation via degradation of HDAC6 and thereby supporting NKA mislocalization.

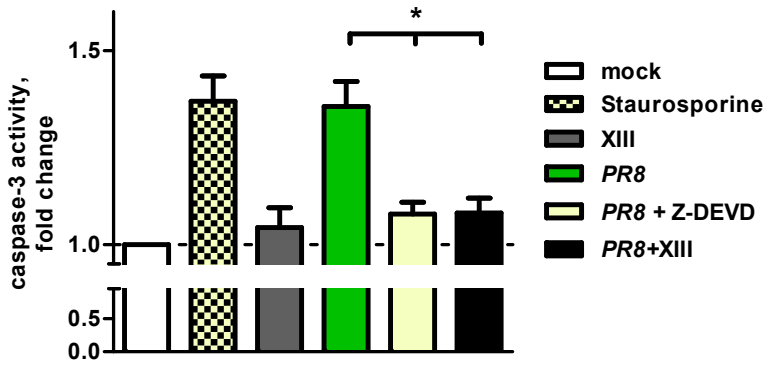

Figure 4-20 Influence of ROCK inhibition on caspase-3 activity in IAV-infected cells. Calu3 cells were either mock-infected or *PR8*-infected (MOI: 2) and subsequently treated either with DMSO, caspase activator (staurosporine,1 µM), Rho-kinase inhibitor (XIII, 5 µM) or caspase-3 inhibitor (Z-DEVD-FMK, 40 µM). Cells were lysed 24h p.i. and lysates were analyzed for caspase-3 activity with Caspase-3 Colorimetric Protease Assay Kit. Data represent mean +SEM, n=4.

3.13. Influence of caspase-3 inhibition on IAV-induced apical distribution of Na^+,K^+-ATPase.

The results so far indicated, that in virus-infected Calu3 cells IAV-induced caspase-3 activity regulates the amount of HDAC6 (Fig. 4-19), and that HDAC6 activity affects NKA mistargeting (Fig. 4-18). In order to further elucidate a role of caspase-3 activity in NKA mistargeting during IAV infection, the caspase-3 inhibitor - Z-DEVD-FMK (40 µM) was added to Calu3 cells after infection with *PR8* and the amount of NKA on the apical cell membrane was analyzed by OCWB assay. Z-DEVD-FMK treatment slightly reduced amount of apically localized NKAβ_1, but the level of reduction was not significantly different from non-treated

PR8-infected cells – 1.3 vs 1.41 relative units, respectively, whereas the abundance of the viral HA and M2 proteins on the cell surface was significantly reduced (Fig. 4-21). It should be noted that caspase-3 can also activate ROCK[306] (Fig. 4-18, A). The inhibition of caspase-3 could therefore lead to less active ROCK and this should result in less free/active HDAC6 (Fig.4-18, A). This might explain the modest reduction of NKA mistargeting after caspase-3 inhibition.

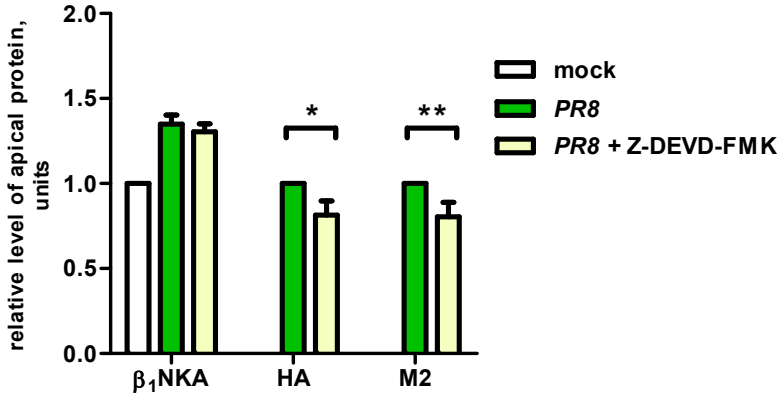

Figure 4-21 Effect of caspase-3 inhibition on IAV-induced NKA mislocalization in Calu3 cells. Calu3 cells infected with *PR8* at an MOI 2, were either treated with caspase-3-inhibitor (Z-DEVD-FMK, 40 μM) or left untreated and apical redistribution of NKA was analyzed by OCWB assay with anti-NKAβ_1-, anti-HA- and anti-M2 antibodies. Data represent mean +SEM, n=24.

3.14. ROCK-inhibition improves vectorial water transport during IAV infection

The basolateral distribution pattern of NKA is one of the major determinants in establishment of the osmotic sodium gradient that plays an important role in effective vectorial fluid transport. To determine whether prevention of apical NKA distribution during IAV-infection could improve vectorial water transport, highly polarized LLI cultures of Calu3 cells were infected with IAV and overlaid with culture medium, containing FITC-dextran +/- inhibitors that had demonstrated to reduce IAV-induced NKA mistargeting. The concentration difference of FITC-dextran between the apical and basal chamber of the Transwell® chamber was analyzed 8 and 24 h p.i.. As a control, cells were treated with amiloride, an inhibitor of most plasmatic sodium transport systems [309]. IAV-infection induced a drastic drop in the efficiency of water transport through the monolayer of cells as well as the amiloride treatment (Fig. 4-22). Application of kinesin-1 inhibitor (AMP-PNP) had a tendency to increase the capability of IAV-infected Calu3 cells for vectorial water transport (Fig. 4-22). Treatment of the cells with ROCK-inhibitor XIII significantly improved vectorial water transport at 8 and 24 h p.i. (Fig. 4-22). This indicates that prevention of NKA mistargeting has a positive effect on physiological characteristics of the IAV-infected Calu3 cell monolayer.

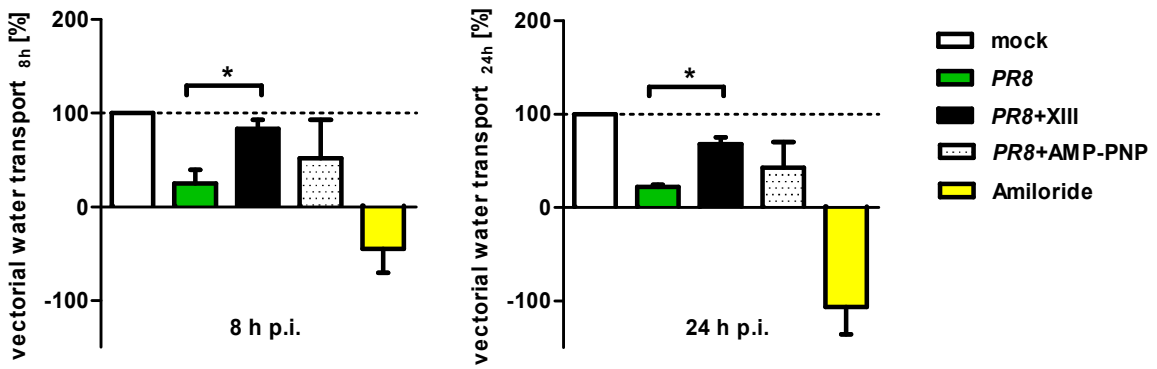

Figure 4-22 Inhibition of Na^+, K^+-ATPase mispolarization in IAV-infected Calu3 cells improves vectorial water transport. 14-days-old monolayers of Calu3 cells on Transwell® inserts were infected with *PR8* (MOI 2) and treated with either DMSO (control), Rho-kinase inhibitor XIII (10 µM), kinesin-1 inhibitor (AMP-PMP) or amiloride (a negative regulator of water transport) (0.5 µM). Vectorial transport of water through the monolayer of Calu3 cells was determined by changes of FITC-dextran (70 kDa) concentrations in apical and basal cell culture media 8 and 24 h p.i.. Data represent mean +SEM, n=3.

Interestingly, application of the ROCK-inhibitor (XIII) to Calu3 cells infected with a high dose of IAV (MOI: 5) improved the structure of cell monolayer, which is illustrated by Figure 4-23.

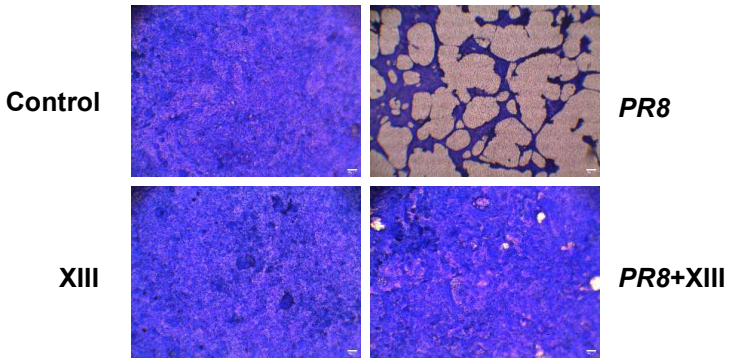

Figure 4-23 Inhibition of ROCK reduced IAV-induced damage of the Calu3 cell monolayer. Highly polarized Calu3 cells cultivated under LLI conditions were either mock-infected or *PR8*-infected, treated with DMSO or XIII and stained with 2.5% Coomassie-dye 24 h p.i. Pictures obtained with EVOS FL Auto Cell Imaging System, objective magnification ×10, scale bar: 100 µm.

3.15. Application of ROCK-inhibitor reduces virus titer and improves IAV-induced lung injury *in vivo*

Next, to investigate whether the ROCK inhibition could improve alveolar fluid clearance during IAV-induced acute lung injury *in vivo*, mice were infected with *PR8* by intra-tracheal (IT) inoculation of 500 plaque-forming units (pfu) per mouse (work performed in collaboration

with Prof. Dr. S. Herold, by Balachandar Selvakumar, PhD). During the next 6 days, the mice were daily treated with the clinically approved ROCK-inhibitor "fasudil HCL". Intra-peritoneal (IP) injections of fasudil did not lead to a significant change in the body weight loss induced by IAV-infection during a seven days observation period (Figure 4-24).

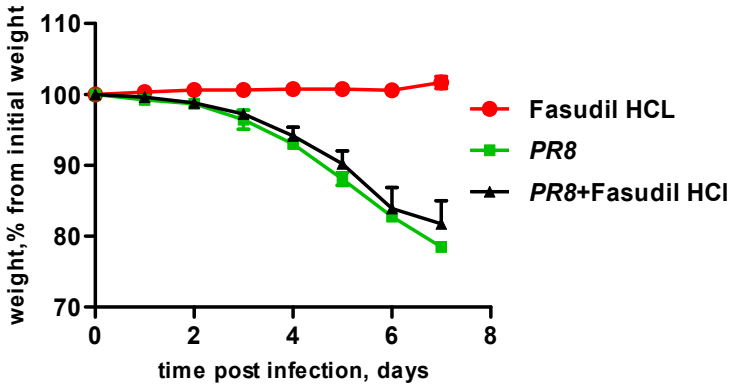

Figure 4-24 Effect of fasudil HCl treatment on body weight of IAV-infected mice. C57BL/6 mice were IT-infected with 500 pfu of *PR8* per mouse and on day 1, 2, 3, 4, 5, 6 p.i. 10 mg/kg of fasudil HCl in 100 µl of sterile saline was administrated by IP injection. Body weight was measured daily before fasudil administration. Data represent mean +SD, n=5.

Nevertheless, ROCK inhibition had a significant effect on pulmonary edema, defined as the wet/dry weight ratio of lung tissue. The values of wet/dry ratios were significantly increased in the *PR8*-infected group, indicating a fluid accumulation (Fig. 4-25). However, the application of fasudil significantly decreased these values compared with the non-treated IAV-infected group (Fig. 4-25).

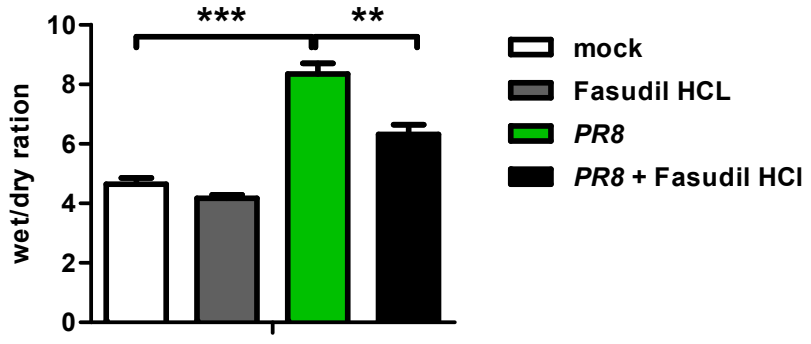

Figure 4-25 Effect of fasudil HCl treatment on IAV-induced alveolar edema. Six-week-old C57BL/6 mice were anesthetized, either mock-infected or PR8-infected (500 pfu) by IT inoculation and were treated with sterile saline or fasudil HCl during the next 6 days. (A) Wet/dry weight ratio of lung tissues were analyzed 7 days p.i.. Data represent mean + SEM, n=5.

Furthermore, virus titer analysis of the lungs from infected mice revealed a reduction of virus titer in the lung homogenates of infected mice when fasudil was applied (Fig. 4-26, A, B). The titer of *PR8* virus in control group was equal to 2, 9 $\log_{10}$ FFU/ml (100%), whereas in fasudil-treated group the virus only reached a titer 0, 8 $\log_{10}$ FFU/ml (1, 3 %) (Fig. 4-26, A, B).

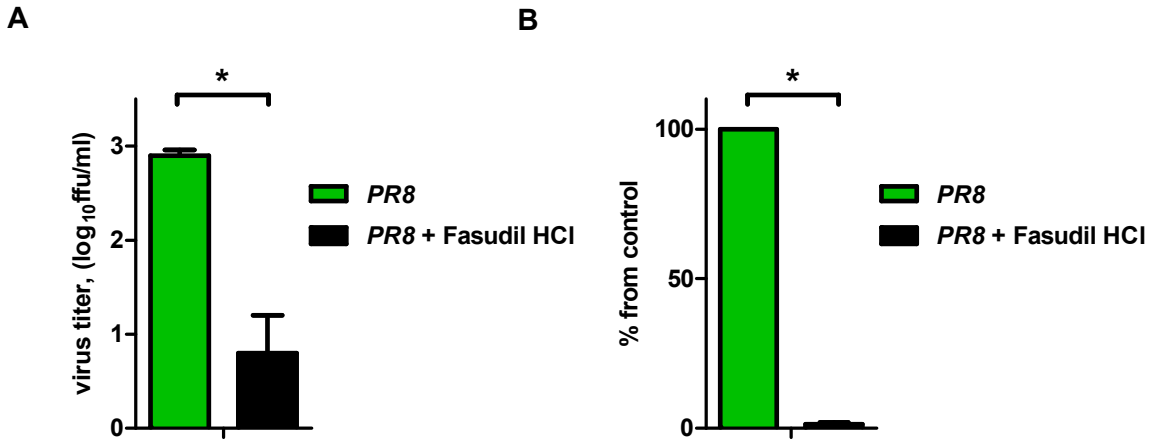

Figure 4-26 Effect of fasudil HCl treatment on IAV replication *in vivo*. Six-week-old C57BL/6 mice were IT mock-infected or PR8-infected (500 pfu) under narcosis and were treated with sterile saline or fasudil HCl during the next 6 days. On the day 7, lungs were isolated and the virus titer in lungs of infected mice was quantified by foci assay and represented as a $\log_{10}$ffu/ml **(A)** or as percent from control **(B)** – infected not-treated group. Data represent mean + SD, n=3.

Histological analysis of lung tissues (work performed in collaboration with Univ.-Prof. Dr. Achim Gruber) demonstrated massive pathological changes – necrosis of alveolar walls, desquamated type II pneumocytes and multiple leukocyte infiltrates in *PR8*-infected mice (Fig. 4-27, A,). Interestingly, lung injury in the *PR8*-infected fasudil-treated animals was less pronounced and less severe than in untreated IAV-infected mice (Fig. 4-27, A).

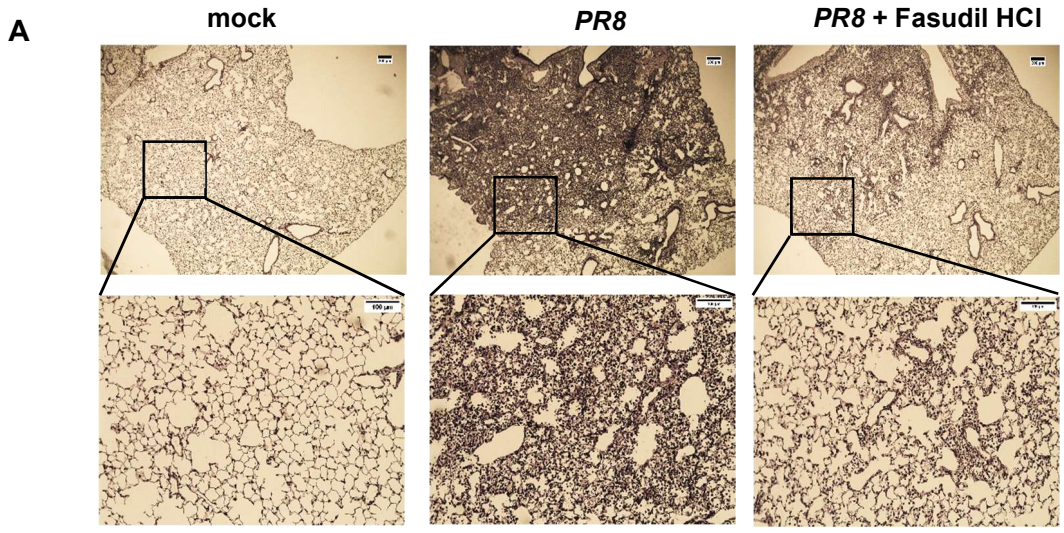

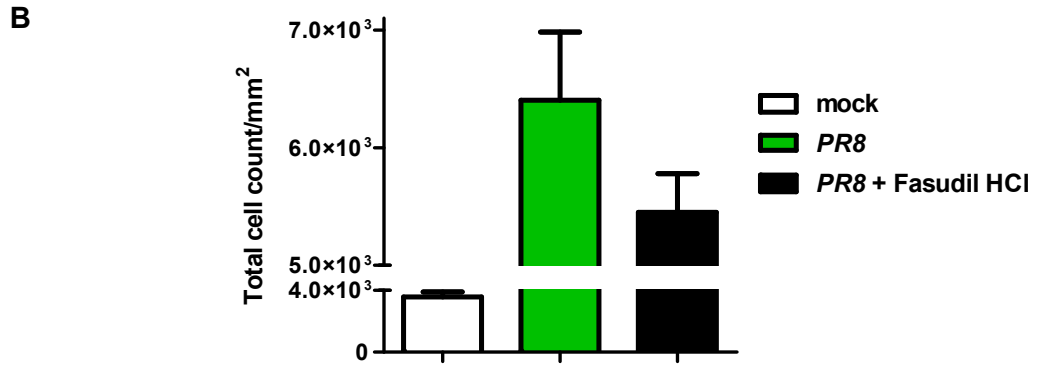

Figure 4-27 Effect of fasudil HCl treatment IAV-induced lung infiltration. Six-week-old C57BL/6 mice were anesthetized, either mock-infected or *PR8*-infected (500 pfu) by IT inoculation and were treated with sterile saline or fasudil HCl during the next 6 days. **(A)** Representative hematoxylin-eosin-stained mouse lung sections are shown. Section thickness - 3.5 µm, scale bar – upper row – 200 µm (objective magnification - ×4), lower row – 100 µm (objective magnification: ×20). **(B)** Total amount of cells per mm^2 of mouse lung specimens. Data represent mean + SEM, n=5.

Moreover, when a total cell count per square millimeter of lung specimens was analyzed, the fasudil-treated group demonstrated a reduction in infiltrated cell amount (5450.8 cells per mm^2) when compared with non-treated group (6404.7 cells per mm^2), supporting the optical observation of lung infiltration reduction (Fig. 4-27, B).

Collectively, these data demonstrate that inhibition of IAV-induced ROCK activity prevents tubulin-dependent mistargeting of the Na^+, K^+-ATPase, reduces virus titer, increases alveolar fluid clearance capacity and reduces IAV pathogenesis *in vivo*.

4. Discussion

In severe cases, human IAV infection can lead to development of ARDS that is characterized by accumulation of a protein-reach fluid within the alveolar lumen in its exudative phase. ARDS is generally associated with high mortality. Alveolus flooding is a result of IAV-induced immune cell-mediated damage of the alveolar epithelial-endothelial barrier and an infringement of the osmotic gradients, especially the Na^+ gradient, in the alveolar microenvironment that negatively affects pulmonary fluid homeostasis.

In the present work, IAV-induced apical mistargeting of the epithelial NKA at the late stage of viral infection was investigated since NKA is usually localized on the basolateral plasma membrane and plays an important role in alveolar edema clearance, as it was described earlier[197,204,236,249,310]. Previously, it has been shown that IAV negatively regulates the activity and the abundance of the apical membrane-localized ion channels – ENaC and CFTR that are involved in the establishment of an osmotic gradient[210-213,311-314]. IAV membrane attachment and replication induces activation of protein kinase C (PKC) that results in ENaC internalization and degradation, whereas impairment of the CFTR amount and function is depending on an IAV M2 protein-associated alternation of the cellular trafficking machinery[210,213,311,313,314] and this is currently believed that these changes are a major factor for fluid accumulation contributing to pulmonary edema formation. An active Na^+ transport over NKA that is localized on the basolateral membrane of alveolar epithelial cells creates the main driving force of pulmonary fluid clearance. It has been demonstrated before that IAV-infection of primary human and murine alveolar epithelial cells (AECs) decreases the NKA amount on the basolateral membrane of neighboring, non-infected cells via paracrine signaling of type I IFN that leads to the degradation of the transporter[214]. In infected AECs a reduction of the expression of plasma membrane-associated NKA was not observed[214], but the transporter was found to be mislocalized to the apical cell membrane (Peteranderl et al., under submission). The regulation of NKA includes a constant translocation of the enzyme between the plasma membrane and intracellular storage vesicles[249,250,267,315]. NKA endocytosis from the basolateral membrane, regulated by PKC, ERK, Rho kinase (ROCK) and actin cytoskeleton reorganization, is one of the main mechanism of impaired function of the enzyme during acute lung injury (ALI)[250]. Activation of PKCs, ERK and ROCK, as well as a remodeling of the actin cytoskeleton during IAV entry and replication is well described[277,316-322]. Therefore, I originally suspected that IAV induces endocytosis of the basolateral NKA and by alteration of the cellular trafficking machinery, which could lead to NKA mistargeting to the apical plasma membrane. In the

present study, IAV infection of bronchial epithelial Calu3 cells also led to the activation of ERK, ROCK signaling and MLCK that regulates actin cytoskeleton reorganization. Interestingly, although IAV induced activation of these pathways that are involved in internalization of NKA (based on the literature analysis), IAV infection of primary murine and human AECs did not induce a decrease of plasma membrane-associated NKA, when its amount was analyzed by flow cytometry[214]. Flow cytometry requires a single cell suspension that is not allowing an analysis of protein redistribution from the basolateral to the apical cell membrane. Therefore, in this work basolateral NKA membrane abundance of highly polarized Calu3 cells during IAV infection was analyzed by surface protein biotinylation of polarized cell cultures. Surface protein biotinylation analysis revealed no reduction of either total NKA α_1 subunit amount or its abundance in the basolateral cell membrane in IAV-infected Calu3 cells, but its mislocalization to the apical cell membrane was clearly detected. Moreover, when inhibitors of MEK/ERK, ROCK, MLCK and actin polymerization effectors were administered, only inhibition of ROCK prevented apical localization of NKA α_1 and β_1 subunits, as shown by immunofluorescence analysis and "On Cell Western Blotting" (OCWB). Notably, this mistargeting of NKA was found not to dependent on the IAV subtype, but is generally IAV-induced.

An effect of ROCK activity on NKA membrane abundance in alveolar epithelial cells is controversially described in the literature. Stimulation of primary rat AEC and human alveolar epithelial cell line A549 with the β–adrenergic agonist isoproterenol activates RhoA/ROCK and leads to the recruitment of NKA α subunits into the plasma membrane from the intracellular compartment[258,323]. In contrast, hypoxia (1.5% O_2)-induced activation of RhoA/ROCK in A549 cells induced endocytosis of the α1 subunit of NKA from the plasma membrane[254]. The mechanism that is involved in RhoA/ROCK regulation of NKA endocytosis is presumably based on the regulation of actin cytoskeleton reorganization[254]. In the current study, inhibition of MEK/ERK and MLCK or destruction of actin fibers by cytochalasin D as well as enhancement of actin polymerization by jasplakinolide application did not prevent IAV-induced apical mistargeting of NKA in infected Calu3 cells. Thus, despite the fact that IAV infection induced an activation of signals involved in endocytosis of NKA in Calu3 cells, the amount of the basolateral membrane-associated ion transporter was not reduced during the course of infection. Nevertheless, I was able to show conclusively that virus-induced ROCK activity plays an important role in the process NKA mislocalization.

Mislocalization of the NKA to the apical cell domain was described in the retinal pigment epithelium (RPE) during cell re-morphogenesis and in kidney epithelial cells during autosomal

dominant polycystic kidney disease (ADPKD) and is correlated with increased transcription and translation of the β2 isoform of the NKA β subunit[229,230]. The β2 subunit contains five N-glycosylation sites promoting the apical membrane sorting, whereas the β1 subunit contains only basolateral membrane sorting signals[266]. The apically mislocalized pump in the RPE consists of α2 and β2 subunit dimers, whereas α_1 subunit was only presented in basolateral membrane as well as the majority of β1 subunit[229]. In ADPKD epithelium, α1 and β2 subunits were localized in the apical cell domain, whereas the β1 subunit was detected only in the basolateral membrane[230]. Nevertheless, during IAV-induced mistargeting of NKA in Calu3 cells I could detect both, α1 and β1 subunits on the apical cell membrane. Furthermore, IAV infection of primary human and murine AEC did not increase amount of β2 subunit mRNA (Peteranderl, unpublished). Since only assembled α1/β1-α1/β2 dimers are able to be exported from the endoplasmic reticulum to the Golgi apparatus and later transported to the plasma membrane, an inhibition of the ER-Golgi transport is supposed to inhibit a transport of newly synthesized α1/β2 dimers[223]. Interestingly, application of an inhibitor of ER-Golgi vesicular transport (Brefeldin A) to the IAV-infected Calu3 cells did not prevent mistargeting of NKA to the apical cell membrane, but - as expected - reduced an amount of apical membrane-associated viral proteins HA and M2 that are known be transported via the ER/Golgi pathway[324]. Therefore, it seems likely that IAV infection induces apical mislocalization of NKA via an alteration of plasma membrane protein recycling and protein trafficking, rather than via increase of β2 subunit expression. Nevertheless, further analysis of the abundance of β_2 and α_2 subunits in the apical membrane of IAV-infected Calu3 cells, as well as an investigation of IAV effects on β1/ β2 subunits glycosylation are required.

30-70% of cellular NKA is localized within the cytoplasmic vesicular storage, allowing a quick response to extracellular stimuli[267,285]. Analysis of NKA-containing vesicles motion and incorporation of the transporter into the plasma membrane demonstrated that these processes are dependent on structural and functional integrity of the microtubule cytoskeleton[257,263]. I could show that administration of the microtubule polymerization inhibitor – nocodazole, or the microtubule polymer stabilizer – paclitaxel (in non-toxic concentrations) to IAV-infected Calu3 cells indeed prevented the apical mislocalization of α1 and β1 NKA subunits at the late stage of the virus replication cycle. Previously it was described, that the movement of NKA-containing vesicles along the microtubule network in A549 cells utilizes kinesin-1 as a molecular motor, providing tubulin-dependent transport[263,325]. Notably, I could also show that application of a competitive kinesin-1 inhibitor (adenosine 5′-(β,γ-imido)triphosphate (AMP-PNP)) to IAV-infected Calu3 cells prohibited mistargeting of NKA to the apical cell membrane

at the late stage of the viral infection. The fact that inhibition of kinesin-1 did not have a negative effect on apical localization of the viral HA and M2, indicates potentially different transport mechanisms for apical membrane-associated virus proteins and NKA.

The late phase of IAV replication includes virus particle assembly and virion budding from the apical plasma membrane of infected cells. Although, a clear picture how IAV utilizes host actin filaments and microtubule networks for the transport of its own proteins and virus components is not described, an involvement of microtubules in the transport of vRNPs to the apical plasma membrane by recruitment of Rab11-recycling endosomes is well demonstrated [14,146,148,149,152,158,160-163,166,286,326]. The GTPase Rab11 is one of the major regulators of the endocytic recycling compartment and it allows actin- and microtubule-dependent vesicular transport via binding to the different effectors molecules, including molecular motors such as myosin V, kinesin-1, kinesin-2 and kinesin-3[150,151,157,159]. During IAV infection, newly synthesized vRNPs compete with Rab11-family-interacting proteins (FIPs) for the binding to Rab11, resulting on one hand in impaired sorting efficiency of recycling endosomes and on the other hand in efficient vRNP transport[148,149,286]. The cytoplasmic NKA storage vesicles include clathrin-coated vesicles, early- / late endosomes and lysosomes. Comellas et al. demonstrated in A549 cells the co-localization of the NKAα1 subunit with the Rab10 protein that is regulating a vesicular transport from the Golgi apparatus to the basolateral membrane[261]. In the present study, subcellular fragmentation of IAV-infected Calu3 cells revealed that the viral NP protein (an indicator for vRNPs[327]), cellular Rab11 and the NKAα1 subunit are distributed in the same fractions. This finding allows me to suggest that for the apical transport of its vRNPs IAV recruit Rab11-positive vesicles that also contain NKA. Transport of such vesicles might be facilitated by the microtubule molecular motor kinesin-1 that was reported to be involved in the transport of NKA-containing vesicles to the plasma membrane and interacts with Rab11. Nevertheless, so far only one molecular motor – KIF13A, that belongs to the kinesin-3 family, is described to mediate the vRNP transport[152,161,263,328].

Previously, it was shown that IAV infection increases acetylation of lysine 40 (K40) in α-tubulin of microtubules via post-translational modification to generate stable, long-lived microtubules and thereby to improve the apical vRNP and HA transport[165,299,329-331]. Hence, late in the viral replication cycle, IAV infection leads to the activation of caspase-3 that cleaves and inactivates histone deacetylase 6 (HDAC6), a cytoplasmic multifunctional enzyme, responsible for microtubules deacetylation[165,166,303]. Accordingly, depletion of HDAC6 or its inhibition by tubacin or by trichostatin A increased the virus titer in A549 cells[165,299]. In the present work, application of tubacin to IAV-infected Calu3 cells also led to elevated HA and M2 protein

abundance on the apical plasma membrane and slightly increased amounts of apically mislocalized NKA. Acetylated microtubules have been shown to promote kinasin-1 binding and transport *in vivo*[293-295]. Therefore, it seems likely, that IAV-induced elevation of microtubule acetylation (by virus-induced, caspase-dependent HDAC6-degradation) results in an increase of kinesin-1-dependent transport of NKA-containing vesicles. Nevertheless, my results show that tubacin application did not significantly affect the apical mistargeting of NKA. This might be explained by exhaustion of the NKA amount within cellular vesicular storage during IAV-infection. Therefore, NKA abundance on the apical membrane cannot be further increased by HDAC6 inhibition. In agreement with the fact that nocodazole reduces microtubule acetylation, the here observed negative effect of nocodazole administration on IAV-induced NKA mislocalization is also in line with the importance of microtubule acetylation for NKA-containing vesicles trafficking[166,299]

Husain et al. demonstrated a requirement of the RhoA GTPase for the signaling and regulation of HDAC6 activity during IAV infection of canine kidney epithelial cells (MDCK II)[299]. Knockdown of RhoA by siRNA further increased acetylation of microtubules in IAV-infected cells[299]. One of the downstream effectors of RhoA is ROCK that is involved in regulation of the HDAC6 activity via phosphorylation of its inhibitor - tubulin polymerization-promoting protein-1 (TPPP1)[332,333]. Dephosphorylated TPPP1 binds to HDAC6 and inhibits its activity, while phosphorylation of TPPP1 by ROCK impairs this binding and allows HDAC6 activity. Surprisingly, I found that inhibition of ROCK activity in IAV-infected Calu3 cells did not increase the amount of acetylated α-tubulin, but in contrast, rather a reduction of acetylated microtubules was observed at the late phase of IAV replication. This might in part be explained by the fact that ROCK inhibits activity of ERK, which is activated during IAV infection and can increase the deacetylase activity of HDAC6 by its direct phosphorylation[334-336]. This observed decrease of microtubule acetylation by ROCK-inhibition might therefore impair the NKA mislocalization.

As mentioned earlier, HDAC6 is a substrate for the proteolytic cleavage by caspase-3, which is activated during infection and is essential for efficient IAV-propagation[144,303,337]. Notably, several ROCK-activated substrates are found to be involved in the intrinsic and the extrinsic caspase activation, promoting apoptosis[306]. In IAV-infected Calu3 cells, I observed that activation of caspase-3 at the late stage of the infection was correlated with the degradation of HDAC6 and the activation of ROCK. Interestingly, the inhibition of caspase-3 did not prevent apical mistargeting of NKA. Here it should be noted that since caspase-3 can also directly activate ROCK (ROCK1)[306], inhibition of caspase-3 and as a result - a reduced activity

of ROCK, might lead to the decreased amount of TPPPP1-free active HDAC6 that increases tubulin acetylation. Therefore, caspase inhibition might not have a prominent negative effect on NKA mislocalisation. Nevertheless, further experiments to confirm this speculation are needed.

Taken together, I propose the following mechanism for the NKA mislocalization during IAV-infection At the late stage of virus replication, one of the IAV-triggered pathways leads to **(i)** activation of ROCK, that results in the **(ii)** stimulation of caspase-3, leading to **(iii)** HDAC6 degradation. Reduction of the HDAC6 amount correlates with an **(iv)** increase of microtubule acetylation that **(v)** promotes tubulin-dependent trafficking of the viral proteins and vRNPs and **(vi)** increase of motility of NKA-containing vesicles due to the high affinity of kinesin-1 molecular motor to acetylated microtubules. Presumably, for the transport of vRNPs the virus "recruits" NKA-containing vesicles, which are co-delivered to the apical cell membrane by a piggy-back mechanism.

The osmotic gradient, which is generated by NKA is important for the maintenance of the optimal volume and composition of the airway surface fluid (ASF) that consists of mucus and the periciliary liquid layer (PCL)[313]. The PCL surrounds underlying epithelial cells providing the ideal conditions for the ciliary beating that is required for the mucus clearance[338,339]. The mucus layer traps environmental pollution agents and respiratory pathogens, including IAV[63,64,313,338,339]. The efficiency of mucus clearance in the airway is determined by the rate of cilia beating and mucus hydration that strongly depends on an active ion transport[338,339]. Infringement of the Na^+ gradient disturbs the fluid homeostasis resulting either in pulmonary edema or in high-viscosity of the PCL, impairing the normal cilia beating[339]. The cell line that has been used in the present work (Calu3) is producing mucus when cultivated on permeable Transwell® cell culture inserts at liquid- or air-liquid-interfaces (LLI/ALI). Interestingly, when mispolarization of NKA during IAV-infection was prevented by an administration of nocodazole, paclitaxel or a ROCK-inhibitor to IAV-infected ALI culture of Calu3 cells, the virus titer was significantly reduced at each measured time point post infection. When nocodazole, paclitaxel or a ROCK-inhibitor was applied to the Calu3 cells cultivated submerged in tissue plates the virus yield was not affected. Interestingly, under these conditions the mucus layer above the Calu3 cells was not detectable This indicates that a strong hydration of the mucus due to the culture medium results in a low mucosal viscosity. Taken together, these results could suggest that the apical mistargeting of NKA leads to a more efficient IAV spread by reduced viscosity of the muscus produced from the infected cells. Down-regulation

of the Na^+ transport allows accumulation of fluids on the apical side that increases hydration of the mucus and could therefore provide easier virus spread.

Previously it was demonstrated that an increase of the Na^+ transport by up-regulation of NKA amount enhances alveolar fluid clearance during ALI[214,236,260]. The preclusion of the IAV-induced apical NKA mistargeting by ROCK inhibition restored IAV-compromised vectorial water transport through the highly polarized monolayer of infected Calu3 cells and reduced lung edema formation in IAV-infected mice. The positive effect of ROCK inhibition on the vectorial water transport and edema resolution during IAV-infection might also be explained by the increased NKA activity. Arce et al. summarized data on the NKA activity inhibition by its interaction with submembraneous acetylated tubulin[340]. The reviewed data allows to speculate that inhibition of ROCK during IAV-infection that results in a decreased level of acetylated tubulin might lead to the dissociation of NKA from tubulin and by this stimulates its activity. Further experiments that could support this speculation are therefore needed.

A clinical application of ROCK inhibitors is currently only approved in Japan and China for the treatment of cerebral vasospasm and glaucoma[341]. Nevertheless, due to the broad spectrum of downstream-regulated molecules, ROCK-inhibitors might have a potential benefit during the treatment of different pathological conditions such as cancer, kidney failure, osteoporosis and neuronal degeneration[342-350]. Several publications demonstrated a protective effect of ROCK inhibition during indirect acute lung injury (iALI) induced either by sepsis or by chemical agent[351-355]. The application of ROCK-inhibitors was associated with the improvement of endothelial permeability, reduction of lung inflammation, cell infiltration and pulmonary alveolar flooding[351-355]. The mechanism of action was considered as the maintenance of the barrier function of the pulmonary microvascular endothelial cells by inhibition of actin-dependent cell contraction induced by active ROCK and decrease of cell death by inhibition of caspase-3 activity[351-355].

In the murine model of the current study, ALI was induced by direct impact of IAV on alveolar epithelial cells. Administration of a ROCK-inhibitor at low concentration resulted in the reduction of IAV-induced pulmonary edema evaluated as wet/dry lung weight ratio. IAV titer declined more rapidly in the murine lungs when a ROCK-inhibitor was administered to the animals. Histopathologic analysis of lungs from the IAV-infected group compared to the IAV-infected, and ROCK-inhibitor treated group also revealed a difference in the amounts of infiltrated inflammatory cells and damage of the lung tissue. It might be possible that a more efficient virus spread in the lungs due to the apical NKA translocation (see above), could induced more acute damage of the alveolar epithelial cells and result in an intensified release

of inflammatory mediators. This again might lead to an increased damage of the pulmonary architecture. The animal group treated with a ROCK-inhibitor after IAV-infection demonstrated lower levels of alveolar tissue infiltration and damage. Nevertheless, to better understand the influence of ROCK-inhibition on the immune response during IAV-infection additionally experiments are needed.

Taking together, this work presented here demonstrates a novel mechanism of IAV-induced pathogenesis affecting the NKA membrane localization that leads to an imbalance of the pulmonary fluid homeostasis. Targeting of this pathway with ROCK-kinase inhibitors might be a therapeutic strategy to maintain normal fluid regulation and to reduce IAV-induced pathological conditions in patients with ARDS.

5. Summary

One of the fatal complication of influenza A virus (IAV) infection is the acute respiratory distress syndrome (ARDS) associated with sever formation of alveolar edema. Impaired resolution of pulmonary edema is a result of a direct destruction of the alveolar epithelium induced by IAV replication and an infringement of the osmotic gradient in the alveolar microenvironment, which is the main driving force of alveolar fluid clearance. IAV infection down-regulates the amount and function of several membrane ion-channels and pumps that are needed to establish the osmotic gradient.

In the present work a novel mechanism of IAV pathogenicity affecting the basolateral membrane-located Na^+,K^+-ATPase (NKA), the major regulator of fluid homeostasis, is described. IAV infection did not reduce the overall amount of membrane-associated NKA, but induced a mislocalization of the enzyme to the apical site of infected polarized human bronchial epithelial cells (Calu3), as well as canine kidney epithelial cells (MDCK II). The mislocalization of NKA was not dependent on the IAV subtype or viral replication efficiency, but seems to be induced by IAV in general. The results of the present work indicate that the source of apically localized NKA is the vesicular intracellular NKA depot, since no decrease of NKA in the basolateral cell membrane was observed during IAV-infection, as well as inhibition of newly synthesized NKA maturation did not prevent its apical distribution. Application of the actin polymerization inhibitor cytochalasin D, the actin polymerization enhancer jasplakinolide, the inhibitor of microtubule polymerization nocodazole or the stabilizer of microtubule polymer paclitaxel, indicated that NKA mistargeting to the apical cell membrane depends on the integrity of the tubulin network. Moreover, a post-translational modification of α-tubulin (acetylation of residue K40), is needed for IAV-induced NKA mistargeting. This modification seems to be is indirectly regulated by Rho-kinase (ROCK) as NKA mislocalization in IAV-infected cells can be prevented by ROCK inhibition, which impairs IAV-induced caspase-3-dependent degradation of histone deacetylase 6 (HDAC6), resulting in a reduced amount of acetylated α-tubulin needed for apical NKA transport. In addition, ROCK inhibition not only prevented mistargeting of NKA to the apical membrane, but also reduced virus titer and restored vectorial water transport through the monolayer of highly polarized infected Calu3 cells. Application of Fasudil HCl to IAV-infected mice improved pulmonary edema clearance and reduced the virus titer and immune cell infiltration in the lungs. Taking together, an administration of ROCK inhibitors might be a potential treatment scenario for the patients with IAV-induced ARDS

6. Zusammenfassung

Eine der gefürchtetsten Komplikationen bei einer Influenza-A-Virus (IAV)-Infektion ist die Entwicklung eines „Akuten Atemnotsyndroms“ (ARDS), welches durch ein schweres alveoläres Ödem bedingt ist. Die Störung in der Auflösung des pulmonaren Ödems liegt zum einem in der direkten Zerstörung der Alveolarepithelzellen, bedingt durch die IAV-Replikation, und zum anderen in der Veränderung der alveolaren Mikro-Umgebung und damit in einer Störung des osmotischen Gradienten, einer der wichtigsten Faktoren zur Ödembeseitigung. Im Rahmen einer IAV-Infektion kommt es zu einer funktionellen als auch quantitativen Modulation verschiedener membranständiger Ionenkanäle bzw. –pumpen, welche zur Aufrechterhaltung des osmotischen Gradient benötigt werden.

In der hier vorgestellten Arbeit wird ein neuer Mechanismus der IAV-Pathogenität beschrieben, welcher die Lokalisation, der in der basolateralen Membran verankerten Natrium/Kalium-ATPase (NKA), dem Hauptregulator der Flüssigkeitshomöostase, beeinflusst. IAV-Infektion humaner Bronchialepithelzellen (Calu3) oder Hunde-Nierenepithelzellen (MDCK II) führte nicht zu einer Veränderung in der Gesamtmenge der membranständigen NKA, löste aber eine NKA-Fehllokalisation in den apikalen Membranbereich aus. Die Fehllokalisation war dabei weder vom IAV-Subtyp noch von der Effizienz der viralen Replikation abhängig, sondern scheint generell von IAV ausgelöst zu werden. Die Ergebnisse der Arbeit zeigen, dass vermutlich intrazelluläre Vesikel die Quelle der apikalen NKA darstellen, da es zu keiner Abnahme der NKA-Menge in der basolateralen Membran im Sinne einer Translokalisation kam und auch die Hemmung der NKA-Neusynthese die NKA-Fehllokalisation nicht verhinderte. Allerdings konnte durch die Hemmung der Polymerisation (Nocodazol) oder der Stabilisierung (Paclitaxel) der Mikrotubuli die apikale Fehllokalisation der NKA vermindert werden. Zudem konnte nachgewiesen werden, dass eine posttranslationale Acetylierung von α-Tubulin ebenfalls für die Fehllokalisation notwendig ist. Diese Modifikation scheint indirekt durch die Rho-Kinase (ROCK) reguliert zu werden, da eine ROCK-Hemmung (Fasudil-HCl) die NKA-Fehllokalisation vermindert. Die ROCK-Hemmung führt zu einer Reduktion der IAV-induzierten, Caspase-3-abhängigen Degradierung der Histon-Deacetylase 6 (HDAC6). Dies wiederum führt zu einer verminderten Menge an acetyliertem Tubulin. Durch eine Hemmung von ROCK konnte aber nicht nur die NKA-Fehllokalisation in die apikale Membran reduziert werden, sondern auch der Virustiter. Gleichzeitig wurde der

vektoriale Wassertransport durch hochpolarisierte, IAV-infizierte Calu-3-Zellen wiederhergestellt. Im Mausmodell führte die Behandlung mit Fasudil-HCl zu einer verbesserten Resorption des pulmonalen Ödems, einem verminderten Virustiter und zu einer Abnahme der Immunzellinfiltration der Lunge. Zusammenfassend könnte die Hemmung von ROCK eine mögliche Therapieoption für ein IAV-induziertes ARDS darstellen.

7. References

1 Lefkowitz, E. J. *et al.* Virus taxonomy: the database of the International Committee on Taxonomy of Viruses (ICTV). *Nucleic acids research* **46**, D708-D717, doi:10.1093/nar/gkx932 (2018).

2 Lamb, R. A. in *Encyclopedia of Virology* Vol. 3rd Edition (ed B. W.J. Mahy, Van Regenmortel, M.H.V.) Ch. Influenza, 95-103 (Elsevier, 2008).

3 Ma, W., Garcia-Sastre, A. & Schwemmle, M. Expected and Unexpected Features of the Newly Discovered Bat Influenza A-like Viruses. *PLoS pathogens* **11**, e1004819, doi:10.1371/journal.ppat.1004819 (2015).

4 Tong, S. *et al.* A distinct lineage of influenza A virus from bats. *Proceedings of the National Academy of Sciences of the United States of America* **109**, 4269-4274, doi:10.1073/pnas.1116200109 (2012).

5 Tong, S. *et al.* New world bats harbor diverse influenza A viruses. *PLoS pathogens* **9**, e1003657, doi:10.1371/journal.ppat.1003657 (2013).

6 Shaw, M. L., Palese, P. in *Encyclopedia of Virology* (ed B. W.J. Mahy, Van Regenmortel, M.H.V.) (Elsevier, 2008).

7 Badham, M. D. & Rossman, J. S. Filamentous Influenza Viruses. *Current clinical microbiology reports* **3**, 155-161, doi:10.1007/s40588-016-0041-7 (2016).

8 Dadonaite, B., Vijayakrishnan, S., Fodor, E., Bhella, D. & Hutchinson, E. C. Filamentous influenza viruses. *The Journal of general virology* **97**, 1755-1764, doi:10.1099/jgv.0.000535 (2016).

9 Noda, T. Native morphology of influenza virions. *Frontiers in microbiology* **2**, 269, doi:10.3389/fmicb.2011.00269 (2011).

10 Edinger, T. O., Pohl, M. O. & Stertz, S. Entry of influenza A virus: host factors and antiviral targets. *The Journal of general virology* **95**, 263-277, doi:10.1099/vir.0.059477-0 (2014).

11 Rossman, J. S. & Lamb, R. A. Influenza virus assembly and budding. *Virology* **411**, 229-236, doi:10.1016/j.virol.2010.12.003 (2011).

12 Shtykova, E. V. *et al.* Influenza virus Matrix Protein M1 preserves its conformation with pH, changing multimerization state at the priming stage due to electrostatics. *Scientific reports* **7**, 16793, doi:10.1038/s41598-017-16986-y (2017).

13 Hutchinson, E. C. *et al.* Erratum: Conserved and host-specific features of influenza virion architecture. *Nature communications* **6**, 6446, doi:10.1038/ncomms7446 (2015).

14 Hutchinson, E. C. & Fodor, E. Transport of the influenza virus genome from nucleus to nucleus. *Viruses* **5**, 2424-2446, doi:10.3390/v5102424 (2013).

15 Portela, A. & Digard, P. The influenza virus nucleoprotein: a multifunctional RNA-binding protein pivotal to virus replication. *The Journal of general virology* **83**, 723-734, doi:10.1099/0022-1317-83-4-723 (2002).

16 Ye, Q., Krug, R. M. & Tao, Y. J. The mechanism by which influenza A virus nucleoprotein forms oligomers and binds RNA. *Nature* **444**, 1078-1082, doi:10.1038/nature05379 (2006).

17 Hsu, M. T., Parvin, J. D., Gupta, S., Krystal, M. & Palese, P. Genomic RNAs of influenza viruses are held in a circular conformation in virions and in infected cells by a terminal panhandle. *Proceedings of the National Academy of Sciences of the United States of America* **84**, 8140-8144 (1987).

18 Lee, N. *et al.* Genome-wide analysis of influenza viral RNA and nucleoprotein association. *Nucleic acids research* **45**, 8968-8977, doi:10.1093/nar/gkx584 (2017).

19 Te Velthuis, A. J. & Fodor, E. Influenza virus RNA polymerase: insights into the mechanisms of viral RNA synthesis. *Nature reviews. Microbiology* **14**, 479-493, doi:10.1038/nrmicro.2016.87 (2016).

20 Guilligay, D. *et al.* The structural basis for cap binding by influenza virus polymerase subunit PB2. *Nature structural & molecular biology* **15**, 500-506, doi:10.1038/nsmb.1421 (2008).

21 Fodor, E. *et al.* A single amino acid mutation in the PA subunit of the influenza virus RNA polymerase inhibits endonucleolytic cleavage of capped RNAs. *Journal of virology* **76**, 8989-9001 (2002).

22 Lee, M. T. *et al.* Definition of the minimal viral components required for the initiation of unprimed RNA synthesis by influenza virus RNA polymerase. *Nucleic acids research* **30**, 429-438 (2002).

23 Maier, H. J., Kashiwagi, T., Hara, K. & Brownlee, G. G. Differential role of the influenza A virus polymerase PA subunit for vRNA and cRNA promoter binding. *Virology* **370**, 194-204, doi:10.1016/j.virol.2007.08.029 (2008).

24 Jung, T. E. & Brownlee, G. G. A new promoter-binding site in the PB1 subunit of the influenza A virus polymerase. *The Journal of general virology* **87**, 679-688, doi:10.1099/vir.0.81453-0 (2006).

25 Kobayashi, M., Toyoda, T. & Ishihama, A. Influenza virus PB1 protein is the minimal and essential subunit of RNA polymerase. *Archives of virology* **141**, 525-539 (1996).

26 Chen, W. *et al.* A novel influenza A virus mitochondrial protein that induces cell death. *Nature medicine* **7**, 1306-1312, doi:10.1038/nm1201-1306 (2001).

27 Wise, H. M. *et al.* Overlapping signals for translational regulation and packaging of influenza A virus segment 2. *Nucleic acids research* **39**, 7775-7790, doi:10.1093/nar/gkr487 (2011).

28 Wise, H. M. *et al.* A complicated message: Identification of a novel PB1-related protein translated from influenza A virus segment 2 mRNA. *Journal of virology* **83**, 8021-8031, doi:10.1128/JVI.00826-09 (2009).

29 Yamayoshi, S., Watanabe, M., Goto, H. & Kawaoka, Y. Identification of a Novel Viral Protein Expressed from the PB2 Segment of Influenza A Virus. *Journal of virology* **90**, 444-456, doi:10.1128/JVI.02175-15 (2016).

30 Long, J. C. & Fodor, E. The PB2 Subunit of the Influenza A Virus RNA Polymerase Is Imported into the Mitochondrial Matrix. *Journal of virology* **90**, 8729-8738, doi:10.1128/JVI.01384-16 (2016).

31 Chakrabarti, A. K. & Pasricha, G. An insight into the PB1F2 protein and its multifunctional role in enhancing the pathogenicity of the influenza A viruses. *Virology* **440**, 97-104, doi:10.1016/j.virol.2013.02.025 (2013).

32 Buehler, J. *et al.* Influenza A virus PB1-F2 protein expression is regulated in a strain-specific manner by sequences located downstream of the PB1-F2 initiation codon. *Journal of virology* **87**, 10687-10699, doi:10.1128/JVI.01520-13 (2013).

33 Le Goffic, R. *et al.* Influenza A virus protein PB1-F2 exacerbates IFN-beta expression of human respiratory epithelial cells. *Journal of immunology* **185**, 4812-4823, doi:10.4049/jimmunol.0903952 (2010).

34 Mazur, I. *et al.* The proapoptotic influenza A virus protein PB1-F2 regulates viral polymerase activity by interaction with the PB1 protein. *Cellular microbiology* **10**, 1140-1152, doi:10.1111/j.1462-5822.2008.01116.x (2008).

35 Tauber, S., Ligertwood, Y., Quigg-Nicol, M., Dutia, B. M. & Elliott, R. M. Behaviour of influenza A viruses differentially expressing segment 2 gene products in vitro and in vivo. *The Journal of general virology* **93**, 840-849, doi:10.1099/vir.0.039966-0 (2012).

36 Jagger, B. W. *et al.* An overlapping protein-coding region in influenza A virus segment 3 modulates the host response. *Science* **337**, 199-204, doi:10.1126/science.1222213 (2012).

37 Shi, M. *et al.* Evolutionary conservation of the PA-X open reading frame in segment 3 of influenza A virus. *Journal of virology* **86**, 12411-12413, doi:10.1128/JVI.01677-12 (2012).

38 Bavagnoli, L. *et al.* The novel influenza A virus protein PA-X and its naturally deleted variant show different enzymatic properties in comparison to the viral endonuclease PA. *Nucleic acids research* **43**, 9405-9417, doi:10.1093/nar/gkv926 (2015).

39 Hayashi, T., MacDonald, L. A. & Takimoto, T. Influenza A Virus Protein PA-X Contributes to Viral Growth and Suppression of the Host Antiviral and Immune Responses. *Journal of virology* **89**, 6442-6452, doi:10.1128/JVI.00319-15 (2015).

40 Gong, Y. N., Chen, G. W., Chen, C. J., Kuo, R. L. & Shih, S. R. Computational analysis and mapping of novel open reading frames in influenza A viruses. *PloS one* **9**, e115016, doi:10.1371/journal.pone.0115016 (2014).

41 Muramoto, Y., Noda, T., Kawakami, E., Akkina, R. & Kawaoka, Y. Identification of novel influenza A virus proteins translated from PA mRNA. *Journal of virology* **87**, 2455-2462, doi:10.1128/JVI.02656-12 (2013).

42 Wang, Q. *et al.* Host Interaction Analysis of PA-N155 and PA-N182 in Chicken Cells Reveals an Essential Role of UBA52 for Replication of H5N1 Avian Influenza Virus. *Frontiers in microbiology* **9**, 936, doi:10.3389/fmicb.2018.00936 (2018).

43 Russell, C. J., Hu, M. & Okda, F. A. Influenza Hemagglutinin Protein Stability, Activation, and Pandemic Risk. *Trends in microbiology* **26**, 841-853, doi:10.1016/j.tim.2018.03.005 (2018).

44 Steinhauer, D. A. Role of hemagglutinin cleavage for the pathogenicity of influenza virus. *Virology* **258**, 1-20, doi:10.1006/viro.1999.9716 (1999).

45 Wilson, I. A., Skehel, J. J. & Wiley, D. C. Structure of the haemagglutinin membrane glycoprotein of influenza virus at 3 A resolution. *Nature* **289**, 366-373 (1981).

46 Ciminski, K., Thamamongood, T., Zimmer, G. & Schwemmle, M. Novel insights into bat influenza A viruses. *The Journal of general virology* **98**, 2393-2400, doi:10.1099/jgv.0.000927 (2017).

47 Karakus, U. *et al.* MHC class II proteins mediate cross-species entry of bat influenza viruses. *Nature* **567**, 109-112, doi:10.1038/s41586-019-0955-3 (2019).

48 Garten, W., Bosch, F. X., Linder, D., Rott, R. & Klenk, H. D. Proteolytic activation of the influenza virus hemagglutinin: The structure of the cleavage site and the enzymes involved in cleavage. *Virology* **115**, 361-374 (1981).

49 Kido, H. *et al.* Host envelope glycoprotein processing proteases are indispensable for entry into human cells by seasonal and highly pathogenic avian influenza viruses. *Journal of molecular and genetic medicine : an international journal of biomedical research* **3**, 167-175 (2008).

50 Sakai, K. *et al.* TMPRSS2 Independency for Haemagglutinin Cleavage In Vivo Differentiates Influenza B Virus from Influenza A Virus. *Scientific reports* **6**, 29430, doi:10.1038/srep29430 (2016).

51 Kido, H., Murakami, M., Oba, K., Chen, Y. & Towatari, T. Cellular proteinases trigger the infectivity of the influenza A and Sendai viruses. *Molecules and cells* **9**, 235-244 (1999).

52 Klenk, H. D. & Garten, W. Host cell proteases controlling virus pathogenicity. *Trends in microbiology* **2**, 39-43 (1994).

53 Russell, C. J. in *Encyclopedia of Virology* Vol. 3rd Edition (ed B. W.J. Mahy, Van Regenmortel, M.H.V.) 489-494 (Elsevier, 2008).

54 Varki, A. & Schauer, R. in *Essentials of Glycobiology* (eds nd *et al.*) (2009).

55 Ito, T. *et al.* Molecular basis for the generation in pigs of influenza A viruses with pandemic potential. *Journal of virology* **72**, 7367-7373 (1998).

56 Suzuki, Y. Sialobiology of influenza: molecular mechanism of host range variation of influenza viruses. *Biological & pharmaceutical bulletin* **28**, 399-408 (2005).

57 Couceiro, J. N., Paulson, J. C. & Baum, L. G. Influenza virus strains selectively recognize sialyloligosaccharides on human respiratory epithelium; the role of the host cell in selection of hemagglutinin receptor specificity. *Virus research* **29**, 155-165 (1993).

58 Rogers, G. N., Pritchett, T. J., Lane, J. L. & Paulson, J. C. Differential sensitivity of human, avian, and equine influenza A viruses to a glycoprotein inhibitor of infection: selection of receptor specific variants. *Virology* **131**, 394-408 (1983).

59 Gaymard, A., Le Briand, N., Frobert, E., Lina, B. & Escuret, V. Functional balance between neuraminidase and haemagglutinin in influenza viruses. *Clinical microbiology and infection : the official publication of the European Society of Clinical Microbiology and Infectious Diseases* **22**, 975-983, doi:10.1016/j.cmi.2016.07.007 (2016).

60 Itamura, S. [Structure and function of influenza virus neuraminidase]. *Nihon rinsho. Japanese journal of clinical medicine* **55**, 2570-2574 (1997).

61 Shtyrya, Y. A., Mochalova, L. V. & Bovin, N. V. Influenza virus neuraminidase: structure and function. *Acta naturae* **1**, 26-32 (2009).

62 Air, G. M. Influenza neuraminidase. *Influenza and other respiratory viruses* **6**, 245-256, doi:10.1111/j.1750-2659.2011.00304.x (2012).

63 Byrd-Leotis, L., Cummings, R. D. & Steinhauer, D. A. The Interplay between the Host Receptor and Influenza Virus Hemagglutinin and Neuraminidase. *International journal of molecular sciences* **18**, doi:10.3390/ijms18071541 (2017).

64 Matrosovich, M. N., Matrosovich, T. Y., Gray, T., Roberts, N. A. & Klenk, H. D. Neuraminidase is important for the initiation of influenza virus infection in human airway

epithelium. *Journal of virology* **78**, 12665-12667, doi:10.1128/JVI.78.22.12665-12667.2004 (2004).

65 Ohuchi, M., Feldmann, A., Ohuchi, R. & Klenk, H. D. Neuraminidase is essential for fowl plague virus hemagglutinin to show hemagglutinating activity. *Virology* **212**, 77-83, doi:10.1006/viro.1995.1455 (1995).

66 Wagner, R., Wolff, T., Herwig, A., Pleschka, S. & Klenk, H. D. Interdependence of hemagglutinin glycosylation and neuraminidase as regulators of influenza virus growth: a study by reverse genetics. *Journal of virology* **74**, 6316-6323 (2000).

67 Lamb, R. A., Lai, C. J. & Choppin, P. W. Sequences of mRNAs derived from genome RNA segment 7 of influenza virus: colinear and interrupted mRNAs code for overlapping proteins. *Proceedings of the National Academy of Sciences of the United States of America* **78**, 4170-4174 (1981).

68 Robb, N. C. & Fodor, E. The accumulation of influenza A virus segment 7 spliced mRNAs is regulated by the NS1 protein. *The Journal of general virology* **93**, 113-118, doi:10.1099/vir.0.035485-0 (2012).

69 Shih, S. R., Suen, P. C., Chen, Y. S. & Chang, S. C. A novel spliced transcript of influenza A/WSN/33 virus. *Virus genes* **17**, 179-183 (1998).

70 Harris, A., Forouhar, F., Qiu, S., Sha, B. & Luo, M. The crystal structure of the influenza matrix protein M1 at neutral pH: M1-M1 protein interfaces can rotate in the oligomeric structures of M1. *Virology* **289**, 34-44, doi:10.1006/viro.2001.1119 (2001).

71 Ruigrok, R. W. *et al.* Membrane interaction of influenza virus M1 protein. *Virology* **267**, 289-298, doi:10.1006/viro.1999.0134 (2000).

72 Shtykova, E. V. *et al.* Structural analysis of influenza A virus matrix protein M1 and its self-assemblies at low pH. *PloS one* **8**, e82431, doi:10.1371/journal.pone.0082431 (2013).

73 Bui, M., Whittaker, G. & Helenius, A. Effect of M1 protein and low pH on nuclear transport of influenza virus ribonucleoproteins. *Journal of virology* **70**, 8391-8401 (1996).

74 Bui, M., Wills, E. G., Helenius, A. & Whittaker, G. R. Role of the influenza virus M1 protein in nuclear export of viral ribonucleoproteins. *Journal of virology* **74**, 1781-1786 (2000).

75 Manzoor, R., Igarashi, M. & Takada, A. Influenza A Virus M2 Protein: Roles from Ingress to Egress. *International journal of molecular sciences* **18**, doi:10.3390/ijms18122649 (2017).

76 Pielak, R. M. & Chou, J. J. Influenza M2 proton channels. *Biochimica et biophysica acta* **1808**, 522-529, doi:10.1016/j.bbamem.2010.04.015 (2011).

77 Cady, S. D., Luo, W., Hu, F. & Hong, M. Structure and function of the influenza A M2 proton channel. *Biochemistry* **48**, 7356-7364, doi:10.1021/bi9008837 (2009).

78 Henkel, J. R., Popovich, J. L., Gibson, G. A., Watkins, S. C. & Weisz, O. A. Selective perturbation of early endosome and/or trans-Golgi network pH but not lysosome pH by dose-dependent expression of influenza M2 protein. *The Journal of biological chemistry* **274**, 9854-9860 (1999).

79 Martyna, A. *et al.* Membrane remodeling by the M2 amphipathic helix drives influenza virus membrane scission. *Scientific reports* **7**, 44695, doi:10.1038/srep44695 (2017).

80 Rossman, J. S., Jing, X., Leser, G. P. & Lamb, R. A. Influenza virus M2 protein mediates ESCRT-independent membrane scission. *Cell* **142**, 902-913, doi:10.1016/j.cell.2010.08.029 (2010).

81 Schmidt, N. W., Mishra, A., Wang, J., DeGrado, W. F. & Wong, G. C. Influenza virus A M2 protein generates negative Gaussian membrane curvature necessary for budding and scission. *Journal of the American Chemical Society* **135**, 13710-13719, doi:10.1021/ja400146z (2013).

82 Jackson, D. & Lamb, R. A. The influenza A virus spliced messenger RNA M mRNA3 is not required for viral replication in tissue culture. *The Journal of general virology* **89**, 3097-3101, doi:10.1099/vir.0.2008/004739-0 (2008).

83 Hutchinson, E. C., Curran, M. D., Read, E. K., Gog, J. R. & Digard, P. Mutational analysis of cis-acting RNA signals in segment 7 of influenza A virus. *Journal of virology* **82**, 11869-11879, doi:10.1128/JVI.01634-08 (2008).

84 Wise, H. M. *et al.* Identification of a novel splice variant form of the influenza A virus M2 ion channel with an antigenically distinct ectodomain. *PLoS pathogens* **8**, e1002998, doi:10.1371/journal.ppat.1002998 (2012).

85 Hale, B. G., Randall, R. E., Ortin, J. & Jackson, D. The multifunctional NS1 protein of influenza A viruses. *The Journal of general virology* **89**, 2359-2376, doi:10.1099/vir.0.2008/004606-0 (2008).

86 Inglis, S. C., Barrett, T., Brown, C. M. & Almond, J. W. The smallest genome RNA segment of influenza virus contains two genes that may overlap. *Proceedings of the National Academy of Sciences of the United States of America* **76**, 3790-3794 (1979).

87 Lamb, R. A. & Choppin, P. W. Segment 8 of the influenza virus genome is unique in coding for two polypeptides. *Proceedings of the National Academy of Sciences of the United States of America* **76**, 4908-4912 (1979).

88 Garaigorta, U. & Ortin, J. Mutation analysis of a recombinant NS replicon shows that influenza virus NS1 protein blocks the splicing and nucleo-cytoplasmic transport of its own viral mRNA. *Nucleic acids research* **35**, 4573-4582, doi:10.1093/nar/gkm230 (2007).

89 Plotch, S. J. & Krug, R. M. In vitro splicing of influenza viral NS1 mRNA and NS1-beta-globin chimeras: possible mechanisms for the control of viral mRNA splicing. *Proceedings of the National Academy of Sciences of the United States of America* **83**, 5444-5448 (1986).

90 Zheng, M. *et al.* An A14U Substitution in the 3' Noncoding Region of the M Segment of Viral RNA Supports Replication of Influenza Virus with an NS1 Deletion by Modulating Alternative Splicing of M Segment mRNAs. *Journal of virology* **89**, 10273-10285, doi:10.1128/JVI.00919-15 (2015).

91 O'Neill, R. E., Talon, J. & Palese, P. The influenza virus NEP (NS2 protein) mediates the nuclear export of viral ribonucleoproteins. *The EMBO journal* **17**, 288-296, doi:10.1093/emboj/17.1.288 (1998).

92 Paterson, D. & Fodor, E. Emerging roles for the influenza A virus nuclear export protein (NEP). *PLoS pathogens* **8**, e1003019, doi:10.1371/journal.ppat.1003019 (2012).

93 Robb, N. C., Smith, M., Vreede, F. T. & Fodor, E. NS2/NEP protein regulates transcription and replication of the influenza virus RNA genome. *The Journal of general virology* **90**, 1398-1407, doi:10.1099/vir.0.009639-0 (2009).

94 Selman, M., Dankar, S. K., Forbes, N. E., Jia, J. J. & Brown, E. G. Adaptive mutation in influenza A virus non-structural gene is linked to host switching and induces a novel protein by alternative splicing. *Emerging microbes & infections* **1**, e42, doi:10.1038/emi.2012.38 (2012).

95 Sauter, N. K. *et al.* Hemagglutinins from two influenza virus variants bind to sialic acid derivatives with millimolar dissociation constants: a 500-MHz proton nuclear magnetic resonance study. *Biochemistry* **28**, 8388-8396 (1989).

96 Patterson, S., Oxford, J. S. & Dourmashkin, R. R. Studies on the mechanism of influenza virus entry into cells. *The Journal of general virology* **43**, 223-229, doi:10.1099/0022-1317-43-1-223 (1979).

97 Rust, M. J., Lakadamyali, M., Zhang, F. & Zhuang, X. Assembly of endocytic machinery around individual influenza viruses during viral entry. *Nature structural & molecular biology* **11**, 567-573, doi:10.1038/nsmb769 (2004).

98 Sun, E. Z. *et al.* Real-Time Dissection of Distinct Dynamin-Dependent Endocytic Routes of Influenza A Virus by Quantum Dot-Based Single-Virus Tracking. *ACS nano* **11**, 4395-4406, doi:10.1021/acsnano.6b07853 (2017).

99 Yoshimura, A. *et al.* Infectious cell entry mechanism of influenza virus. *Journal of virology* **43**, 284-293 (1982).

100 Arcangeletti, M. C. *et al.* Host-cell-dependent role of actin cytoskeleton during the replication of a human strain of influenza A virus. *Archives of virology* **153**, 1209-1221, doi:10.1007/s00705-008-0103-0 (2008).

101 Brass, A. L. *et al.* The IFITM proteins mediate cellular resistance to influenza A H1N1 virus, West Nile virus, and dengue virus. *Cell* **139**, 1243-1254, doi:10.1016/j.cell.2009.12.017 (2009).

102 Elbahesh, H. *et al.* Novel roles of focal adhesion kinase in cytoplasmic entry and replication of influenza A viruses. *Journal of virology* **88**, 6714-6728, doi:10.1128/JVI.00530-14 (2014).

103 Sieczkarski, S. B. & Whittaker, G. R. Differential requirements of Rab5 and Rab7 for endocytosis of influenza and other enveloped viruses. *Traffic* **4**, 333-343 (2003).

104 Sun, X. & Whittaker, G. R. Role of the actin cytoskeleton during influenza virus internalization into polarized epithelial cells. *Cellular microbiology* **9**, 1672-1682, doi:10.1111/j.1462-5822.2007.00900.x (2007).

105 De Conto, F. *et al.* Highly dynamic microtubules improve the effectiveness of early stages of human influenza A/NWS/33 virus infection in LLC-MK2 cells. *PloS one* **7**, e41207, doi:10.1371/journal.pone.0041207 (2012).

106 Tsurudome, M. *et al.* Lipid interactions of the hemagglutinin HA2 NH2-terminal segment during influenza virus-induced membrane fusion. *The Journal of biological chemistry* **267**, 20225-20232 (1992).

107 Durrer, P. *et al.* H+-induced membrane insertion of influenza virus hemagglutinin involves the HA2 amino-terminal fusion peptide but not the coiled coil region. *The Journal of biological chemistry* **271**, 13417-13421 (1996).

108 Chen, J., Skehel, J. J. & Wiley, D. C. N- and C-terminal residues combine in the fusion-pH influenza hemagglutinin HA(2) subunit to form an N cap that terminates the triple-stranded coiled coil. *Proceedings of the National Academy of Sciences of the United States of America* **96**, 8967-8972 (1999).

109 Skehel, J. J. & Wiley, D. C. Receptor binding and membrane fusion in virus entry: the influenza hemagglutinin. *Annual review of biochemistry* **69**, 531-569, doi:10.1146/annurev.biochem.69.1.531 (2000).

110 Zhirnov, O. P. [The effect of pH on in vitro deproteinization in orthomyxo- and paramyxoviruses]. *Molekuliarnaia genetika, mikrobiologiia i virusologiia*, 11-15 (1990).

111 Zhirnov, O. P. Solubilization of matrix protein M1/M from virions occurs at different pH for orthomyxo- and paramyxoviruses. *Virology* **176**, 274-279 (1990).

112 Wharton, S. A., Belshe, R. B., Skehel, J. J. & Hay, A. J. Role of virion M2 protein in influenza virus uncoating: specific reduction in the rate of membrane fusion between virus and liposomes by amantadine. *The Journal of general virology* **75 (Pt 4)**, 945-948, doi:10.1099/0022-1317-75-4-945 (1994).

113 Fontana, J., Cardone, G., Heymann, J. B., Winkler, D. C. & Steven, A. C. Structural changes in Influenza virus at low pH characterized by cryo-electron tomography. *Journal of virology* **86**, 2919-2929, doi:10.1128/JVI.06698-11 (2012).

114 Hutchinson, E. C. & Fodor, E. Nuclear import of the influenza A virus transcriptional machinery. *Vaccine* **30**, 7353-7358, doi:10.1016/j.vaccine.2012.04.085 (2012).

115 Cros, J. F. & Palese, P. Trafficking of viral genomic RNA into and out of the nucleus: influenza, Thogoto and Borna disease viruses. *Virus research* **95**, 3-12 (2003).

116 Melen, K. *et al.* Importin alpha nuclear localization signal binding sites for STAT1, STAT2, and influenza A virus nucleoprotein. *The Journal of biological chemistry* **278**, 28193-28200, doi:10.1074/jbc.M303571200 (2003).

117 O'Neill, R. E., Jaskunas, R., Blobel, G., Palese, P. & Moroianu, J. Nuclear import of influenza virus RNA can be mediated by viral nucleoprotein and transport factors required for protein import. *The Journal of biological chemistry* **270**, 22701-22704 (1995).

118 Wang, P., Palese, P. & O'Neill, R. E. The NPI-1/NPI-3 (karyopherin alpha) binding site on the influenza a virus nucleoprotein NP is a nonconventional nuclear localization signal. *Journal of virology* **71**, 1850-1856 (1997).

119 Plotch, S. J., Bouloy, M., Ulmanen, I. & Krug, R. M. A unique cap(m7GpppXm)-dependent influenza virion endonuclease cleaves capped RNAs to generate the primers that initiate viral RNA transcription. *Cell* **23**, 847-858 (1981).

120 Yuan, P. *et al.* Crystal structure of an avian influenza polymerase PA(N) reveals an endonuclease active site. *Nature* **458**, 909-913, doi:10.1038/nature07720 (2009).

121 Dias, A. *et al.* The cap-snatching endonuclease of influenza virus polymerase resides in the PA subunit. *Nature* **458**, 914-918, doi:10.1038/nature07745 (2009).

122 Reich, S. *et al.* Structural insight into cap-snatching and RNA synthesis by influenza polymerase. *Nature* **516**, 361-366, doi:10.1038/nature14009 (2014).

123 Robertson, J. S., Schubert, M. & Lazzarini, R. A. Polyadenylation sites for influenza virus mRNA. *Journal of virology* **38**, 157-163 (1981).

124 Pritlove, D. C., Poon, L. L., Fodor, E., Sharps, J. & Brownlee, G. G. Polyadenylation of influenza virus mRNA transcribed in vitro from model virion RNA templates: requirement for 5' conserved sequences. *Journal of virology* **72**, 1280-1286 (1998).

125 Pritlove, D. C., Poon, L. L., Devenish, L. J., Leahy, M. B. & Brownlee, G. G. A hairpin loop at the 5' end of influenza A virus virion RNA is required for synthesis of poly(A)+ mRNA in vitro. *Journal of virology* **73**, 2109-2114 (1999).

126 Poon, L. L., Pritlove, D. C., Fodor, E. & Brownlee, G. G. Direct evidence that the poly(A) tail of influenza A virus mRNA is synthesized by reiterative copying of a U track in the virion RNA template. *Journal of virology* **73**, 3473-3476 (1999).

127 Hutchinson, E. C. & Yamauchi, Y. Understanding Influenza. *Methods in molecular biology* **1836**, 1-21, doi:10.1007/978-1-4939-8678-1_1 (2018).

128 Inglis, S. C. & Brown, C. M. Spliced and unspliced RNAs encoded by virion RNA segment 7 of influenza virus. *Nucleic acids research* **9**, 2727-2740 (1981).

129 Palese, P., Shaw, M.L. in *Fields Virology* Vol. 5th Edition (ed D. M. Knipe, Howley, P. M.) 1648-1689 (Lippincott Williams & Wilkins, 2007).

130 Deng, T., Vreede, F. T. & Brownlee, G. G. Different de novo initiation strategies are used by influenza virus RNA polymerase on its cRNA and viral RNA promoters during viral RNA replication. *Journal of virology* **80**, 2337-2348, doi:10.1128/JVI.80.5.2337-2348.2006 (2006).

131 Newcomb, L. L. *et al.* Interaction of the influenza a virus nucleocapsid protein with the viral RNA polymerase potentiates unprimed viral RNA replication. *Journal of virology* **83**, 29-36, doi:10.1128/JVI.02293-07 (2009).

132 Robb, N. C. *et al.* Single-molecule FRET reveals the pre-initiation and initiation conformations of influenza virus promoter RNA. *Nucleic acids research* **44**, 10304-10315, doi:10.1093/nar/gkw884 (2016).

133 York, A., Hengrung, N., Vreede, F. T., Huiskonen, J. T. & Fodor, E. Isolation and characterization of the positive-sense replicative intermediate of a negative-strand RNA virus. *Proceedings of the National Academy of Sciences of the United States of America* **110**, E4238-4245, doi:10.1073/pnas.1315068110 (2013).

134 Pflug, A., Lukarska, M., Resa-Infante, P., Reich, S. & Cusack, S. Structural insights into RNA synthesis by the influenza virus transcription-replication machine. *Virus research* **234**, 103-117, doi:10.1016/j.virusres.2017.01.013 (2017).

135 Cao, S. *et al.* A nuclear export signal in the matrix protein of Influenza A virus is required for efficient virus replication. *Journal of virology* **86**, 4883-4891, doi:10.1128/JVI.06586-11 (2012).

136 Chase, G. P. *et al.* Influenza virus ribonucleoprotein complexes gain preferential access to cellular export machinery through chromatin targeting. *PLoS pathogens* **7**, e1002187, doi:10.1371/journal.ppat.1002187 (2011).

137 Iwatsuki-Horimoto, K., Horimoto, T., Fujii, Y. & Kawaoka, Y. Generation of influenza A virus NS2 (NEP) mutants with an altered nuclear export signal sequence. *Journal of virology* **78**, 10149-10155, doi:10.1128/JVI.78.18.10149-10155.2004 (2004).

138 Lakdawala, S. S. *et al.* Influenza a virus assembly intermediates fuse in the cytoplasm. *PLoS pathogens* **10**, e1003971, doi:10.1371/journal.ppat.1003971 (2014).

139 Lakdawala, S. S. *et al.* Correction: Influenza A Virus Assembly Intermediates Fuse in the Cytoplasm. *PLoS pathogens* **12**, e1006121, doi:10.1371/journal.ppat.1006121 (2016).

140 Martin, K. & Helenius, A. Nuclear transport of influenza virus ribonucleoproteins: the viral matrix protein (M1) promotes export and inhibits import. *Cell* **67**, 117-130 (1991).

141 Neumann, G., Hughes, M. T. & Kawaoka, Y. Influenza A virus NS2 protein mediates vRNP nuclear export through NES-independent interaction with hCRM1. *The EMBO journal* **19**, 6751-6758, doi:10.1093/emboj/19.24.6751 (2000).

142 Fukuda, M. *et al.* CRM1 is responsible for intracellular transport mediated by the nuclear export signal. *Nature* **390**, 308-311, doi:10.1038/36894 (1997).

143 Watanabe, K. *et al.* Inhibition of nuclear export of ribonucleoprotein complexes of influenza virus by leptomycin B. *Virus research* **77**, 31-42 (2001).

144 Muhlbauer, D. *et al.* Influenza virus-induced caspase-dependent enlargement of nuclear pores promotes nuclear export of viral ribonucleoprotein complexes. *Journal of virology* **89**, 6009-6021, doi:10.1128/JVI.03531-14 (2015).

145 Kawaguchi, A., Matsumoto, K. & Nagata, K. YB-1 functions as a porter to lead influenza virus ribonucleoprotein complexes to microtubules. *Journal of virology* **86**, 11086-11095, doi:10.1128/JVI.00453-12 (2012).

146 Amorim, M. J. *et al.* A Rab11- and microtubule-dependent mechanism for cytoplasmic transport of influenza A virus viral RNA. *Journal of virology* **85**, 4143-4156, doi:10.1128/JVI.02606-10 (2011).

147 Momose, F., Kikuchi, Y., Komase, K. & Morikawa, Y. Visualization of microtubule-mediated transport of influenza viral progeny ribonucleoprotein. *Microbes and infection* **9**, 1422-1433, doi:10.1016/j.micinf.2007.07.007 (2007).

148 Momose, F. *et al.* Apical transport of influenza A virus ribonucleoprotein requires Rab11-positive recycling endosome. *PloS one* **6**, e21123, doi:10.1371/journal.pone.0021123 (2011).

149 Vale-Costa, S. *et al.* Influenza A virus ribonucleoproteins modulate host recycling by competing with Rab11 effectors. *Journal of cell science* **129**, 1697-1710, doi:10.1242/jcs.188409 (2016).

150 Guichard, A., Nizet, V. & Bier, E. RAB11-mediated trafficking in host-pathogen interactions. *Nature reviews. Microbiology* **12**, 624-634, doi:10.1038/nrmicro3325 (2014).

151 Welz, T., Wellbourne-Wood, J. & Kerkhoff, E. Orchestration of cell surface proteins by Rab11. *Trends in cell biology* **24**, 407-415, doi:10.1016/j.tcb.2014.02.004 (2014).

152 Vale-Costa, S. & Amorim, M. J. Recycling Endosomes and Viral Infection. *Viruses* **8**, 64, doi:10.3390/v8030064 (2016).

153 Fan, G. H., Lapierre, L. A., Goldenring, J. R., Sai, J. & Richmond, A. Rab11-family interacting protein 2 and myosin Vb are required for CXCR2 recycling and receptor-mediated chemotaxis. *Molecular biology of the cell* **15**, 2456-2469, doi:10.1091/mbc.e03-09-0706 (2004).

154 Hales, C. M. *et al.* Identification and characterization of a family of Rab11-interacting proteins. *The Journal of biological chemistry* **276**, 39067-39075, doi:10.1074/jbc.M104831200 (2001).

155 Lapierre, L. A. *et al.* Myosin vb is associated with plasma membrane recycling systems. *Molecular biology of the cell* **12**, 1843-1857, doi:10.1091/mbc.12.6.1843 (2001).

156 Perez Bay, A. E. *et al.* The kinesin KIF16B mediates apical transcytosis of transferrin receptor in AP-1B-deficient epithelia. *The EMBO journal* **32**, 2125-2139, doi:10.1038/emboj.2013.130 (2013).

157 Roland, J. T. *et al.* Rab GTPase-Myo5B complexes control membrane recycling and epithelial polarization. *Proceedings of the National Academy of Sciences of the United States of America* **108**, 2789-2794, doi:10.1073/pnas.1010754108 (2011).

158 Delevoye, C. *et al.* Recycling endosome tubule morphogenesis from sorting endosomes requires the kinesin motor KIF13A. *Cell reports* **6**, 445-454, doi:10.1016/j.celrep.2014.01.002 (2014).

159 Horgan, C. P. & McCaffrey, M. W. The dynamic Rab11-FIPs. *Biochemical Society transactions* **37**, 1032-1036, doi:10.1042/BST0371032 (2009).

160 Bruce, E. A., Digard, P. & Stuart, A. D. The Rab11 pathway is required for influenza A virus budding and filament formation. *Journal of virology* **84**, 5848-5859, doi:10.1128/JVI.00307-10 (2010).

161 Ramos-Nascimento, A. *et al.* KIF13A mediates trafficking of influenza A virus ribonucleoproteins. *Journal of cell science* **130**, 4038-4050, doi:10.1242/jcs.210807 (2017).

162 Avilov, S. V., Moisy, D., Naffakh, N. & Cusack, S. Influenza A virus progeny vRNP trafficking in live infected cells studied with the virus-encoded fluorescently tagged PB2 protein. *Vaccine* **30**, 7411-7417, doi:10.1016/j.vaccine.2012.09.077 (2012).

163 Kumakura, M., Kawaguchi, A. & Nagata, K. Actin-myosin network is required for proper assembly of influenza virus particles. *Virology* **476**, 141-150, doi:10.1016/j.virol.2014.12.016 (2015).

164 Simpson-Holley, M. *et al.* A functional link between the actin cytoskeleton and lipid rafts during budding of filamentous influenza virions. *Virology* **301**, 212-225 (2002).

165 Husain, M. & Cheung, C. Y. Histone deacetylase 6 inhibits influenza A virus release by downregulating the trafficking of viral components to the plasma membrane via its substrate, acetylated microtubules. *Journal of virology* **88**, 11229-11239, doi:10.1128/JVI.00727-14 (2014).

166 Nturibi, E., Bhagwat, A. R., Coburn, S., Myerburg, M. M. & Lakdawala, S. S. Intracellular Colocalization of Influenza Viral RNA and Rab11A Is Dependent upon Microtubule Filaments. *Journal of virology* **91**, doi:10.1128/JVI.01179-17 (2017).

167 Doms, R. W., Lamb, R. A., Rose, J. K. & Helenius, A. Folding and assembly of viral membrane proteins. *Virology* **193**, 545-562, doi:10.1006/viro.1993.1164 (1993).

168 Sun, E., He, J. & Zhuang, X. Dissecting the role of COPI complexes in influenza virus infection. *Journal of virology* **87**, 2673-2685, doi:10.1128/JVI.02277-12 (2013).

169 Barman, S. *et al.* Role of transmembrane domain and cytoplasmic tail amino acid sequences of influenza a virus neuraminidase in raft association and virus budding. *Journal of virology* **78**, 5258-5269 (2004).

170 Ohkura, T., Momose, F., Ichikawa, R., Takeuchi, K. & Morikawa, Y. Influenza A virus hemagglutinin and neuraminidase mutually accelerate their apical targeting through clustering of lipid rafts. *Journal of virology* **88**, 10039-10055, doi:10.1128/JVI.00586-14 (2014).

171 Thaa, B., Herrmann, A. & Veit, M. Intrinsic cytoskeleton-dependent clustering of influenza virus M2 protein with hemagglutinin assessed by FLIM-FRET. *Journal of virology* **84**, 12445-12449, doi:10.1128/JVI.01322-10 (2010).

172 Zhang, J., Pekosz, A. & Lamb, R. A. Influenza virus assembly and lipid raft microdomains: a role for the cytoplasmic tails of the spike glycoproteins. *Journal of virology* **74**, 4634-4644 (2000).

173 Schmitt, A. P. & Lamb, R. A. Influenza virus assembly and budding at the viral budozone. *Advances in virus research* **64**, 383-416, doi:10.1016/S0065-3527(05)64012-2 (2005).

174 Marjuki, H. *et al.* Membrane accumulation of influenza A virus hemagglutinin triggers nuclear export of the viral genome via protein kinase Calpha-mediated activation of ERK signaling. *The Journal of biological chemistry* **281**, 16707-16715, doi:10.1074/jbc.M510233200 (2006).

175 Holsinger, L. J., Shaughnessy, M. A., Micko, A., Pinto, L. H. & Lamb, R. A. Analysis of the posttranslational modifications of the influenza virus M2 protein. *Journal of virology* **69**, 1219-1225 (1995).

176 Schroeder, C., Heider, H., Moncke-Buchner, E. & Lin, T. I. The influenza virus ion channel and maturation cofactor M2 is a cholesterol-binding protein. *European biophysics journal : EBJ* **34**, 52-66, doi:10.1007/s00249-004-0424-1 (2005).

177 Veit, M., Klenk, H. D., Kendal, A. & Rott, R. The M2 protein of influenza A virus is acylated. *The Journal of general virology* **72 (Pt 6)**, 1461-1465, doi:10.1099/0022-1317-72-6-1461 (1991).

178 Noda, T. *et al.* Importance of the 1+7 configuration of ribonucleoprotein complexes for influenza A virus genome packaging. *Nature communications* **9**, 54, doi:10.1038/s41467-017-02517-w (2018).

179 Ali, A., Avalos, R. T., Ponimaskin, E. & Nayak, D. P. Influenza virus assembly: effect of influenza virus glycoproteins on the membrane association of M1 protein. *Journal of virology* **74**, 8709-8719 (2000).

180 Chen, B. J., Leser, G. P., Jackson, D. & Lamb, R. A. The influenza virus M2 protein cytoplasmic tail interacts with the M1 protein and influences virus assembly at the site of virus budding. *Journal of virology* **82**, 10059-10070, doi:10.1128/JVI.01184-08 (2008).

181 Noton, S. L. *et al.* Identification of the domains of the influenza A virus M1 matrix protein required for NP binding, oligomerization and incorporation into virions. *The Journal of general virology* **88**, 2280-2290, doi:10.1099/vir.0.82809-0 (2007).

182 Cox, N. J. & Subbarao, K. Global epidemiology of influenza: past and present. *Annual review of medicine* **51**, 407-421, doi:10.1146/annurev.med.51.1.407 (2000).

183 Paules, C. & Subbarao, K. Influenza. *Lancet* **390**, 697-708, doi:10.1016/S0140-6736(17)30129-0 (2017).

184 Krammer, F. *et al.* Influenza. *Nature reviews. Disease primers* **4**, 3, doi:10.1038/s41572-018-0002-y (2018).

185 Taubenberger, J. K. & Morens, D. M. The pathology of influenza virus infections. *Annual review of pathology* **3**, 499-522, doi:10.1146/annurev.pathmechdis.3.121806.154316 (2008).

186 Shinya, K. *et al.* Avian flu: influenza virus receptors in the human airway. *Nature* **440**, 435-436, doi:10.1038/440435a (2006).

187 Kuiken, T., Riteau, B., Fouchier, R. A. & Rimmelzwaan, G. F. Pathogenesis of influenza virus infections: the good, the bad and the ugly. *Current opinion in virology* **2**, 276-286, doi:10.1016/j.coviro.2012.02.013 (2012).

188 Fukuyama, S. & Kawaoka, Y. The pathogenesis of influenza virus infections: the contributions of virus and host factors. *Current opinion in immunology* **23**, 481-486, doi:10.1016/j.coi.2011.07.016 (2011).

189 Nicholson, K. G. Clinical features of influenza. *Seminars in respiratory infections* **7**, 26-37 (1992).

190 Liu, Y. *et al.* Altered receptor specificity and cell tropism of D222G hemagglutinin mutants isolated from fatal cases of pandemic A(H1N1) 2009 influenza virus. *Journal of virology* **84**, 12069-12074, doi:10.1128/JVI.01639-10 (2010).

191 Mak, G. C. *et al.* Association of D222G substitution in haemagglutinin of 2009 pandemic influenza A (H1N1) with severe disease. *Euro surveillance : bulletin Europeen sur les maladies transmissibles = European communicable disease bulletin* **15** (2010).

192 Otte, A. *et al.* Evolution of 2009 H1N1 influenza viruses during the pandemic correlates with increased viral pathogenicity and transmissibility in the ferret model. *Scientific reports* **6**, 28583, doi:10.1038/srep28583 (2016).

193 Peng, W. *et al.* Recent H3N2 Viruses Have Evolved Specificity for Extended, Branched Human-type Receptors, Conferring Potential for Increased Avidity. *Cell host & microbe* **21**, 23-34, doi:10.1016/j.chom.2016.11.004 (2017).

194 Qi, L. *et al.* Role of sialic acid binding specificity of the 1918 influenza virus hemagglutinin protein in virulence and pathogenesis for mice. *Journal of virology* **83**, 3754-3761, doi:10.1128/JVI.02596-08 (2009).

195 Van Poucke, S. *et al.* Role of Substitutions in the Hemagglutinin in the Emergence of the 1968 Pandemic Influenza Virus. *Journal of virology* **89**, 12211-12216, doi:10.1128/JVI.01292-15 (2015).

196 Xu, R., McBride, R., Paulson, J. C., Basler, C. F. & Wilson, I. A. Structure, receptor binding, and antigenicity of influenza virus hemagglutinins from the 1957 H2N2 pandemic. *Journal of virology* **84**, 1715-1721, doi:10.1128/JVI.02162-09 (2010).

197 Herold, S., Becker, C., Ridge, K. M. & Budinger, G. R. Influenza virus-induced lung injury: pathogenesis and implications for treatment. *The European respiratory journal* **45**, 1463-1478, doi:10.1183/09031936.00186214 (2015).

198 de Jong, M. D. *et al.* Fatal avian influenza A (H5N1) in a child presenting with diarrhea followed by coma. *The New England journal of medicine* **352**, 686-691, doi:10.1056/NEJMoa044307 (2005).

199 Korteweg, C. & Gu, J. Pathology, molecular biology, and pathogenesis of avian influenza A (H5N1) infection in humans. *The American journal of pathology* **172**, 1155-1170, doi:10.2353/ajpath.2008.070791 (2008).

200 Kuiken, T., van den Brand, J., van Riel, D., Pantin-Jackwood, M. & Swayne, D. E. Comparative pathology of select agent influenza a virus infections. *Veterinary pathology* **47**, 893-914, doi:10.1177/0300985810378651 (2010).

201 Short, K. R. *et al.* Influenza virus damages the alveolar barrier by disrupting epithelial cell tight junctions. *The European respiratory journal* **47**, 954-966, doi:10.1183/13993003.01282-2015 (2016).

202 Short, K. R., Kroeze, E., Fouchier, R. A. M. & Kuiken, T. Pathogenesis of influenza-induced acute respiratory distress syndrome. *The Lancet. Infectious diseases* **14**, 57-69, doi:10.1016/S1473-3099(13)70286-X (2014).

203 Liu, Q., Zhou, Y. H. & Yang, Z. Q. The cytokine storm of severe influenza and development of immunomodulatory therapy. *Cellular & molecular immunology* **13**, 3-10, doi:10.1038/cmi.2015.74 (2016).

204 Mutlu, G. M. & Sznajder, J. I. Mechanisms of pulmonary edema clearance. *American journal of physiology. Lung cellular and molecular physiology* **289**, L685-695, doi:10.1152/ajplung.00247.2005 (2005).

205 Mason, R. J. Biology of alveolar type II cells. *Respirology* **11 Suppl**, S12-15, doi:10.1111/j.1440-1843.2006.00800.x (2006).

206 Weinheimer, V. K. *et al.* Influenza A viruses target type II pneumocytes in the human lung. *The Journal of infectious diseases* **206**, 1685-1694, doi:10.1093/infdis/jis455 (2012).

207 Hartsock, A. & Nelson, W. J. Adherens and tight junctions: structure, function and connections to the actin cytoskeleton. *Biochimica et biophysica acta* **1778**, 660-669, doi:10.1016/j.bbamem.2007.07.012 (2008).

208 Rogol, P. R. Intact epithelial barrier function is critical for resolution of alveolar edema in humans. *The American review of respiratory disease* **144**, 468, doi:10.1164/ajrccm/144.2.468 (1991).
209 King, L. S. & Yasui, M. Aquaporins and disease: lessons from mice to humans. *Trends in endocrinology and metabolism: TEM* **13**, 355-360 (2002).
210 Londino, J. D. *et al.* Influenza virus M2 targets cystic fibrosis transmembrane conductance regulator for lysosomal degradation during viral infection. *FASEB journal : official publication of the Federation of American Societies for Experimental Biology* **29**, 2712-2725, doi:10.1096/fj.14-268755 (2015).
211 Chen, X. J. *et al.* Influenza virus inhibits ENaC and lung fluid clearance. *American journal of physiology. Lung cellular and molecular physiology* **287**, L366-373, doi:10.1152/ajplung.00011.2004 (2004).
212 Lazrak, A. *et al.* Influenza virus M2 protein inhibits epithelial sodium channels by increasing reactive oxygen species. *FASEB journal : official publication of the Federation of American Societies for Experimental Biology* **23**, 3829-3842, doi:10.1096/fj.09-135590 (2009).
213 Londino, J. D. *et al.* Influenza matrix protein 2 alters CFTR expression and function through its ion channel activity. *American journal of physiology. Lung cellular and molecular physiology* **304**, L582-592, doi:10.1152/ajplung.00314.2012 (2013).
214 Peteranderl, C. *et al.* Macrophage-epithelial paracrine crosstalk inhibits lung edema clearance during influenza infection. *The Journal of clinical investigation* **126**, 1566-1580, doi:10.1172/JCI83931 (2016).
215 Kaplan, J. H. Biochemistry of Na,K-ATPase. *Annual review of biochemistry* **71**, 511-535, doi:10.1146/annurev.biochem.71.102201.141218 (2002).
216 Suhail, M. Na, K-ATPase: Ubiquitous Multifunctional Transmembrane Protein and its Relevance to Various Pathophysiological Conditions. *Journal of clinical medicine research* **2**, 1-17, doi:10.4021/jocmr2010.02.263w (2010).
217 Clausen, T. Quantification of Na+,K+ pumps and their transport rate in skeletal muscle: functional significance. *The Journal of general physiology* **142**, 327-345, doi:10.1085/jgp.201310980 (2013).
218 Clausen, M. V., Hilbers, F. & Poulsen, H. The Structure and Function of the Na,K-ATPase Isoforms in Health and Disease. *Frontiers in physiology* **8**, 371, doi:10.3389/fphys.2017.00371 (2017).
219 Dempski, R. E., Friedrich, T. & Bamberg, E. The beta subunit of the Na+/K+-ATPase follows the conformational state of the holoenzyme. *The Journal of general physiology* **125**, 505-520, doi:10.1085/jgp.200409186 (2005).
220 Geering, K. The functional role of beta subunits in oligomeric P-type ATPases. *Journal of bioenergetics and biomembranes* **33**, 425-438 (2001).
221 Geering, K. Functional roles of Na,K-ATPase subunits. *Current opinion in nephrology and hypertension* **17**, 526-532, doi:10.1097/MNH.0b013e3283036cbf (2008).
222 Geering, K. Function of FXYD proteins, regulators of Na, K-ATPase. *Journal of bioenergetics and biomembranes* **37**, 387-392, doi:10.1007/s10863-005-9476-x (2005).
223 Tokhtaeva, E., Sachs, G. & Vagin, O. Assembly with the Na,K-ATPase alpha(1) subunit is required for export of beta(1) and beta(2) subunits from the endoplasmic reticulum. *Biochemistry* **48**, 11421-11431, doi:10.1021/bi901438z (2009).
224 Vagin, O., Sachs, G. & Tokhtaeva, E. The roles of the Na,K-ATPase beta 1 subunit in pump sorting and epithelial integrity. *Journal of bioenergetics and biomembranes* **39**, 367-372, doi:10.1007/s10863-007-9103-0 (2007).
225 Yoshimura, S. H., Iwasaka, S., Schwarz, W. & Takeyasu, K. Fast degradation of the auxiliary subunit of Na+/K+-ATPase in the plasma membrane of HeLa cells. *Journal of cell science* **121**, 2159-2168, doi:10.1242/jcs.022905 (2008).
226 Morton, M. J. *et al.* Association with {beta}-COP regulates the trafficking of the newly synthesized Na,K-ATPase. *The Journal of biological chemistry* **285**, 33737-33746, doi:10.1074/jbc.M110.141119 (2010).
227 Padilla-Benavides, T. *et al.* The polarized distribution of Na+,K+-ATPase: role of the interaction between {beta} subunits. *Molecular biology of the cell* **21**, 2217-2225, doi:10.1091/mbc.E10-01-0081 (2010).

228 Vagin, O., Tokhtaeva, E. & Sachs, G. The role of the beta1 subunit of the Na,K-ATPase and its glycosylation in cell-cell adhesion. *The Journal of biological chemistry* **281**, 39573-39587, doi:10.1074/jbc.M606507200 (2006).

229 Lobato-Alvarez, J. A. *et al.* The Apical Localization of Na(+), K(+)-ATPase in Cultured Human Retinal Pigment Epithelial Cells Depends on Expression of the beta2 Subunit. *Frontiers in physiology* **7**, 450, doi:10.3389/fphys.2016.00450 (2016).

230 Wilson, P. D. *et al.* Apical plasma membrane mispolarization of NaK-ATPase in polycystic kidney disease epithelia is associated with aberrant expression of the beta2 isoform. *The American journal of pathology* **156**, 253-268 (2000).

231 Blanco, G., DeTomaso, A. W., Koster, J., Xie, Z. J. & Mercer, R. W. The alpha-subunit of the Na,K-ATPase has catalytic activity independent of the beta-subunit. *The Journal of biological chemistry* **269**, 23420-23425 (1994).

232 DeTomaso, A. W., Blanco, G. & Mercer, R. W. The alpha and beta subunits of the Na,K-ATPase can assemble at the plasma membrane into functional enzyme. *The Journal of cell biology* **127**, 55-69 (1994).

233 Lodish H, B. A., Zipursky SL, et al. in *Molecular Cell Biology.* Ch. Section 15.4, (New York: W. H. Freeman, 2000).

234 Milligan, L. P. & McBride, B. W. Energy costs of ion pumping by animal tissues. *The Journal of nutrition* **115**, 1374-1382, doi:10.1093/jn/115.10.1374 (1985).

235 Rajasekaran, S. A., Barwe, S. P. & Rajasekaran, A. K. Multiple functions of Na,K-ATPase in epithelial cells. *Seminars in nephrology* **25**, 328-334, doi:10.1016/j.semnephrol.2005.03.008 (2005).

236 Sznajder, J. I., Factor, P. & Ingbar, D. H. Invited review: lung edema clearance: role of Na(+)-K(+)-ATPase. *Journal of applied physiology* **93**, 1860-1866, doi:10.1152/japplphysiol.00022.2002 (2002).

237 Rajasekaran, S. A. *et al.* Na,K-ATPase activity is required for formation of tight junctions, desmosomes, and induction of polarity in epithelial cells. *Molecular biology of the cell* **12**, 3717-3732, doi:10.1091/mbc.12.12.3717 (2001).

238 Rajasekaran, S. A. *et al.* Na,K-ATPase beta-subunit is required for epithelial polarization, suppression of invasion, and cell motility. *Molecular biology of the cell* **12**, 279-295, doi:10.1091/mbc.12.2.279 (2001).

239 Rajasekaran, S. A. & Rajasekaran, A. K. Na,K-ATPase and epithelial tight junctions. *Frontiers in bioscience* **14**, 2130-2148 (2009).

240 Rajasekaran, S. A. *et al.* Na,K-ATPase inhibition alters tight junction structure and permeability in human retinal pigment epithelial cells. *American journal of physiology. Cell physiology* **284**, C1497-1507, doi:10.1152/ajpcell.00355.2002 (2003).

241 Cui, X. & Xie, Z. Protein Interaction and Na/K-ATPase-Mediated Signal Transduction. *Molecules* **22**, doi:10.3390/molecules22060990 (2017).

242 Pratt, R. D., Brickman, C. R., Cottrill, C. L., Shapiro, J. I. & Liu, J. The Na/K-ATPase Signaling: From Specific Ligands to General Reactive Oxygen Species. *International journal of molecular sciences* **19**, doi:10.3390/ijms19092600 (2018).

243 Xie, Z. Molecular mechanisms of Na/K-ATPase-mediated signal transduction. *Annals of the New York Academy of Sciences* **986**, 497-503 (2003).

244 Zhang, L., Zhang, Z., Guo, H. & Wang, Y. Na+/K+-ATPase-mediated signal transduction and Na+/K+-ATPase regulation. *Fundamental & clinical pharmacology* **22**, 615-621, doi:10.1111/j.1472-8206.2008.00620.x (2008).

245 Li, Z. & Langhans, S. A. Transcriptional regulators of Na,K-ATPase subunits. *Frontiers in cell and developmental biology* **3**, 66, doi:10.3389/fcell.2015.00066 (2015).

246 Clifford, R. J. & Kaplan, J. H. Regulation of Na,K-ATPase subunit abundance by translational repression. *The Journal of biological chemistry* **284**, 22905-22915, doi:10.1074/jbc.M109.030536 (2009).

247 Espineda, C. E., Chang, J. H., Twiss, J., Rajasekaran, S. A. & Rajasekaran, A. K. Repression of Na,K-ATPase beta1-subunit by the transcription factor snail in carcinoma. *Molecular biology of the cell* **15**, 1364-1373, doi:10.1091/mbc.e03-09-0646 (2004).

248 Schwartze, J. T. *et al.* Glucocorticoids recruit Tgfbr3 and Smad1 to shift transforming growth factor-beta signaling from the Tgfbr1/Smad2/3 axis to the Acvrl1/Smad1 axis in lung

fibroblasts. *The Journal of biological chemistry* **289**, 3262-3275, doi:10.1074/jbc.M113.541052 (2014).

249 Lecuona, E., Trejo, H. E. & Sznajder, J. I. Regulation of Na,K-ATPase during acute lung injury. *Journal of bioenergetics and biomembranes* **39**, 391-395, doi:10.1007/s10863-007-9102-1 (2007).

250 Vadasz, I. & Sznajder, J. I. Gas Exchange Disturbances Regulate Alveolar Fluid Clearance during Acute Lung Injury. *Frontiers in immunology* **8**, 757, doi:10.3389/fimmu.2017.00757 (2017).

251 Chibalin, A. V. *et al.* Dopamine-induced endocytosis of Na+,K+-ATPase is initiated by phosphorylation of Ser-18 in the rat alpha subunit and Is responsible for the decreased activity in epithelial cells. *The Journal of biological chemistry* **274**, 1920-1927 (1999).

252 Chibalin, A. V. *et al.* Phosphorylation of the catalyic alpha-subunit constitutes a triggering signal for Na+,K+-ATPase endocytosis. *The Journal of biological chemistry* **273**, 8814-8819 (1998).

253 Dada, L. A. *et al.* Phosphorylation and ubiquitination are necessary for Na,K-ATPase endocytosis during hypoxia. *Cellular signalling* **19**, 1893-1898, doi:10.1016/j.cellsig.2007.04.013 (2007).

254 Dada, L. A., Novoa, E., Lecuona, E., Sun, H. & Sznajder, J. I. Role of the small GTPase RhoA in the hypoxia-induced decrease of plasma membrane Na,K-ATPase in A549 cells. *Journal of cell science* **120**, 2214-2222, doi:10.1242/jcs.003038 (2007).

255 Lamaze, C., Chuang, T. H., Terlecky, L. J., Bokoch, G. M. & Schmid, S. L. Regulation of receptor-mediated endocytosis by Rho and Rac. *Nature* **382**, 177-179, doi:10.1038/382177a0 (1996).

256 Lecuona, E. *et al.* Protein kinase A-Ialpha regulates Na,K-ATPase endocytosis in alveolar epithelial cells exposed to high CO(2) concentrations. *American journal of respiratory cell and molecular biology* **48**, 626-634, doi:10.1165/rcmb.2012-0373OC (2013).

257 Bertorello, A. M. *et al.* Analysis of Na+,K+-ATPase motion and incorporation into the plasma membrane in response to G protein-coupled receptor signals in living cells. *Molecular biology of the cell* **14**, 1149-1157, doi:10.1091/mbc.e02-06-0367 (2003).

258 Bertorello, A. M., Ridge, K. M., Chibalin, A. V., Katz, A. I. & Sznajder, J. I. Isoproterenol increases Na+-K+-ATPase activity by membrane insertion of alpha-subunits in lung alveolar cells. *The American journal of physiology* **276**, L20-27 (1999).

259 Ridge, K. M. *et al.* Dopamine-induced exocytosis of Na,K-ATPase is dependent on activation of protein kinase C-epsilon and -delta. *Molecular biology of the cell* **13**, 1381-1389, doi:10.1091/mbc.01-07-0323 (2002).

260 Saldias, F. J. *et al.* beta-adrenergic stimulation restores rat lung ability to clear edema in ventilator-associated lung injury. *American journal of respiratory and critical care medicine* **162**, 282-287, doi:10.1164/ajrccm.162.1.9809058 (2000).

261 Comellas, A. P. *et al.* Insulin regulates alveolar epithelial function by inducing Na+/K+-ATPase translocation to the plasma membrane in a process mediated by the action of Akt. *Journal of cell science* **123**, 1343-1351, doi:10.1242/jcs.066464 (2010).

262 Lecuona, E. *et al.* Na,K-ATPase alpha1-subunit dephosphorylation by protein phosphatase 2A is necessary for its recruitment to the plasma membrane. *FASEB journal : official publication of the Federation of American Societies for Experimental Biology* **20**, 2618-2620, doi:10.1096/fj.06-6503fje (2006).

263 Trejo, H. E. *et al.* Role of kinesin light chain-2 of kinesin-1 in the traffic of Na,K-ATPase-containing vesicles in alveolar epithelial cells. *FASEB journal : official publication of the Federation of American Societies for Experimental Biology* **24**, 374-382, doi:10.1096/fj.09-137802 (2010).

264 Javaherian, S., Paz, A. C. & McGuigan, A. P. Micropatterning cells on permeable membrane filters. *Methods in cell biology* **121**, 171-189, doi:10.1016/B978-0-12-800281-0.00012-9 (2014).

265 Powell, J. D. S. T. M. Advances and Remaining Challenges in the Study of Influenza and Anthrax Infection in Lung Cell Culture. *Challenges* **Volume 9**, doi:10.3390/challe9010002 (2018).

266 Vagin, O., Turdikulova, S. & Tokhtaeva, E. Polarized membrane distribution of potassium-dependent ion pumps in epithelial cells: different roles of the N-glycans of their beta subunits. *Cell biochemistry and biophysics* **47**, 376-391 (2007).

267 Efendiev, R., Das-Panja, K., Cinelli, A. R., Bertorello, A. M. & Pedemonte, C. H. Localization of intracellular compartments that exchange Na,K-ATPase molecules with the plasma membrane in a hormone-dependent manner. *British journal of pharmacology* **151**, 1006-1013, doi:10.1038/sj.bjp.0707304 (2007).

268 Welch, L. C. *et al.* Extracellular signal-regulated kinase (ERK) participates in the hypercapnia-induced Na,K-ATPase downregulation. *FEBS letters* **584**, 3985-3989, doi:10.1016/j.febslet.2010.08.002 (2010).

269 Haidari, M., Zhang, W., Ganjehei, L., Ali, M. & Chen, Z. Inhibition of MLC phosphorylation restricts replication of influenza virus--a mechanism of action for anti-influenza agents. *PloS one* **6**, e21444, doi:10.1371/journal.pone.0021444 (2011).

270 Hennet, T., Ziltener, H. J., Frei, K. & Peterhans, E. A kinetic study of immune mediators in the lungs of mice infected with influenza A virus. *Journal of immunology* **149**, 932-939 (1992).

271 Jacoby, D. B. & Choi, A. M. Influenza virus induces expression of antioxidant genes in human epithelial cells. *Free radical biology & medicine* **16**, 821-824 (1994).

272 Knobil, K., Choi, A. M., Weigand, G. W. & Jacoby, D. B. Role of oxidants in influenza virus-induced gene expression. *The American journal of physiology* **274**, L134-142 (1998).

273 Lin, X. *et al.* The Influenza Virus H5N1 Infection Can Induce ROS Production for Viral Replication and Host Cell Death in A549 Cells Modulated by Human Cu/Zn Superoxide Dismutase (SOD1) Overexpression. *Viruses* **8**, doi:10.3390/v8010013 (2016).

274 Oda, T. *et al.* Oxygen radicals in influenza-induced pathogenesis and treatment with pyran polymer-conjugated SOD. *Science* **244**, 974-976 (1989).

275 Pinto, R. *et al.* Inhibition of influenza virus-induced NF-kappaB and Raf/MEK/ERK activation can reduce both virus titers and cytokine expression simultaneously in vitro and in vivo. *Antiviral research* **92**, 45-56, doi:10.1016/j.antiviral.2011.05.009 (2011).

276 Reshi, M. L., Su, Y. C. & Hong, J. R. RNA Viruses: ROS-Mediated Cell Death. *International journal of cell biology* **2014**, 467452, doi:10.1155/2014/467452 (2014).

277 Zhang, C. *et al.* p38MAPK, Rho/ROCK and PKC pathways are involved in influenza-induced cytoskeletal rearrangement and hyperpermeability in PMVEC via phosphorylating ERM. *Virus research* **192**, 6-15, doi:10.1016/j.virusres.2014.07.027 (2014).

278 Duncia, J. V. *et al.* MEK inhibitors: the chemistry and biological activity of U0126, its analogs, and cyclization products. *Bioorganic & medicinal chemistry letters* **8**, 2839-2844 (1998).

279 Asano, T. *et al.* Vasodilator actions of HA1077 in vitro and in vivo putatively mediated by the inhibition of protein kinase. *British journal of pharmacology* **98**, 1091-1100 (1989).

280 Nagumo, H. *et al.* Rho kinase inhibitor HA-1077 prevents Rho-mediated myosin phosphatase inhibition in smooth muscle cells. *American journal of physiology. Cell physiology* **278**, C57-65, doi:10.1152/ajpcell.2000.278.1.C57 (2000).

281 Saitoh, M., Ishikawa, T., Matsushima, S., Naka, M. & Hidaka, H. Selective inhibition of catalytic activity of smooth muscle myosin light chain kinase. *The Journal of biological chemistry* **262**, 7796-7801 (1987).

282 Casella, J. F., Flanagan, M. D. & Lin, S. Cytochalasin D inhibits actin polymerization and induces depolymerization of actin filaments formed during platelet shape change. *Nature* **293**, 302-305 (1981).

283 Holzinger, A. Jasplakinolide: an actin-specific reagent that promotes actin polymerization. *Methods in molecular biology* **586**, 71-87, doi:10.1007/978-1-60761-376-3_4 (2009).

284 Sciaky, N. *et al.* Golgi tubule traffic and the effects of brefeldin A visualized in living cells. *The Journal of cell biology* **139**, 1137-1155 (1997).

285 Lecuona, E., Sun, H., Vohwinkel, C., Ciechanover, A. & Sznajder, J. I. Ubiquitination participates in the lysosomal degradation of Na,K-ATPase in steady-state conditions. *American journal of respiratory cell and molecular biology* **41**, 671-679, doi:10.1165/rcmb.2008-0365OC (2009).

286 Vale-Costa, S. & Amorim, M. J. Clustering of Rab11 vesicles in influenza A virus infected cells creates hotspots containing the 8 viral ribonucleoproteins. *Small GTPases* **8**, 71-77, doi:10.1080/21541248.2016.1199190 (2017).

287 De Brabander, M. J., Van de Veire, R. M., Aerts, F. E., Borgers, M. & Janssen, P. A. The effects of methyl (5-(2-thienylcarbonyl)-1H-benzimidazol-2-yl) carbamate, (R 17934; NSC 238159), a new synthetic antitumoral drug interfering with microtubules, on mammalian cells cultured in vitro. *Cancer research* **36**, 905-916 (1976).

288 Weaver, B. A. How Taxol/paclitaxel kills cancer cells. *Molecular biology of the cell* **25**, 2677-2681, doi:10.1091/mbc.E14-04-0916 (2014).

289 Kawaguchi, K. & Ishiwata, S. Nucleotide-dependent single- to double-headed binding of kinesin. *Science* **291**, 667-669, doi:10.1126/science.291.5504.667 (2001).

290 Korten, T., Tavkin, E., Scharrel, L., Kushwaha, V. S. & Diez, S. An automated in vitro motility assay for high-throughput studies of molecular motors. *Lab on a chip* **18**, 3196-3206, doi:10.1039/c8lc00547h (2018).

291 Kuznetsov, S. A. & Gelfand, V. I. Bovine brain kinesin is a microtubule-activated ATPase. *Proceedings of the National Academy of Sciences of the United States of America* **83**, 8530-8534 (1986).

292 Kuznetsov, S. A. & Gel'fand, V. I. [Kinesin from the bovine brain: a novel mechanochemical ATPase activated by microtubules]. *Doklady Akademii nauk SSSR* **291**, 1505-1509 (1986).

293 Cai, D., McEwen, D. P., Martens, J. R., Meyhofer, E. & Verhey, K. J. Single molecule imaging reveals differences in microtubule track selection between Kinesin motors. *PLoS biology* **7**, e1000216, doi:10.1371/journal.pbio.1000216 (2009).

294 Katrukha, E. A. *et al.* Probing cytoskeletal modulation of passive and active intracellular dynamics using nanobody-functionalized quantum dots. *Nature communications* **8**, 14772, doi:10.1038/ncomms14772 (2017).

295 Reed, N. A. *et al.* Microtubule acetylation promotes kinesin-1 binding and transport. *Current biology : CB* **16**, 2166-2172, doi:10.1016/j.cub.2006.09.014 (2006).

296 Hammond, J. W., Cai, D. & Verhey, K. J. Tubulin modifications and their cellular functions. *Current opinion in cell biology* **20**, 71-76, doi:10.1016/j.ceb.2007.11.010 (2008).

297 Song, Y. & Brady, S. T. Post-translational modifications of tubulin: pathways to functional diversity of microtubules. *Trends in cell biology* **25**, 125-136, doi:10.1016/j.tcb.2014.10.004 (2015).

298 Wloga, D., Joachimiak, E. & Fabczak, H. Tubulin Post-Translational Modifications and Microtubule Dynamics. *International journal of molecular sciences* **18**, doi:10.3390/ijms18102207 (2017).

299 Husain, M. & Harrod, K. S. Enhanced acetylation of alpha-tubulin in influenza A virus infected epithelial cells. *FEBS letters* **585**, 128-132, doi:10.1016/j.febslet.2010.11.023 (2011).

300 Schofield, A. V., Gamell, C., Suryadinata, R., Sarcevic, B. & Bernard, O. Tubulin polymerization promoting protein 1 (Tppp1) phosphorylation by Rho-associated coiled-coil kinase (rock) and cyclin-dependent kinase 1 (Cdk1) inhibits microtubule dynamics to increase cell proliferation. *The Journal of biological chemistry* **288**, 7907-7917, doi:10.1074/jbc.M112.441048 (2013).

301 Schofield, A. V., Steel, R. & Bernard, O. Rho-associated coiled-coil kinase (ROCK) protein controls microtubule dynamics in a novel signaling pathway that regulates cell migration. *The Journal of biological chemistry* **287**, 43620-43629, doi:10.1074/jbc.M112.394965 (2012).

302 Patel, R. A. *et al.* RKI-1447 is a potent inhibitor of the Rho-associated ROCK kinases with anti-invasive and antitumor activities in breast cancer. *Cancer research* **72**, 5025-5034, doi:10.1158/0008-5472.CAN-12-0954 (2012).

303 Husain, M. & Harrod, K. S. Influenza A virus-induced caspase-3 cleaves the histone deacetylase 6 in infected epithelial cells. *FEBS letters* **583**, 2517-2520, doi:10.1016/j.febslet.2009.07.005 (2009).

304 Haggarty, S. J., Koeller, K. M., Wong, J. C., Grozinger, C. M. & Schreiber, S. L. Domain-selective small-molecule inhibitor of histone deacetylase 6 (HDAC6)-mediated tubulin deacetylation. *Proceedings of the National Academy of Sciences of the United States of America* **100**, 4389-4394, doi:10.1073/pnas.0430973100 (2003).

305 Banerjee, I. *et al.* Influenza A virus uses the aggresome processing machinery for host cell entry. *Science* **346**, 473-477, doi:10.1126/science.1257037 (2014).

306 Shi, J. & Wei, L. Rho kinase in the regulation of cell death and survival. *Archivum immunologiae et therapiae experimentalis* **55**, 61-75, doi:10.1007/s00005-007-0009-7 (2007).

307 Garcia-Calvo, M. *et al.* Inhibition of human caspases by peptide-based and macromolecular inhibitors. *The Journal of biological chemistry* **273**, 32608-32613 (1998).

308 Thornberry, N. A. *et al.* A combinatorial approach defines specificities of members of the caspase family and granzyme B. Functional relationships established for key mediators of apoptosis. *The Journal of biological chemistry* **272**, 17907-17911 (1997).

309 Kleyman, T. R. & Cragoe, E. J., Jr. Amiloride and its analogs as tools in the study of ion transport. *The Journal of membrane biology* **105**, 1-21 (1988).

310 Luyt, C. E., Combes, A., Trouillet, J. L., Nieszkowska, A. & Chastre, J. Virus-induced acute respiratory distress syndrome: epidemiology, management and outcome. *Presse medicale* **40**, e561-568, doi:10.1016/j.lpm.2011.05.027 (2011).

311 Brand, J. D. *et al.* Influenza-mediated reduction of lung epithelial ion channel activity leads to dysregulated pulmonary fluid homeostasis. *JCI insight* **3**, doi:10.1172/jci.insight.123467 (2018).

312 Kunzelmann, K. *et al.* Influenza virus inhibits amiloride-sensitive Na+ channels in respiratory epithelia. *Proceedings of the National Academy of Sciences of the United States of America* **97**, 10282-10287, doi:10.1073/pnas.160041997 (2000).

313 Londino, J. D. *et al.* Influenza virus infection alters ion channel function of airway and alveolar cells: mechanisms and physiological sequelae. *American journal of physiology. Lung cellular and molecular physiology* **313**, L845-L858, doi:10.1152/ajplung.00244.2017 (2017).

314 Vohwinkel, C. U. & Vadasz, I. Influenza A matrix protein M2 downregulates CFTR: inhibition of chloride transport by a proton channel of the viral envelope. *American journal of physiology. Lung cellular and molecular physiology* **304**, L813-816, doi:10.1152/ajplung.00091.2013 (2013).

315 Teixeira, V. L., Katz, A. I., Pedemonte, C. H. & Bertorello, A. M. Isoform-specific regulation of Na+,K+-ATPase endocytosis and recruitment to the plasma membrane. *Annals of the New York Academy of Sciences* **986**, 587-594 (2003).

316 Pleschka, S. *et al.* Influenza virus propagation is impaired by inhibition of the Raf/MEK/ERK signalling cascade. *Nature cell biology* **3**, 301-305, doi:10.1038/35060098 (2001).

317 Constantinescu, S. N., Cernescu, C. D. & Popescu, L. M. Effects of protein kinase C inhibitors on viral entry and infectivity. *FEBS letters* **292**, 31-33 (1991).

318 Fujioka, Y. *et al.* A Ca(2+)-dependent signalling circuit regulates influenza A virus internalization and infection. *Nature communications* **4**, 2763, doi:10.1038/ncomms3763 (2013).

319 Marjuki, H. *et al.* Influenza A virus-induced early activation of ERK and PI3K mediates V-ATPase-dependent intracellular pH change required for fusion. *Cellular microbiology* **13**, 587-601, doi:10.1111/j.1462-5822.2010.01556.x (2011).

320 Mondal, A. *et al.* Influenza virus recruits host protein kinase C to control assembly and activity of its replication machinery. *eLife* **6**, doi:10.7554/eLife.26910 (2017).

321 Root, C. N., Wills, E. G., McNair, L. L. & Whittaker, G. R. Entry of influenza viruses into cells is inhibited by a highly specific protein kinase C inhibitor. *The Journal of general virology* **81**, 2697-2705, doi:10.1099/0022-1317-81-11-2697 (2000).

322 Sieczkarski, S. B., Brown, H. A. & Whittaker, G. R. Role of protein kinase C betaII in influenza virus entry via late endosomes. *Journal of virology* **77**, 460-469 (2003).

323 Lecuona, E., Ridge, K., Pesce, L., Batlle, D. & Sznajder, J. I. The GTP-binding protein RhoA mediates Na,K-ATPase exocytosis in alveolar epithelial cells. *Molecular biology of the cell* **14**, 3888-3897, doi:10.1091/mbc.e02-12-0781 (2003).

324 Pohl, M. O., Lanz, C. & Stertz, S. Late stages of the influenza A virus replication cycle-a tight interplay between virus and host. *The Journal of general virology* **97**, 2058-2072, doi:10.1099/jgv.0.000562 (2016).

325 Lecuona, E. *et al.* Myosin-Va restrains the trafficking of Na+/K+-ATPase-containing vesicles in alveolar epithelial cells. *Journal of cell science* **122**, 3915-3922, doi:10.1242/jcs.046953 (2009).

326 Eisfeld, A. J., Kawakami, E., Watanabe, T., Neumann, G. & Kawaoka, Y. RAB11A is essential for transport of the influenza virus genome to the plasma membrane. *Journal of virology* **85**, 6117-6126, doi:10.1128/JVI.00378-11 (2011).

327 Eisfeld, A. J., Neumann, G. & Kawaoka, Y. At the centre: influenza A virus ribonucleoproteins. *Nature reviews. Microbiology* **13**, 28-41, doi:10.1038/nrmicro3367 (2015).

328 Matsuzaki, F., Shirane, M., Matsumoto, M. & Nakayama, K. I. Protrudin serves as an adaptor molecule that connects KIF5 and its cargoes in vesicular transport during process formation. *Molecular biology of the cell* **22**, 4602-4620, doi:10.1091/mbc.E11-01-0068 (2011).

329 Janke, C. & Montagnac, G. Causes and Consequences of Microtubule Acetylation. *Current biology : CB* **27**, R1287-R1292, doi:10.1016/j.cub.2017.10.044 (2017).

330 Portran, D., Schaedel, L., Xu, Z., Thery, M. & Nachury, M. V. Tubulin acetylation protects long-lived microtubules against mechanical ageing. *Nature cell biology* **19**, 391-398, doi:10.1038/ncb3481 (2017).

331 Xu, Z. *et al.* Microtubules acquire resistance from mechanical breakage through intralumenal acetylation. *Science* **356**, 328-332, doi:10.1126/science.aai8764 (2017).

332 Schofield, A. V., Gamell, C. & Bernard, O. Tubulin polymerization promoting protein 1 (TPPP1) increases beta-catenin expression through inhibition of HDAC6 activity in U2OS osteosarcoma cells. *Biochemical and biophysical research communications* **436**, 571-577, doi:10.1016/j.bbrc.2013.05.076 (2013).

333 Tokesi, N. *et al.* TPPP/p25 promotes tubulin acetylation by inhibiting histone deacetylase 6. *The Journal of biological chemistry* **285**, 17896-17906, doi:10.1074/jbc.M109.096578 (2010).

334 Hensel, N. *et al.* ERK and ROCK functionally interact in a signaling network that is compensationally upregulated in Spinal Muscular Atrophy. *Neurobiology of disease* **108**, 352-361, doi:10.1016/j.nbd.2017.09.005 (2017).

335 Seidel, C., Schnekenburger, M., Dicato, M. & Diederich, M. Histone deacetylase 6 in health and disease. *Epigenomics* **7**, 103-118, doi:10.2217/epi.14.69 (2015).

336 Williams, K. A. *et al.* Extracellular signal-regulated kinase (ERK) phosphorylates histone deacetylase 6 (HDAC6) at serine 1035 to stimulate cell migration. *The Journal of biological chemistry* **288**, 33156-33170, doi:10.1074/jbc.M113.472506 (2013).

337 Wurzer, W. J. *et al.* Caspase 3 activation is essential for efficient influenza virus propagation. *The EMBO journal* **22**, 2717-2728, doi:10.1093/emboj/cdg279 (2003).

338 Tarran, R. Regulation of airway surface liquid volume and mucus transport by active ion transport. *Proceedings of the American Thoracic Society* **1**, 42-46, doi:10.1513/pats.2306014 (2004).

339 Widdicombe, J. H. Regulation of the depth and composition of airway surface liquid. *Journal of anatomy* **201**, 313-318 (2002).

340 Arce, C. A., Casale, C. H. & Barra, H. S. Submembraneous microtubule cytoskeleton: regulation of ATPases by interaction with acetylated tubulin. *The FEBS journal* **275**, 4664-4674, doi:10.1111/j.1742-4658.2008.06615.x (2008).

341 Feng, Y., LoGrasso, P. V., Defert, O. & Li, R. Rho Kinase (ROCK) Inhibitors and Their Therapeutic Potential. *Journal of medicinal chemistry* **59**, 2269-2300, doi:10.1021/acs.jmedchem.5b00683 (2016).

342 Akaihata, H. *et al.* Protective Effect of a Rho-kinase Inhibitor on Bladder Dysfunction in a Rat Model of Chronic Bladder Ischemia. *Urology* **111**, 238 e237-238 e212, doi:10.1016/j.urology.2017.10.007 (2018).

343 Holmstrom, F. *et al.* Protective effect of hydroxyfasudil, a Rho kinase inhibitor, on ventral prostatic hyperplasia in the spontaneously hypertensive rat. *The Prostate* **75**, 1774-1782, doi:10.1002/pros.23063 (2015).

344 Komers, R. *et al.* Rho kinase inhibition protects kidneys from diabetic nephropathy without reducing blood pressure. *Kidney international* **79**, 432-442, doi:10.1038/ki.2010.428 (2011).

345 Li, Y. H. *et al.* Protective effect of a novel Rho kinase inhibitor WAR-5 in experimental autoimmune encephalomyelitis by modulating inflammatory response and neurotrophic factors. *Experimental and molecular pathology* **99**, 220-228, doi:10.1016/j.yexmp.2015.06.016 (2015).

346 Mueller, B. K., Mack, H. & Teusch, N. Rho kinase, a promising drug target for neurological disorders. *Nature reviews. Drug discovery* **4**, 387-398, doi:10.1038/nrd1719 (2005).

347 Olson, M. F. Applications for ROCK kinase inhibition. *Current opinion in cell biology* **20**, 242-248, doi:10.1016/j.ceb.2008.01.002 (2008).

348 Peng, X. C., Chen, X. X., Zhang, Y. U., Wang, H. J. & Feng, Y. A novel inhibitor of Rho GDP-dissociation inhibitor alpha improves the therapeutic efficacy of paclitaxel in Lewis lung carcinoma. *Biomedical reports* **3**, 473-477, doi:10.3892/br.2015.475 (2015).

349 Rath, N. & Olson, M. F. Rho-associated kinases in tumorigenesis: re-considering ROCK inhibition for cancer therapy. *EMBO reports* **13**, 900-908, doi:10.1038/embor.2012.127 (2012).

350 Wilhelm, I. *et al.* Role of Rho/ROCK signaling in the interaction of melanoma cells with the blood-brain barrier. *Pigment cell & melanoma research* **27**, 113-123, doi:10.1111/pcmr.12169 (2014).

351 Cinel, I. *et al.* Involvement of Rho kinase (ROCK) in sepsis-induced acute lung injury. *Journal of thoracic disease* **4**, 30-39, doi:10.3978/j.issn.2072-1439.2010.08.04 (2012).

352 Ohata, K. *et al.* Protective Effect of Inhaled Rho-Kinase Inhibitor on Lung Ischemia-Reperfusion Injury. *The Annals of thoracic surgery* **103**, 476-483, doi:10.1016/j.athoracsur.2016.07.067 (2017).

353 Wang, Y., Wang, X., Liu, W. & Zhang, L. Role of the Rho/ROCK signaling pathway in the protective effects of fasudil against acute lung injury in septic rats. *Molecular medicine reports* **18**, 4486-4498, doi:10.3892/mmr.2018.9446 (2018).

354 Zhang, H. *et al.* [Role of Rho/ROCK signaling pathway in the protective effects of hydrogen against acute lung injury in septic mice]. *Zhonghua wei zhong bing ji jiu yi xue* **28**, 401-406 (2016).

355 Zhang, L., Li, Q., Liu, Z., Liu, W. & Zhao, M. Protective Effects of a Rho Kinase Inhibitor on Paraquat-Induced Acute Lung Injuries in Rats. *Inflammation* **41**, 2171-2183, doi:10.1007/s10753-018-0860-1 (2018).

8. Suppliment

8.1. List of Figures

Figure 1-1 Schematic representation of an influenza virus particle, adapted from[13] 7

Figure 1-2 Schematic representation of the IAV life cycle, modified from[127] 12

Figure 1-3 Influenza A virus RNA replication/transcription, adapted from[134] 14

Figure 1-4 Schematic representation of alveolar epithelium 18

Figure 1-5 Pathological effect of IAV on lung edema resolution 19

Figure 1-6 The molecular structure of Na^+,K^+-ATPase, modified from[217] 20

Figure 4-1 Growth kinetic of PR8 on different permanent cell lines 36

Figure 4-2 Total Na^+,K^+-ATPase α1-subunit expression in different IAV-infected cell lines 37

Figure 4-3 Redistribution of NKAα1 within the plasma membrane of infected cells 38

Figure 4-4 Development of TEER in Calu3 cells cultivated at LLI or ALI conditions 39

Figure 4-5 Calu3 cells cultivated at LLI or ALI conditions 40

Figure 4-6 Distribution of tight junction proteins in membrane of Calu3 cells cultivated under different conditions 41

Figure 4-7 Replication of PR8 virus in Calu3 cells cultivated in Transwell ® inserts at liquid-liquid interface (LLI), air-liquid interface (ALI) or in a culture plate 42

Figure 4-8 Redistribution of NKAα1 within the plasma membrane of infected cells 42

Figure 4-9 NKA quantification on the apical plasma membrane of IAV infected Calu3 cells 43

Figure 4-10 Redistribution of NKAβ1 within the plasma membrane of Calu3 cells infected with different IAV subtypes 44

Figure 4-11 Effect of actin targeting reagents and MEK-, MLCK- and ROCK inhibitors on IAV-induced NKA mistargeting 46

Figure 4-12 Influence of ER/Golgi transport inhibition on NKAβ1 mistargeting to the apical plasma membrane of IAV-infected cells 47

Figure 4-13 Subcellular NKA distribution in IAV-infected Calu3 cells 48

Figure 4-14 Effect of microtubule targeting reagents application on IAV-induced Na^+,K^+-ATPase mistargeting 49

Figure 4-15 Effect of microtubule targeting agents and Rho-kinase inhibitor on the IAV titer 50

Figure 4-16 Effect of kinesine-1 inhibition on IAV titer and NKA mistargeting in Calu3 cells 51

Figure 4-17 Influence of Rho-kinase inhibition on the amount of acetylated α-tubulin during IAV replication in Calu3 cells 52

Figure 4-18 Influence of HDAC6 activity on IAV replication and redistribution of NKAβ1 within the plasma membrane of infected cells 53

Figure 4-19 Effect of ROCK inhibition on cellular HDAC6 amount and caspase-3 activation during IAV infection 54

Figure 4-20 Influence of ROCK inhibition on caspase-3 activity in IAV-infected cells 55

Figure 4-21 Effect of caspase-3 inhibition on IAV-induced NKA misplocalization in Calu3 cells 56

Figure 4-22 Inhibition of Na^+, K^+-ATPase mispolarization in IAV-infected Calu3 cells improves vectorial water transport 57

Figure 4-23 Inhibition of ROCK reduced IAV-induced damage of the Calu3 cell monolayer 57

Figure 4-24 Effect of fasudil HCl treatment on body weight of IAV-infected mice 58

Figure 4-25 Effect of fasudil HCl treatment on IAV-induced alveolar edema 58

Figure 4-26 Effect of fasudil HCl treatment on IAV replication in vivo 59

Figure 4-27 Effect of fasudil HCl treatment on IAV titer and IAV-induced lung infiltration 59

8.2. List of Tables

Table 1. IAV RNA segments and encoded proteins 10

8.3. Materials

8.3.1. Instruments

Autoclave	Syste
Cell culture incubator	Labotect; Panasonic
Cell culture microscope CK2	Olympus
Confocal laser scanning microscope (TCS SP5)	Leica
Culture Hood (HERA safe KS)	ThermoScintific
ddH2O generator SG	Edwin DAMM
EVOS FL Auto Cell Imaging System	Life Technologies
Heat block	Steute
Magnetic stirrer	IKA Labortechnik
Microtome RM2125	Leica
Millicell®ERS-2 epithelial Volt-Ohm meter	Millipore
Mini centrifuge	Biofuge 13, Heraeus
Neubauer chamber	Optik Labor
Odyssay Infrared Imager	LI-COR
pH meter (Type 632)	Metrohm
Power Supply Powerpack P24	Biometra
Scale (MDS 580)	Kern
Scale (PM460) DeltaRange	Mettler
Scanner Epson Perfection V500 Photo scan	Epson
Science Imaging ChemoCam	INTAS
SDS-PAGE Gelsystem	Bio-Rad
Semi Dry Blotter Unit	Scie-PLAS
Shaker (Type 3013)	MSGV GmbH
Sterile needles	BD Microlance 3 BD

Syringe (microliter, serial 700)	Hamilton
Tecan Spark® 10M multimode microplate reader	Tecan
Typhoon 9200 scanner	GE Healthcare
Ultracentrifuge LE-80	Beckman Coulter
Reichter Ultracut R	Leica
Vacuum tissue processorASP200	Leica
Vacuum sealer	CIATRONIC
Vortex (Vibrofix VF1)	IKA Labortechnik
Water bath (SW-20C)	Julabo, GFL

8.3.2. Reagents and chemicals

1,2,3-Propanetriol glycidyl ethe (Epon 812)	Serva
1,4-Dithiothreit (C4H10O2S2) (DTT)	Roth
2,4,6-Tris(dimethylaminomethyl)phenol (DMP 30)	Serva
2'-[4-Ethoxyphenyl]-5-[4-Methyl-1-Piperazinyl]-2,5'-bi-1H-Benzimidazol-Trihydrochlorid-Trihydrat, Höchst 33342	TermoScintific/Invitrogen
2-Dodecenylsuccinic acid anhydride (DDSA)	Serva
3-Amino-9-ethylcarbazole (AEC)	Sigma Aldrich
Accutase	PAA
Acrylamide/Bisacrylamide 37, 5:1 premixedsolution	Roth
Ammonium acetate	Serva
Ammonium persulfate (APS)	Serva
Annexin V PE	Biolegend
Antifade ProGold mounting medium	TermoScintific/Invitrogen
Aprotinin	Roth
Benzamidin	Sigma
Blotting papers (GB004)	Scheicher&Schuell
Bradford reagent	Sigma Aldrich
Brefeldin 1000×	eBioscience
Bromophenol blue	Merck
BSA (Powder)	Roth
BSA (Solution, 30%)	Sigma Aldrich
Calcium chloride dihydrate ($CaCl_2 \cdot 2H_2O$)	Sigma Aldrich
Cycloheximide ($C_{15}H_{23}NO_4$)	Sigma Aldrich
DAPI (stock 1mg/ml)	Roth
DEAE Dextran (MW: 500,000)	PharmaciaBiotech
Dimethylsulfoxid (DMSO)	Sigma Aldrich

DRAQ5™ Fluorescent Probe Solution (5 mM)	TermoScintific/Invitrogen
D-Sucrose	Roth
Eosin G-Solution, 0,5 % in H_2O	Roth
Ethanol (absolute)	Roth
Ethidiumbromide	Roche
Ethylene glycol-bis(β-aminoethyl ether)-N,N,N',N'-tetraacetic acid (EGTA)	Sigma Aldrich
Ethylenediaminetetraaceticacid (EDTA)	Fluka
EZ-link Sulfo-NHS-SS-Biotin	Thermo Scintific
Falcon centrifuge tube	Falcon
FITC-Dextran, 70 kDa	Sigma Aldrich
Formaldehyde solution, 37 %	Roth
Glutaraldehyde, 25%	Sigma Aldrich
Glycerol	Sigma Aldrich
Glycine	Roth
Hematoxylin Solution, Mayer's	Sigma Aldrich
Hydrochloride (HCl)	Roth
Hydrogen peroxide (H_2O_2)	Roth
Imidazole ($C_3N_2H_4$)	Sigma Aldrich
Isopropanol	Roth
Leupeptin	Sigma Aldrich
Magnesium chloride hexahydrate ($MgCl_2 \cdot 6H_2O$)	Merck
Methanol	Roth
Methylnadic anhydride (MNA)	Serva
N-N-dimethylformamide (DMF)	Sigma Aldrich
Osmium tetroxide solution,4% in H2O	Sigma Aldrich
Paraformaldehyde (PFA)	Merck
Pefablock	Roth
Potassium chloride (KCl)	Roth
Potassium dihydrogen phosphate (KH_2PO_4)	Roth
PVDF-Membrane Immobilon-F transfe rmembrane	Millipore
Roti®-Blot A, 10x	Roth
Roti®-Blot K, 10x	Roth
Silicon rhodamine (SiR)-tubulin	Spirochrome AG
Skimmed milk, powder	Roth
Sodium acetate ($C_2H_3NaO_2$)	Sigma Aldrich
Sodium azide (NaN_3)	Sigma Aldrich
Sodium cacodylate trihydrate ((CH3)2AsO2Na · 3H2O)	Sigma Aldrich
Sodium chloride (NaCl)	Roth
Sodium dodecylsulfate (SDS)	Merck
Sodium fluoride (NaF)	Sigma Aldrich

Sodium hydrogen carbonate ($NaHCO_3$)	Fluka
Sodium hydrogenphosphate (Na_2HPO_4)	Sigma Aldrich
Sodium hydroxide (NaOH)	Merck
Sodium orthovanadate, Na_3VO_4	Sigma Aldrich
Sodium-β-glycerophosphate	Sigma Aldrich
Spectra™ Multicolor Broad Range Protein	ThermoFisher
TEMED (N,N,N',N'-Tetramethyl-ethylene diamine)	Serva
TERGITOL™ Type NP-40 (NP-40)	Merck
Tetrasodium pyrophosphate ($Na_4P_2O_7$)	Sigma Aldrich
Trichloroacetic acid (TCA)	Merck/ Sigma Aldrich
Triethanolamin	Sigma Aldrich
TRIS hydrochloride (TRIS HCl, $NH_2C(CH_2OH)_3 \cdot HCl$)	Roth
Trisaminomethane (Tris)	Roth
Triton X-100 (t-Octylphenoxypolyethoxyethanol)	Sigma Aldrich
Trypan blue solution, 0.4 %	TermoScintific/Invitrogen
Tween-20	Sigma Aldrich
Ultacentrifugation tubes	Beckman Coulter
Whatman 3MM Paper	Schleicher &Schüll
Xylene, histological grade	Sigma Aldrich

8.3.3. Inhibitors

Name	**Company**	**Working concentration**
Adenosine 5′-(3-thiotriphosphate) tetralithium salt	Sigma Aldrich	500 nM
Cytochalasin D	Sigma Aldrich	20 µM
Fasudil HCl	Selleckchem	10µM
Jasplakinolide	Sigma Aldrich	1µM
ML-7	Sigma Aldrich	1µM
Nocodazole	Sigma Aldrich	1µM
Paclitaxel	Sigma Aldrich	2µM
Raf1 kinase inhibitor I	Calbiochem	10µM
Rho kinase inhibitor RKI-1447(XIII)	Millipore	5µM
Tubacin	Sigma Aldrich	10µM

U0126	Sigma Aldrich	15 µM

8.3.4. Antibodies

Name	**Cat.N**	**Company**	**Dilution**
Acetyl-α-Tubulin (Lys40) (D20G3)	#5335	Cell Signaling Technology	1:2000
Alexa Fluor 488 anti-goat	# A11055	ThermoScintific/ Invitrogen/Gibco	1:1000
Alexa Fluor 488 anti-rabbit	# A21441	ThermoScintific/ Invitrogen/Gibco	1:1000
Alexa Fluor 568 anti-goat	# A11057	ThermoScintific/ Invitrogen/Gibco	1:1000
Alexa Fluor 594 anti-goat	# A11080	ThermoScintific/ Invitrogen/Gibco	1:1000
Alexa Fluor 594 anti-rabbit	# A11012	ThermoScintific/ Invitrogen/Gibco	1:1000
Alexa Fluor 647 anti-mouse	# A21237	ThermoScintific/ Invitrogen/Gibco	1:1000
Alexa Fluor 647anti-mouse	# A21463	ThermoScintific/ Invitrogen/Gibco	1:1000
Anti-Actin	# MA515739	ThermoScintific/ Invitrogen/Gibco	1:1000
Anti-ASIC3 (K-13)	# sc-21845	SantaCruz Biotechnology	1:200
Anti-beta IV Tubulin	# ab179509	Abcam	1:1000
Anti-Caspase3 (8G10)	# 9665	Cell Signaling Technology	1:500
Anti-E-cadherin	# sc-7870	SantaCruz Biotechnology	1:200
Anti-EEA1	# ab2900	Abcam	1:200
Anti-ERp72 (D70D12)	# 5033	Cell Signaling Technology	1:1000

Anti-HDAC6 (D2E5)	# 7558	Cell Signaling Technology	1:1000
Anti-influenza A HA	# ab20841	Abcam	1:2000
Anti-Influenza A M2	# MA1-082	ThermoScintific/ Invitrogen/Gibco	1:1000
Anti-Influenza A NP	# PA5-32242	ThermoScintific/ Invitrogen/Gibco	1:2000
Anti-Influenza A NP		S. Ludwig, Münster	1:100
Anti-Influenza A NP (FITC)	#ab20921	Abcam	1:20
Anti-KIF5B	# ab167429	Abcam	1:500IF 1:1000 WB
Anti-LAMP1 (D2D11)	# 9091	Cell Signaling Technology	1:200
Anti-Mucin 5AC	# ab198294	Abcam	1:1000
Anti-Myosin light chain	# ab11082	Abcam	1:200
Anti-Myosin light chain (phospho S1)	# ab157747	Abcam	1:1000
Anti-Myosin light chain kinase	# ab76092	Abcam	1:200
Anti-p44/42 MAPK (Erk1/2) (L34F12)	# 4696	Cell Signaling Technology	1:1000
Anti-Phospho-Ezrin (Thr567)/Radixin (Thr564)/Moesin (Thr558) (48G2)	# 3726	Cell Signaling Technology	1:1000
Anti-Phospho-p44/42 MAPK (Erk1/2) (Thr202/Tyr204) (D13.14.4E)	# 4370	Cell Signaling Technology	1:1000
Anti-Rab11	# 700184	ThermoScintific/ Invitrogen/Gibco	1:1000
Anti-Rab5	# ab66746	Abcam	1:1000
Anti-Rab7	# ab50533	Abcam	1:1000
Anti-RCAS1 (D2B6N)	# 12290	Cell Signaling Technology	1:1000

Anti-ZO1	# 40-2200	ThermoScintific/ Invitrogen/Gibco	1:100 IF 1:1000 WB
Anti-α1 NKA	# 05-369	Millipore/ Sigma Aldrich	1:1000
Anti-α-Tubulin	# T8328	Sigma Aldrich	1:2000
Anti-β1 NKA	# MA3-930	ThermoScintific/ Invitrogen/Gibco	1:1000
APC/Cy7 anti-mouse CD326 (Ep-CAM)	# 118218	Biolegend	1:100
Cy3 anti-rabbit	# 711-165-152	Jackson ImmunoResearch	1:10000
Cy5 anti-rabbit	# 715-175-150	Jackson ImmunoResearch	1:10000
HRP conjugated anti-goat	# sc-2354	SantaCruz Biotechnology	1:1000
HRP conjugated anti-mouse	# sc-2314	SantaCruz Biotechnology	1:1000
HRP conjugated anti-rabbit	# sc-2313	SantaCruz Biotechnology	1:1000
IRDye®800CW anti-goat	# 926-32214	Licor	1:10000
IRDye®800CW anti-mouse	# 92632210	Licor	1:10000
IRDye®800CW anti-rabbit	# 92632211	Licor	1:10000
Pacific Blue™ anti-mouse CD31	# 102422	Biolegend	1:100
Pacific Blue™ anti-mouse CD45	# 103126	Biolegend	1:100

8.3.5. Materials for cell culture and infection

8.3.5.1. Media

Bronchial Epithelial Growth Medium (BEGM™)	Lonza
Bronchial Epithelial Growth Medium Bullet Kit BEGM™	Lonza
Dulbecco's Modified Eagle Medium/Nutrient Mixture F-12 (DMEM-F12)	ThermoScintific/ Invitrogen/Gibco

Dulbecco's Modified Eagle's medium (DMEM)	ThermoScintific/ Invitrogen/Gibco
Minimum Essential Media (MEM), (10×)	ThermoScintific/ Invitrogen/Gibco
Minimum Essential Medium Eagle (MEM)	ThermoScintific/ Invitrogen/Gibco
Bovine Albumin, liquid, for cell culture (BSA) 30%	Sigma Aldrich
Trypsin- EDTA,0.05%	ThermoScintific/ Invitrogen/Gibco
Fetal calf serum (FCS)	ThermoScintific/ Invitrogen/Gibco
Non-Essential Amino Acids Solution , (100×)	ThermoScintific/ Invitrogen/Gibco
Penicillin/Streptomycin solution, (10,000 U/10mg/mL,100×)	ThermoScintific/ Invitrogen/Gibco
Sodium Pyruvate, (100 mM)	ThermoScintific/ Invitrogen/Gibco
TPCK-treated Trypsin	Sigma Aldrich

PBS+/+/BA/PS (500 ml)

492 ml PBS +/+

5 ml Penicillin/streptomycin (100×)

3 ml Bovine Albumin (BA) (30%)

Infection media #1 for MDCK, A549, MLE15 (100 ml)

98.5 ml DMEM (1×)

500 µl BSA (30%)

1µg/µl TPCK-Trypsin

Infection media #2 for Calu3 (100 ml)

96.5 ml MEM (1×)

1 ml Sodium Pyruvate (100×)

1 ml Non-Essential Amino Acids (100×)

500 µl BSA (30%)

Infection media #3 for CaCo2 (100 ml)

98.5 ml DMEM-F12 (1×)

500 µl BSA (30%)

1µg/µl TPCK-Trypsin

8.3.5.2.Plastics

96 Well Special Optics Microplate, clear flat bottom	Corning
Tissue culture flask	Greiner Bio-one
Tissue culture plates	Greiner Bio-one
Transwells® inserts	Corning

8.3.6. Kits

Caspase-3 activity	ThermoFisher Scintific
ECL (enhanced chemiluminescence) solution Kit	Amersham/GE
SuperSignal™ West Femto Maximum Sensitivity Substrate	ThermoFisher Scintific
BD Cytofix/Cytoperm™ Fixation/Permeabilization Solution Kit	BD Cytofix/Cytoperm™

8.3.7. Buffers and solutions

8.3.7.1.Buffers and solutions for foci assay

PBS +/+ /BA/antibiotic (200ml)

20 ml 10×PBS

174.8 ml ddH2O (sterile)

2 ml Penicillin/Streptomycin (100×)

1.2 ml BSA (35%)

2 ml Ca^{2+}/Mg^{2}(100×)

Avicel Medium (100 ml)

10 ml 10× MEM

33 ml ddH2O

1 ml Penicillin/Strepromycin liquid (100×)

1 ml BSA solution (30%)

50 ml Avicell Stock (2.5%)

1 ml DEAE-Dextran (1%)

4 ml NaHCO3 (7.5%)

100 µl of 1 mg/ml TPCK-trypsin

Avicel Stock (2.5%)

5 g Avicel-Powder

200 ml ddH2O

Autoclaved

Cell fixing buffer (100ml)

95 ml PBS +/+

4 ml Formaldehyde (37%)

1 ml Triton X-100 (t-Octylphenoxypolyethoxyethanol)

Antibody diluting solution for foci assay

Bovine serum albumin 3% (w/v) in 1×PBS +/+

AEC solution (20×)

20 g AEC

12,5 ml DMF

Acetate buffer (2 L)

7.708 g (50 mM) Ammonium acetate

534 µl (8.8 mM) H_2O_2

1950 ml ddH_2O

Adjust pH to 5.0 and fill up till 2 L

8.3.7.2.Buffers and solutions for biotinylation assay

Biotinylation buffer

10mM Triethanolamin

2mM $CaCl_2$

150mM sucrose

Adjust pH to 9

Beads washing solution A

150mM NaCl

50mM Tris, pH 7.4

5mM EDTA, pH 8.0

Beads washing solution B

500mM NaCl

50mM Tris, pH 7.4

5mM EDTA, pH 8.0

Beads washing solution C

500mM NaCl

20mM Tris, pH 7.4

0.2% BSA

8.3.7.3. Buffers and solutions for SDS-PAGE and Immunoblotting assay

Tris buffer pH6.8 (100 ml)

6.05 g Tris

50 ml ddH_2O

Adjust pH to 6.8 and fill up to 100ml with ddH_2O

Tris buffer pH 8.8 (100 ml)

18.8 g Tris

50 ml ddH_2O

Adjust pH to 8.8 and fill up to 100ml with ddH_2O

SDS-PAGE stacking gel

2.9 ml ddH2O

750 µl Acrylamide/Bisacrylamide (30%)

1.25 ml Tris, pH 6.8

50 µl SDS (10%)

50 µl APS (10%)

4 µl TEMED

SDS-PAGE resolving gel (10%)

4 ml ddH2O

3.3 ml Acrylamide/Bisacrylamide (30%)

2.5 ml Tris, pH 8.8

100 µl SDS (10%)

50 µl APS (10%)

6 µl TEMED

SDS-PAGE resolving gel (15%)

2.35 ml ddH2O

4.95 ml Acrylamide/Bisacrylamide (30%)

2.5 ml Tris HCl, pH 8.8

100 µl SDS (10%)

50 µl APS (10%)

6 µl TEMED

SLAB-loading Buffer, 5×

150 mM Tris, pH 6.8

7.5 % SDS

37.5 % Glycerol (99%)

0.2 % Bromphenol blue

4M DTT stock solution (5 ml)

3.086 g dissolve in 5 ml dd H_2O

SDS-PAGE running buffer (10×) (1 L)

2.5 g SDS

15 g Tris HCl

72.5 g Glycin

adjust total volume to 1 L with ddH2O

Anode buffer

100 ml of Roti®-Blot A

200 ml of 100% methanol

700 ml ddH2O

Cathode buffer

100 ml of Roti®-Blot K

200 ml of 100% methanol

700 ml ddH2O

NP40 Lysis buffer

20 mM Tris, pH 7.5

150 mM NaCl,

1 mM EDTA, pH 8.0,

1 mM EGTA, pH 8.0

0.5% NP40

2 mM Na_3VO_4, pH10.0

10 µl Pefablock (200 mM)

10 µl Aprotinin (5 mg/ml)

10 µl Leupeptin (5 mg/ml)

Tris-Buffered Saline (10X TBS) (1 L)

24.2 g Tris-HCl

80 g NaCl

dissolve by adding 900 ml ddH2O

adjust pH to 7.6 and total volume to 1 L with ddH2O

TBS/Tween (0.05%) (1XTBS-T) (1 L)

100 ml 10X TBS

900 ml ddH2O

0.5 ml Tween 20

Blocking buffer

Non-fat dry milk 5% (w/v) in 1×TBS-T

Antibody diluting solution for Western Blot

Non-fat dry milk 2% (w/v) in 1×TBS-T

8.3.7.4.Buffers and solutions for Immunofluorescence

Washing solution for Immunofluorescence

Bovine serum albumin 0.3% (w/v) in 1×PBS +/+

Blocking solution for Immunofluorescence

Bovine serum albumin 3% (w/v) in 1×PBS +/+

Antibody diluting solution for Immunofluorescence

Bovine serum albumin 2% (w/v) in 1×PBS +/+

4 % (w/v) Paraformaldehyde (100ml)

4 g Paraformaldehyde, EM grade

10 ml PBS -/-, 10×

ddH_2O

Dissolve PFA in 50 ml of ddH_2O and 1 ml of 1 M NaOH, warm up until 60°C.

Add 10 ml of 10×PBS -/- and allow cooling to room temperature.

Adjust pH to 7.4 with 1M HCl, and then adjust final volume to 100 ml with ddH_2O.

filtered through 0,45-µm membrane filtered

8.3.7.5.Buffers and solutions for differential centrifugation

Homogenization buffer

250 mMSucrose

3 mM Imidazole (pH 7.4)

1 mM EDTA

0.03 mMCycloheximide

Protease inhibitors

10 µg/mL Aprotinin

1 µg/mL Pepstatin

10 µg/mL Leupeptin

1 mM Pefabloc

Phosphatase inhibitors

1 mM Na_3OV_4

5 mM $Na_4P_2O_7$

50 mMNaF

10 mM β-Glycerophosphate

Hypotonic buffer

20 mM Tris (pH 8)

1.5 mM $MgCl_2$

10 mM CH_3COONa

8.3.7.6. Buffers and solutions for Epon embedding semi-thin section

Cacodilate buffer 0.2 M (10 ml)

428 mg Sodium cacodylate trihydrate

10 ml ddH

1.5% Glutaraldehyde in 0.2 M Cacodilate buffer

600 µl 25% Glutaraldehyde

5 ml 0.2M Cacodilate buffer

4.4 ml ddH_2O

Epon mixture

12 g Epon 812

4.5 g DDSA

7.5 g MNA

0.7 g DMP

steer at app 300 rpm for 10 min

8.3.7.7.Buffers and solutions flow cytometry

FACS-buffer

PBS **-/-**

1 mM EDTA,

2% (v/v) FCS

0,01% (w/v) NaN_3

pH 7.2

8.3.7.8.General Buffers and solutions

1×PBS buffer (1L)

800 ml ddH_2O

8 g NaCl

0.2 g KCl

1.44 g Na_2HPO_4

0.24 g KH_2PO_4

adjust the pH to 7.4 with HCl

10×PBS buffer (10L)

800 g NaCl

20 g KCl

144 g $Na_2HPO_4 \cdot 2H_2O$

24 g KH_2PO_4

8 L ddH_2O

1×PBS +/+ buffer (0,5L)

495 ml 1×PBS (autoclaved)

5 ml Ca^{2+}/Mg^{2+} solution (100×)

Ca^{2+}/Mg^{2+} solution (100×) (100ml)

1.32 g $CaCl_2 \cdot 2H_2O$

2.133 g $MgCl_2 \cdot 6H_2O$

100 ml ddH_2O

autoclaved

8.3.8. Viruses

Virus strain	Source	BSL level
A/Puerto Rico/8/1934 H1N1	Virus collection, Institute of Medical Virology, Justus-Liebig University Giessen, Germany	2
A/Victoria/3/75 H3N2	Virus collection, Institute of Medical Virology, Justus-Liebig University Giessen, Germany	2
A/Thailand/1(KAN-1)/2004 H5N1	Virus collection, Institute of Medical Virology, Justus-Liebig University Giessen, Germany	3
A/Anhui/1/2013 H7N9	Virus collection, Institute of Medical Virology, Justus-Liebig University Giessen, Germany	3

8.4. List of Abbreviations

A	Ampere
ASF	Airway surface fluid
AEC	Alveolar epithelial cells
AEC	Aminoethyl carbazole
ALI	Acute lung injury
ALI	Air-Liquid Interface
AQP	Aquaporin
ARDS	Acute respiratory distress syndrome
ASIC3	Acid-sensing ion channel 3
AT I	Alveolar epithelial cells type I
AT II	Alveolar epithelial cells type II
ATPases	Adenosine triphosphatase
BA	Bovine albumin
°C	Celsius
Ca	Calcium
CFTR	Cyctic fibrosis transmembrane conductance regulator
Cl	Chloride
cm	Centimetre
CO2	Carbon dioxide
DAPI	4′,6-diamidino-2-phenylindole
ddH2O	Double-distilled water
dH_2O	Distilled water
DMEM	Dulbecco’s modified Eagle’s medium
DMEM-F-12	Dulbecco's Modified Eagle Medium/Nutrient Mixture F-12
DMSO	Dimethylsulfoxide
dpi	Dots per inch
DTT	Dithiotreitol
EDTA	Ethylendinitrilotetraacetic acid
EE	Early endosome
ENaC	Epithelial sodium channel
ER	Endoplasmic reticulum
ERK	Extracellular signal–regulated kinases
FCS	Fetal calf serum
ffu	Foci forming unit
FIPs	Rab11-family interacting proteins
G	Gauge
g	Gramms
g	Earth's gravitational force
GTPase	Guanosine triphosphatase
GA	Golgi apparatus
h	Hours

H_2O	Water
HA	Hemagglutinin
HB	Homogenization buffer
HCl	Hydrochloric acid
HDAC	Histone deacetylase
HPAI	Highly pathogenic IAV
HRP	Horseradish peroxidase
IAV	Influenza A virus
IFN	Interferon
IL	Interleukin
K	Potassium
kDa	Kilodalton
KIF	Kinesin superfamily proteins
l	Liter
LE	Late endosome
LLI	Liquid-Liquid Interface
LRT	Lower respiratory tract
µ	Micro
m	Milli
M	Molar
M2	Matrixprotein 2
MCDK II	Madin Darbey Canine Kidney subclone II
MEK	Mitogen-activated protein kinase kinase
MEM	Minimum Essential Medium
min	Minute
MLCK	Myosin light-chain kinase
MLE 15	Murine lung epithelialuim clone 15
MOI	Multiplicity of infection
MT	Microtubules
n	Nano
Na	Sodium
NKAα1	Sodium-potassium adenosine triphosphatase alpha 1 subunit
NKAβ1	Sodium-potassium adenosine triphosphatase beta 1 subunit
nm	Nanometer
NP	Nucleoprotein
OCWB	On cell western blot
PAGE	Polyacrylamidgelelectrophoresis
PBS	Phosphate buffered saline
PCL	Periciliary liquid layer
PFA	Paraformaldehyde
pH	Potentia hydrogenii
PKC	Protein kinase C
pNA	P-nitroanilide

PNS	Post-nuclear supernatant
PS	Senicillin streptomycin
PVDF	Polyvinylidene difluoride
Rab	"Ras-related in brain" protein
Raf	Rapidly Accelerated Fibrosarcoma serine/threonine-specific protein kinase
RE	Recycling endosomes
rER	Rough ER
RNA	Ribonucleic acid
ROCK	Rho-associated coiled-coil containing serin/threonine kinase
ROS	Reactive oxygen species
rpm	Round per minute
RT	Room temperature
SDS	Sodiumdodecylsulfate
TBS	Tris-buffered saline
TEER	Transepithelial electrical resistance
TGN	Trans-Golgi network
TPCK	L-1-Tosylamide-2-phenylethyl chloromethyl ketone
TRAIL	Tumor necrosis factor-related apoptosis-inducing ligand
Tris	Trishydroxymethylaminomethane
URT	Upper respiratory tract
v	Volume
vRNP	Viral Ribonucleoprotein
VWT	Vectorial water transport
w	Weight
ZO	Zona-occludens

8.5. Acknowledgements

Firstly, I would like to express the gratitude to my supervisor - Prof. Dr. Stephan Pleschka for giving me the chance to perform my PhD work in his laboratory, for the interesting projects, for the support and many discussions on the way to finalize my thesis.

I would also like to thank all collaboration partners who contributed to my work - Univ.-Prof. Dr. Achim Gruber, Balachandar Selvakumar, PhD, and Ms. Jessica Schulze. My great appreciation to Prof. Dr. Susanne Herold, Dr. Thorsten Wolff and Christin Peteranderl, PhD, for the fruitful discussions and a look on the project from “the other side”.

I am very gratefully to my former colleagues in the research group of Prof. Pleschka – Florian Martinpott, Virginia Friedrichs, Mesut Karatas, Shartishta Dam for the support and fun that we had during our work together. I also would like to thank my colleagues from the group of Prof. Ziebuhr – Christin Müller, Alexandra Friedrich and Ganesh Bylapudi who helped me in work, gave good advises and shared ‘tips and tricks’. Especial thanks to Karin Schultheiß and Sigrun Broehl for the help in maintenance of the laboratory.

I also would like to thank Dr. Martin Hardt and Ms. Anna Möbus from Imaging Unit, JLU, for the help with confocal microscope and thin sections preparation. As well, I wish to thank Prof. Dr. Andre Menke for allowing me to work in his laboratory and Mr. Dirk Lohfink for the help with Odyssey scanner.

The last, I am very thankful to my husband, Dr. Tobias Arnold, for the critical reading of this work and for the help with translation in German language.

8.6. Affirmation

I declare that I have completed this dissertation single-handedly without the unauthorized help of a second party and only with the assistance acknowledged therein. I have appropriately acknowledged and referenced all text passages that are derived literally from or are based on the content of published or unpublished work of others, and all information that relates to verbal communications. I have abided by the principles of good scientific conduct laid down in the charter of the Justus Liebig University of Giessen in carrying out the investigations described in the dissertation.

Gießen, 24th of March, 2019

Irina Kuznetsova